

Contents

Explanation of Abbreviations	II
1 Introduction	1
2 Ultrashort Laser Pulses	3
2.1 Description of Ultrashort Pulses	3
2.2 Polarization of Light	6
2.3 Interference	8
2.4 Propagation in Solid Media	10
2.4.1 Dispersion	10
2.4.2 Nonlinear Effects	12
3 Beam Combining	16
3.1 Incoherent Beam Combining	16
3.2 Coherent Beam Combining	18
3.2.1 Tiled-Aperture and Filled-Aperture Implementation	18
3.2.2 Approaches to Coherent Beam Combining	21
3.2.3 Polarization Beam Combining	22
3.2.4 Divided-Pulse Amplification	26
3.3 Passive Coherent Beam Combining	27
4 Experimental and Theoretical Investigation of the Passive DPA Setup	34
4.1 Setup Including a Passive Fiber	34
4.1.1 Experimental Setup	34
4.1.2 Experimental Investigations	36
4.1.3 Theoretical Investigations	40
4.2 Setup Including an Active Fiber	44
4.2.1 Experimental Setup	44
4.2.2 Experimental Investigations at Low Average Powers Using Three PBSs	47
4.2.3 Experimental Investigations at High Average Power Using Two PBSs	48
4.2.4 Experimental Investigations at High Pulse Energy Using Two PBSs	53
4.2.5 Theoretical Investigations and Discussion	56
5 Conclusion	64
Bibliography	III
Appendix	A1

Explanation of Abbreviations

SVEA	Slowly Varying Envelope Approximation
FWHM	Full Width at Half Maximum
TBP	Time-Bandwidth Product
HWP	Half-Wave Plate
QWP	Quarter-Wave Plate
GVD	Group Velocity Dispersion
SPM	Self-Phase Modulation
XPM	Cross-Phase Modulation
CPA	Chirped-Pulse Amplification
CW	Continuous Wave
IBC	Incoherent Beam Combining
CBC	Coherent Beam Combining
SBC	Spectral Beam Combining
VBG	Volume Bragg Grating
MOPA	Master Oscillator Power Amplifier
SRS	Stimulated Raman Scattering
SBS	Stimulated Brillouin Scattering
DPA	Divided-Pulse Amplification
SPGD	Stochastic Parallel Gradient Descent
PBS	Polarization Beam Splitter
DOLP	Degree of Linear Polarization
AOM	Acousto-Optic Modulator
SLM	Spatial Light Modulator
MIIPS	Multiphoton Intrapulse Interference Phase Scan
PCF	Photonic Crystal Fiber
LMA	Large-Mode Area
LPF	Large-Pitch Fiber
HHG	High-Harmonic Generation

1 Introduction

An ongoing challenge in the field of laser technology is the development of high-power laser systems delivering ultrashort pulses while maintaining nearly ideal beam characteristics. Nowadays, these lasers find application in many areas such as in industry, medicine, and science. For example, in material processing a high production quality can be achieved with the help of high-energy ultrashort pulses, which prevents the melting of the material and, therefore, preserves marginal areas [1]. On the other hand, such laser systems find also application in research fields such as High-Harmonic Generation (HHG) [2, 3].

There are different laser technologies that have been used so far. Thereby, the geometry of the active medium plays an important role, whereas optical fibers quickly distinguished themselves by their outstanding advantages. Fibers are waveguides that have a large surface to volume ratio. Therefore, they exhibit excellent thermal properties and beam quality. Thus, they are well-suited for high-power applications.

Typically the desired output power is obtained by using both an oscillator, which provides low-energy high quality pulses, and a chain of amplifiers, in this case fibers, which amplify the signal to high power. This concept is known as Master Oscillator Power Amplifier (MOPA) [4]. However, the progress of this approach has been hampered by the onset of nonlinear and thermo-optic effects, which may cause spatial, temporal and spectral distortions of the pulsed beam. The mitigation of these detrimental effects is the main challenge in trying to reach even higher output powers. For this, the intensity inside of the signal core of the amplifying fiber has to be reduced by many orders of magnitude. One way to achieve this is the use of fibers with large mode-field diameters, so-called Large-Mode Area (LMA) fibers. However, the scaling of the mode-field diameter is typically restricted by production tolerances of the particular fiber design. Another possibility is the use of the so-called Chirped-Pulse Amplification (CPA) [5] technique. Thereby, a pulse delivered by an oscillator is stretched in time by imposing a chirp to it. As a result, the peak power is significantly reduced. Then, the stretched pulse is amplified to high power and, subsequently, the chirp is removed. Hence, the compressed pulse duration is comparable to that of the initial pulse. This results in a very high peak power, which exceeds the one achievable without this technique. However, the geometrical dimensions of the laser system usually restrict the available stretched pulse duration. While for pulse stretching passive fibers or small-footprint multi-pass grating stretchers can be employed, compression stages usually have to be realized using a single-pass grating compressor in order to achieve high efficiencies and in order to handle high peak-powers in the gigawatt range. Thus, for CPA system it is the width of the employed grating and the available length of the compressor (i.e. the achievable delay), which restrict the maximum stretched pulse duration to a few nanoseconds. With these techniques average output powers of 830 W [6] and pulse energies of 2.2 mJ [7] have already been reported.

To further scale the output power, the approach of beam combination [8] has become a viable

alternative. The idea behind this is to combine the output beams of several individual lasers into one intense beam. This approach ideally allows increasing the overall output power by a factor that equals the number of lasers to be combined. In order to apply this technique to the amplification of ultrashort pulses, the pulses emitted by the different lasers have to possess a fixed phase relation with each other. To achieve this, one input laser is used whereby its beam is split into a certain number of beams, which are amplified in spatially separated amplifiers and which are finally coherently combined. Thus, this technique is referred to as Coherent Beam Combining (CBC). Since this results in an interferometric setup, the path lengths have to be matched, which can be realized by actively controlling the phases. Using CBC with active-feedback a record pulse energy of 3 mJ [9] was reported.

An elegant possibility is to use the Sagnac geometry, i.e. one input beam is split into two counter-propagating beams passing through the same optical path and amplifier. These pulses can be, afterwards, passively combined [10]. However, in this implementation the initial pulse is just split in two pulses. A further possibility is to divide the pulses temporally before amplification and to recombine them afterwards. Initially, this approach was demonstrated using birefringent crystals for division and combination and it is referred to as Divided-Pulse Amplification (DPA) [11, 12]. This technique has already been successfully integrated into a passive CBC setup using the Sagnac geometry [13], but since the crystals provide delays of only a few picoseconds, this experiment was performed using non-stretched pulses. For such a passive CBC approach using DPA a pulse energy of 3.1 μ J was reported.

The aim of this work is the implementation of the passive CBC and DPA approach (short passive DPA) as the main amplification stage in an existing CPA system. Therefore, an experimental setup will be developed, which is capable of producing temporal delays in the nanosecond range. This setup will be investigated both theoretically and experimentally.

In the following chapter, theoretical basics of ultrashort pulses and some characteristics of light, such as polarization and interference, will be explained briefly. Moreover, the most important detrimental effects caused by the propagation through solid media will be explained, too. In the third chapter, the topic of beam combination will be classified and considered in more detail. Furthermore, different approaches will be presented, whereas the focus will be on CBC. Chapter four deals with the experimental realization and with the characterization of the setups used for the experimental demonstration. Finally, the whole work will be summarized briefly and a short outlook of further investigations will be given.

2 Ultrashort Laser Pulses

The aim of this work is the amplification of ultrashort pulses in high-power fiber amplifiers. In this context, some theoretical basics are explained in the following. First, the theoretical description of pulses and some physical quantities will be presented. Afterwards, both the properties of polarization and interference are considered, which will be important for the scheme of CBC used in this work. Finally, the effect of dispersion and nonlinear effects on the ultrashort pulses propagating through optical fibers will be discussed.

2.1 Description of Ultrashort Pulses

Light is an electromagnetic wave and its physical nature is described by the Maxwell's equations. Due to the harmonic time dependence of the real¹ electric field in space² $\mathbf{E}(\mathbf{r}, t)$, it is possible to introduce a representation of the field, which satisfies those equations:

$$\mathbf{E}(\mathbf{r}, t) = \frac{1}{2} \{ \mathbf{E}_0 \exp [i(\mathbf{k}\mathbf{r} - \omega_0 t)] + c.c. \} \quad (2.1)$$

and is called plane wave³. Thereby \mathbf{E}_0 is the field amplitude, ω_0 is a certain angular frequency and \mathbf{k} is the wave vector. Since Eq. (2.1) describes a stationary, infinite wave train oscillating at one frequency, this representation holds only for monochromatic light.

In the case of optical pulses this description must be extended. Since in general a pulse is of finite extent in both space and time, it can be expressed by a superposition of stationary plane waves with different frequencies and propagation directions. The electric field can be decomposed into infinite wave trains with the help of the Fourier transformation (see Appendix A), which results in [14]

$$\mathbf{E}(\mathbf{r}, t) = \frac{1}{2} \left\{ \int_{-\infty}^{\infty} \int_{-\infty}^{\infty} \tilde{\mathbf{E}}(\mathbf{k}, \omega) \exp [i(\mathbf{k}(\omega)\mathbf{r} - \omega t)] d\mathbf{k}d\omega + c.c. \right\}, \quad (2.2)$$

with $\tilde{\mathbf{E}}(\mathbf{k}, \omega)$ being the spectral components. Consequently, a pulse is a polychromatic wave. To simplify this mathematical expression it is assumed that all wave trains of the pulse propagate in the same direction, namely along the z -axis, and that the transverse energy distribution is constant over the pulse. Furthermore, an approximation often used is the so-called Slowly Varying Envelope Approximation (SVEA) [15]. In this approximation it is assumed that the envelope of a pulse varies slowly in space and time compared to the rapidly oscillating field.

¹Real part of a complex quantity: $2\Re\{z\} = z + z^* = z + c.c.$, with $c.c.$ denoting the complex conjugate.

²Boldface symbols denote vectors in three-dimensional space (x, y, z) .

³Analogous for the magnetic field, which will not be considered.

This assumes that just those spectral components within a narrow band $\Delta\omega$ around the center frequency ω_0 contribute significantly. Using these assumptions, the electric field can be expressed as [14, 16]

$$\mathbf{E}(\mathbf{r}, t) \approx \frac{1}{2} F(x, y) \left\{ \exp(-i\omega_0 t) \int_{\omega_0 - \frac{\Delta\omega}{2}}^{\omega_0 + \frac{\Delta\omega}{2}} \tilde{E}(\omega) \exp[i(k(\omega)z - (\omega - \omega_0)t)] d\omega + c.c. \right\} \hat{\mathbf{x}} \quad (2.3)$$

$$= \frac{1}{2} F(x, y) [A(z, t) \exp(-i\omega_0 t) + c.c.] \hat{\mathbf{x}} \quad , \quad (2.4)$$

with k denoting the z -component of the wave number, $\hat{\mathbf{x}}$ an unit vector oriented in x -direction, $F(x, y)$ the transverse energy distribution, and $A(z, t)$ the complex (slowly varying) amplitude. The spectral components can now be expressed as

$$\tilde{E}(\omega) = |\tilde{E}(\omega)| \exp[i\phi(\omega)] \quad , \quad (2.5)$$

with the spectral phase $\phi(\omega)$. Now the wave vector can be developed in a Taylor series

$$k(\omega) = \sum_{m=0}^{\infty} \left. \frac{d^m k(\omega)}{d\omega^m} \right|_{\omega=\omega_0} (\omega - \omega_0)^m \quad . \quad (2.6)$$

The zeroth order term describes the phase velocity of $\tilde{E}(\omega_0)$ given by $v_p = \omega_0/k(\omega_0)$, while the first order term defines the group velocity $v_g = (dk(\omega)/d\omega)_{\omega=\omega_0}^{-1}$, which describes the energy propagation. When omitting the energy distribution $F(x, y)$, Eq. (2.4) changes to

$$\mathbf{E}(\mathbf{r}, t) = \frac{1}{2} \{A(z, t) \exp[i(k(\omega_0)z - \omega_0 t)] + c.c.\} \hat{\mathbf{x}} \quad . \quad (2.7)$$

Another important parameter of a pulse is its duration Δt . There are different definitions for this parameter, but throughout this work the Full Width at Half Maximum (FWHM) will be used. The shortest achievable pulse duration is limited by the spectral bandwidth $\Delta\nu = \Delta\omega_{\text{FWHM}}/(2\pi)$. The Time-Bandwidth Product (TBP) [4] summarizes the relationship between the pulse duration and the spectral bandwidth:

$$\Delta t \Delta\nu \geq \text{TBP} \quad , \quad (2.8)$$

the TBP is a constant that depends exclusively on the pulse shape. Typically, the lower limit of this inequality, i.e. the so-called transform limited pulses, is reached when the spectral phase of the pulse is linear. A pulse is called ultrashort if $\Delta t \lesssim 1$ ps.

A commonly used example is a Gaussian pulse. In that case the TBP is 0.441 and the complex amplitude is given by [17]

$$A(z, t) = \sqrt{\hat{P}} \exp\left(-2 \ln(2) \frac{t^2}{\Delta t^2}\right) \quad , \quad (2.9)$$

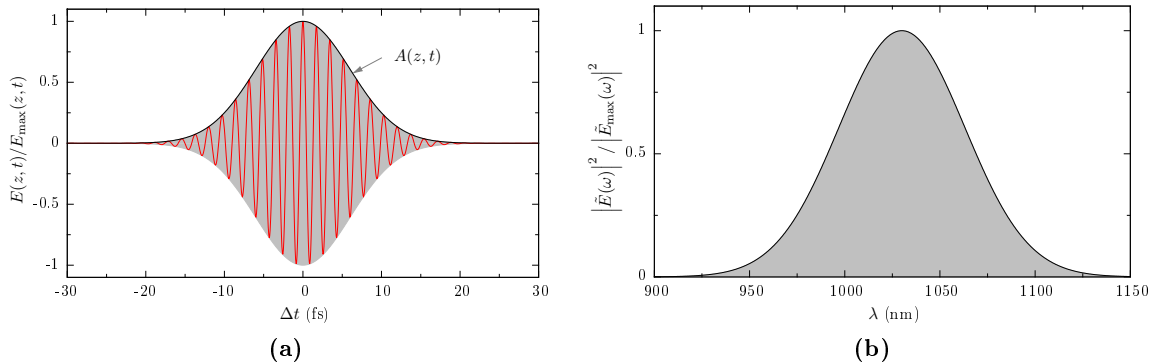


Fig. 2.1: Representation of (a) the electric field and the envelope of a transform limited ultrashort Gaussian pulse with $\Delta t = 20$ fs and (b) its corresponding spectrum with a bandwidth of $\Delta\lambda \approx 78$ nm at a center wavelength of $\lambda_0 = 1030$ nm.

with \hat{P} being the peak power of the pulse. In Fig. 2.1 a transform limited ultrashort ($\Delta t = 20$ fs) Gaussian pulse and its corresponding spectrum are depicted. This short pulse duration (near the limit of the SVEA) was chosen in order to show the fast oscillations of the electric field.

There are important physical quantities that are commonly used to characterize a pulse or a series of pulses. Thus, for a single pulse, the instantaneous optical power $P(\mathbf{r}, t)$, intensity $I(\mathbf{r}, t)$ and the field amplitude $A(\mathbf{r}, t)$ are related by [18]

$$P(\mathbf{r}, t) = \int_{\mathbf{A}} I(\mathbf{r}, t) d\mathbf{A} = C |A(\mathbf{r}, t)|^2 \quad , \quad (2.10)$$

where C comprises all the constant factors. This expression describes the spatial and temporal distribution of the power, whereby its maximum is the peak power \hat{P} . For a series of pulses the repetition rate $f_{\text{rep}} = 1/T$ describes the periodicity with which the pulses are emitted. The power measured by a power meter is given by the spatially resolved average power [18]

$$\bar{P}(\mathbf{r}) = \lim_{T \rightarrow \infty} \frac{1}{2T} \int_{-T}^T P(\mathbf{r}, t) dt \quad . \quad (2.11)$$

Finally, the energy content is described by the pulse energy, which is given by [18]

$$E_p = \int_{-\infty}^{\infty} \int_{-\infty}^{\infty} P(\mathbf{r}, t) dt d\mathbf{r} = \frac{\bar{P}}{f_{\text{rep}}} \quad , \quad (2.12)$$

where \bar{P} is the overall average power. The peak power can be determined by

$$\hat{P} = C \frac{E_p}{\Delta t} \quad , \quad (2.13)$$

where Δt is the pulse duration and C is a constant factor depending on the pulse shape.

2.2 Polarization of Light

The polarization of an electromagnetic wave is a three-dimensional phenomenon that describes the temporal evolution of the orientation of the electric field vector at any position in space. The state of polarization is determined by the relationship between the components of the field vector, which can be written as vector addition [18]

$$\mathbf{E}(\mathbf{r}, t) = \frac{1}{2} [E_x(\mathbf{r}, t)\hat{\mathbf{x}} + E_y(\mathbf{r}, t)\hat{\mathbf{y}} + E_z(\mathbf{r}, t)\hat{\mathbf{z}} + c.c.] \quad . \quad (2.14)$$

In the case of paraxial fields, the electric field vectors can be considered to lie in transverse planes propagating in the same direction. Consequently, when propagating along the z -axis, $E_z(\mathbf{r}, t)$ can be neglected. Comparing with Eq. (2.7), for an ultrashort pulse it follows

$$\mathbf{E}(\mathbf{r}, t) = \frac{1}{2} [A_x(z, t)\hat{\mathbf{x}} + A_y(z, t)\hat{\mathbf{y}}] \exp [i(k(\omega_0)z - \omega_0 t)] + c.c. \quad , \quad (2.15)$$

with the complex (slowly varying) amplitudes that can be expressed as

$$A_x(z, t) = |A_x(z, t)| \exp [i\phi_x(t)] \quad A_y(z, t) = |A_y(z, t)| \exp [i\phi_y(t)] \quad . \quad (2.16)$$

In general, the phase relation and, therefore, the polarization state can vary in time, which is referred to as partial polarization. This time dependence will be neglected for the case of fully polarized light. The evolution of the field vector is defined by the oscillations of the two orthogonal amplitudes and its relative phase $\phi = \phi_y - \phi_x$. Considering a particular plane of incidence, the component lying in that plane (e.g. x -component) is called p -polarization component, while the component being perpendicular to that plane (e.g. y -component) is called s -polarization component⁴. Thus, the state of polarization is identified by the x - y -projection plane. For arbitrary amplitudes and phases, according to Eq. (2.16), the field is in general elliptically polarized. Nevertheless there are two widely used degenerated polarization states: linear and circular. For the first case the oscillations of the components have a phase difference $\phi = 2m\pi$ ($m = 0, 1, 2, \dots$), which is shown in Fig. 2.2a for an ultrashort pulse. The orientation angle ψ of this linear polarization depends furthermore on the magnitudes of the amplitudes and is given by [19]

$$\tan(2\psi) = \frac{2|A_x(z, t)||A_y(z, t)| \cos \phi}{|A_x(z, t)|^2 - |A_y(z, t)|^2} \quad . \quad (2.17)$$

For $|A_x(z, t)| = |A_y(z, t)|$ this results in $\psi = 45^\circ$. In the case of circular polarization the phase between the components is $\phi = (2m - 1)\pi/2$ and it requires also that $|A_x(z, t)| = |A_y(z, t)|$. A distinction is made for $\phi = \pi/2$ and for $\phi = -\pi/2$, which are called right-handed and left-handed circularly polarized, respectively. Fig. 2.2b shows a right-handed circularly polarized ultrashort pulse⁵.

⁴From the German words *parallel* and *senkrecht*.

⁵Since the amplitude of the oscillations changes in time, this would lead to a spiral for the projection of any polarization other than linear polarization. Therefore, just the superposition of the oscillations with constant amplitudes are plotted. Due to the different scale ratio it seems to be elliptical, but it is actually a circle.

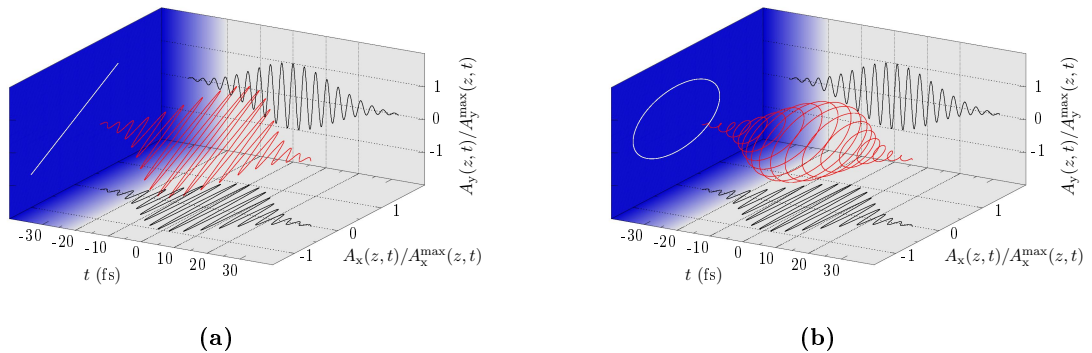


Fig. 2.2: Representation of a polarized ultrashort pulse with $\Delta t = 20$ fs and $\lambda_0 = 1030$ nm. Its components are projected in the respective x - and y -planes, additionally its projection against the propagation direction is shown, (a) for linear polarization and (b) for circular polarization.

Isotropic optical materials are polarization independent. To achieve a phase difference between the field components, materials with polarization-dependent properties are used. These are called anisotropic materials, which is here limited to uniaxial materials. They possess one axis of symmetry (the optical axis) with isotropic properties for directions perpendicular to it. Those polarization components perpendicular and parallel to that axis will experience different refractive indexes n_o and n_e (subscripts denoting ordinary and extraordinary). Such a material it is said to be birefringent. There is a maximum phase difference that the polarization components can accumulate, which depends on the propagation length l through the material [17]:

$$\Delta\varphi = \varphi_e - \varphi_o = \frac{2\pi}{\lambda} l (n_e - n_o) \quad . \quad (2.18)$$

For known $(n_e - n_o)$ the maximum phase difference for a certain wavelength λ can be adjusted with l . This is used, for example, for the so-called Half-Wave Plates (HWPs) and Quarter-Wave Plates (QWPs), which maximum phase differences are $\Delta\varphi = \pi$ and $\Delta\varphi = \pi/2$, respectively. The effect of a HWP is to rotate the orientation angle of linearly polarized light, and the effect of a QWP is to generate elliptical polarization out of linear polarization and vice versa. For the special case of a 45° orientation between the linearly polarized input and the optical axis of the QWP, circular polarization is generated.

One convenient mathematical formalism to handle the state of polarization of light is the Jones matrix calculus [19]. This formalism is only valid for completely polarized light, which is the case dealt with in this work. The vector including the two field components, as given by Eq. (2.16), is called Jones vector and it will be represented by \mathbf{A} . To describe the polarizing devices, 2×2 matrices are used, which are called Jones matrices and are represented by \mathbf{J} . The input and the output of such a device are then related by $\mathbf{A}_{\text{out}} = \mathbf{J}\mathbf{A}_{\text{in}}$. In Tab. 2.1 the Jones matrices for a linear polarizer with transmission coefficients t and for a wave plate are listed. Furthermore, these may be rotated by an angle θ with respect to their optical axis. In the experiments described in this work the rotation of a HWP will be used. With the help of the rotation matrix $\mathbf{R}(\theta)$ (see

Tab. 2.1: Jones matrix for a linear polarizer and a wave plate.

Optical Element	Jones Matrix
Linear polarizer	$\mathbf{J}_P = \begin{pmatrix} t_x & 0 \\ 0 & t_y \end{pmatrix}$
	for ideal <i>p</i> -polarization for ideal <i>s</i> -polarization $\mathbf{J}_{Pp} = \begin{pmatrix} 1 & 0 \\ 0 & 0 \end{pmatrix}$ $\mathbf{J}_{Ps} = \begin{pmatrix} 0 & 0 \\ 0 & 1 \end{pmatrix}$
Wave plate	$\mathbf{J}_{WP} = \begin{pmatrix} \exp[i\varphi_o] & 0 \\ 0 & \exp[i\varphi_e] \end{pmatrix}$
	Half-Wave Plate ($\Delta\varphi = \pi$) Quarter-Wave Plate ($\Delta\varphi = \pi/2$) $\mathbf{J}_{HWP} = \exp(i\varphi_o) \begin{pmatrix} 1 & 0 \\ 0 & -1 \end{pmatrix}$ $\mathbf{J}_{QWP} = \exp(i\varphi_o) \begin{pmatrix} 1 & 0 \\ 0 & -i \end{pmatrix}$

Appendix B) it follows [19]

$$\mathbf{J}_{HWP}(\theta) = \begin{pmatrix} \cos(2\theta) & \sin(2\theta) \\ \sin(2\theta) & -\cos(2\theta) \end{pmatrix}, \quad (2.19)$$

where the constant phase term is neglected.

2.3 Interference

Interference is a phenomenon, which occurs for all kinds of coherent waves. The superposition of two or more waves in space and time results in a wave that consists of the sum of all individual waves. This may lead to regions of enhancement or cancellation of the fields depending on their relative phases, which are then called constructive or destructive interference, respectively. In optics, this holds for the superposition of the complex field amplitudes in the case of monochromatic light of the same frequency [18]. However, ultrashort pulses are polychromatic. Nevertheless, since the bandwidth of the ultrashort pulses of interest for this work is assumed to be narrow, they will be treated as quasi-monochromatic. The superposition of two identical ultrashort pulses propagating in the same direction can be expressed as

$$\mathbf{E}(\mathbf{r}, t) = \mathbf{A}_1(z, t - \tau_1) \exp[-i\omega_0(t - \tau_1)] + \mathbf{A}_2(z, t - \tau_2) \exp[-i\omega_0(t - \tau_2)] \quad , \quad (2.20)$$

(complex conjugate terms omitted) with the time delays $\tau_m = k(\omega_0)z_m/\omega_0$ corresponding to different propagation distances z_m (where $m = 1, 2$). The observable real effect of interference are regions with minimum or maximum intensity. Using the definition of the intensity⁶ $I(\mathbf{r}, t) \sim \langle \mathbf{E}(\mathbf{r}, t) \mathbf{E}^*(\mathbf{r}, t) \rangle$ (according to [18], constant factors neglected), it follows after some

⁶The operator $\langle \cdot \rangle$ denotes time average over a long period.

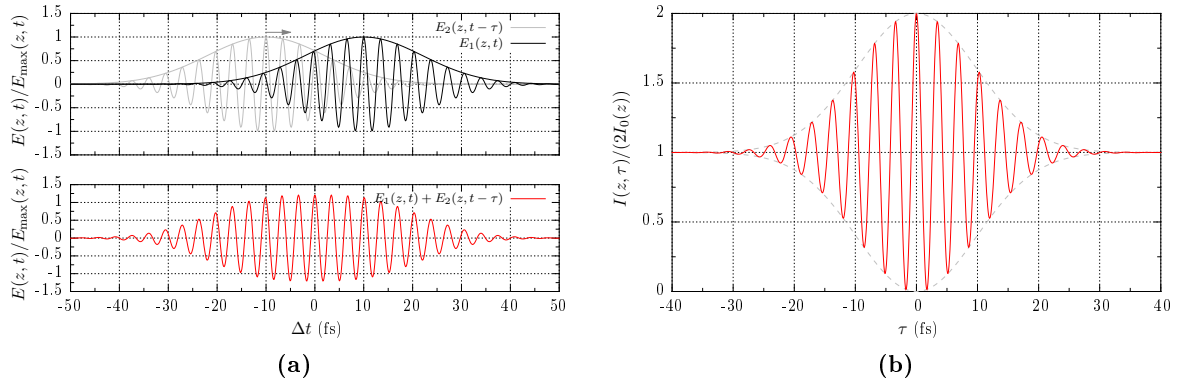


Fig. 2.3: Representation of (a) the superposition of two identical Gaussian pulses with $\Delta t = 20$ fs (compare Fig. 2.1a) delayed by $\tau = 20$ fs and (b) the interference depending on the delay.

calculation that [18]

$$I(\mathbf{r}, t) = I_1(\mathbf{r}, t) + I_2(\mathbf{r}, t) + \underbrace{2\sqrt{I_1(\mathbf{r}, t)I_2(\mathbf{r}, t)} |\gamma(\tau_1, \tau_2)| \cos[\Delta\varphi(\tau_1, \tau_2)]}_{\text{Interference term}}, \quad (2.21)$$

with $I_m(\mathbf{r}, t) \sim |\mathbf{A}_m(z, t - \tau_m)|^2$ being the intensities of the individual pulses (where $m = 1, 2$), $\Delta\varphi(\tau_1, \tau_2) = \omega_0(\tau_2 - \tau_1)$ being the phase difference between them and the complex degree of coherence [18]

$$\gamma(\tau_1, \tau_2) = \frac{\langle \mathbf{A}_1(z, t - \tau_1) \mathbf{A}_2^*(z, t - \tau_2) \rangle}{\sqrt{I_1(\mathbf{r}, t)I_2(\mathbf{r}, t)}}, \quad (2.22)$$

which is a measure of the temporal coherence. Temporal coherence describes the ability of a wave train to interfere with a time-delayed copy of itself. By writing $\tau_1 = 0$ and $\tau_2 = \tau$, then Eq. (2.22) acquires the form of a normalized autocorrelation function. For $|\gamma(\tau)| = 1$ light is fully coherent, for $0 < |\gamma(\tau)| < 1$ partially coherent and for $|\gamma(\tau)| = 0$ it is incoherent. Generally, in the case of partial coherence the correlation is limited to a certain time range, which is called coherence time τ_c and it is defined as the FWHM of $|\gamma(\tau)|$. Within this time, light can propagate the distance [14, 18]

$$l_c = c\tau_c = C \frac{\lambda_0^2}{\Delta\lambda}, \quad (2.23)$$

which is called coherence length. Obviously, the coherence time is inversely related to the bandwidth $\Delta\lambda = \Delta\lambda_{\text{FWHM}}$. The constant factor C depends on the spectral shape and it is, for example, 1 for a rectangular shape and $\sqrt{2\ln(2)/\pi}$ for a Gaussian shape [18]. However, the full description of coherence for ultrashort pulses is more complicated and it requires a complex treatment of coherence theory, which is not considered here. As an example, using Eq. (2.23) the coherence time and length of the pulse depicted in Fig. 2.1 would be $\tau_c \approx 30$ fs and $l_c \approx 9$ μm . But there is also a coherence time, which describes the long-term relationship of the waves. Since for a series of pulses the spectrum in Fig. 2.1b would be a frequency comb spanning under the envelope, the coherence time is determined by the spectral widths of the single peaks. Consequently, the bandwidth may be much smaller and results in a longer coherence time than that of

a single pulse [20]. Just as an example, the superposition of two equal linearly polarized Gaussian ultrashort pulses shifted by $\tau_2 = \tau$ ($\tau_1 = 0$) is shown in Fig. 2.3a. In Fig. 2.3b the corresponding interference (after Eq. (2.21)) at the maximum with $I_1^{\max}(\mathbf{r}, t) = I_2^{\max}(\mathbf{r}, t) = I_0(z)$ with respect to τ is plotted. As can be seen, when the pulses are in phase ($\tau = 0$), the total intensity gets doubled.

2.4 Propagation in Solid Media

If light propagates through media different from vacuum, nonlinear effects and dispersion are present. The influence of the former becomes higher the higher the optical power. Since ultrashort pulses can achieve very high peak powers, these effects cannot be neglected.

2.4.1 Dispersion

The dependence of a physical quantity on the frequency is called dispersion. There are different kinds, such as material or angular dispersion, but they are all related to the frequency dependence of the refractive index $n(\omega)$. A good approximation is the Sellmeier equation⁷ [16]

$$n^2(\omega) = 1 + \sum_{m=1}^N \frac{B_m \omega_m^2}{\omega_m^2 - \omega^2} \quad , \quad (2.24)$$

with the material-dependent parameters B_m and ω_m . In Fig. 2.4a the frequency dependence of the refractive index of silica with $N = 3$ is depicted. It is normally distinguished between the case of normal dispersion (when $dn(\omega)/d\omega > 0$) and anomalous dispersion (when $dn(\omega)/d\omega < 0$).

To simplify further considerations, according to Eq. (2.6), it is common to introduce the abbreviations [16]

$$\beta_m = \left. \frac{d^m k}{d\omega^m} \right|_{\omega=\omega_0} \quad \text{with} \quad \beta_0 = \frac{\omega_0}{v_p} \quad , \quad \beta_1 = \frac{1}{v_g} \quad , \quad \beta_2 = \frac{d}{d\omega} \left(\frac{1}{v_g} \right) \quad . \quad (2.25)$$

Hence, the parameters β_0 and β_1 determine the phase velocity and group velocity of the pulse, respectively, while β_2 is the Group Velocity Dispersion (GVD), which is responsible for the broadening of the pulse. A medium with $\beta_2 > 0$ exhibits normal GVD, which after propagation of a pulse results in a so-called positive chirp, since the low frequencies of the pulse propagate faster than the high frequencies. Thus, the frequency components of a pulse are rearranged under its envelope. The opposite occurs for anomalous GVD and results in a negative chirp.

As a rough estimation, the increase of the pulse duration Δt after a propagation length L due

⁷Far from resonances of the bound electrons of the medium.

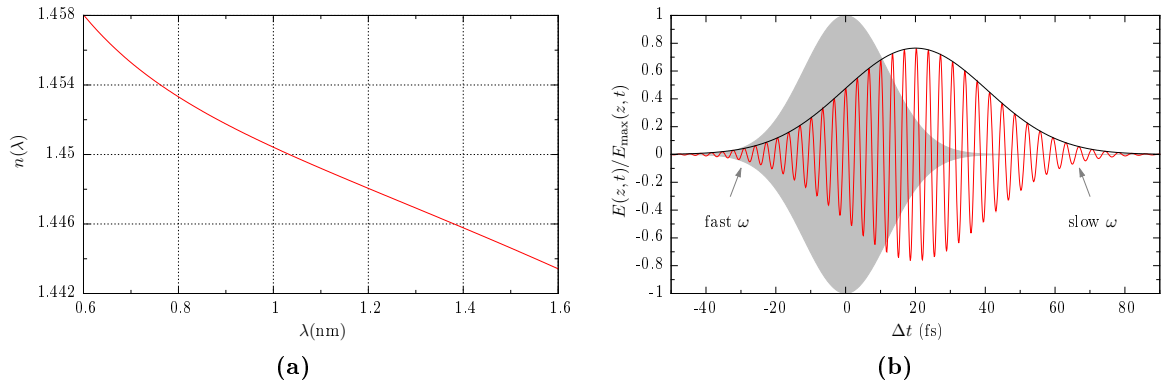


Fig. 2.4: Influence of material dispersion. (a) Variation of the refractive index with the wavelength $\lambda = 2\pi c/\omega$ for silica (after [16]). (b) Broadening and frequency chirp of the ultrashort Gaussian pulse from Fig. 2.1a (shown in grey) when travelling through 10 mm of silica ($\beta_2 \approx 20 \text{ ps}^2 \text{ km}^{-1}$ [16]).

to material dispersion can be estimated by [21]

$$\Delta t = \frac{L}{v_g} \quad \Rightarrow \quad \Delta(\Delta t) = \Delta\omega \left(\frac{d\Delta t}{d\omega} \right)_{\omega=\omega_0} = \Delta\omega\beta_2 L \quad . \quad (2.26)$$

Obviously, the pulse broadening becomes more dramatic the broader the bandwidth of the pulse and the longer the interaction length with the material. Consequently, for ultrashort pulses the effect of material dispersion is not negligible. For the example of a Gaussian pulse, the dispersed pulse can be analytically calculated. Using the envelope function of Eq. (2.9), after calculating its spectrum (according to Appendix A), and after considering the first and second order terms of Eq. (2.6) and by using the abbreviations of Eq. (2.25), it follows

$$A(z, t) = \frac{\sqrt{\hat{P}}}{\sqrt{1 - i\frac{z}{L_D}}} \exp\left(-\frac{2\ln(2)(t - \beta_1 z)^2}{\Delta t_z^2}\right) \exp\left(i\frac{z}{L_D} \frac{2\ln(2)(t - \beta_1 z)^2}{\Delta t_z^2}\right) \quad , \quad (2.27)$$

with the dispersion length L_D and the pulse duration Δt_z after a distance z

$$L_D = \frac{\Delta t^2}{4\ln(2)\beta_2} \quad \text{and} \quad \Delta t_z = \Delta t \sqrt{1 + \left(\frac{z}{L_D}\right)^2} \quad . \quad (2.28)$$

Finally, the electric field is given by Eq. (2.7). Fig. 2.4b shows an ultrashort Gaussian pulse after propagating through $z = 10 \text{ mm}$ silica.

One approach that benefits from dispersion is the CPA [5]. With the help of a dispersive delay line, called stretcher, a pulse is stretched in time domain. This reduces the peak power during the propagation through an amplifying medium and, therefore, the occurring nonlinear effects are effectively mitigated. With this technique, much higher output powers are achievable. Subsequently, another dispersive element, called compressor, removes the chirp and compresses the pulse to its initial duration.

2.4.2 Nonlinear Effects

In conventional optics, when an electromagnetic field interacts with a material, this becomes polarized and the polarization $\mathbf{P}(\mathbf{r}, t)$ depends on the electric field strength $\mathbf{E}(\mathbf{r}, t)$ in a linear manner. If the field is strong enough, the optical response follows a more complicated function and it can, in the most general case (including loss and dispersion), be expressed in frequency domain as a power series⁸ of the form [22]

$$\tilde{\mathbf{P}}(\mathbf{r}, \omega) = \epsilon_0 \left(\chi^{(1)} \cdot \tilde{\mathbf{E}}(\mathbf{r}, \omega) + \chi^{(2)} : \tilde{\mathbf{E}}(\mathbf{r}, \omega) \tilde{\mathbf{E}}(\mathbf{r}, \omega) + \chi^{(3)} \vdots \tilde{\mathbf{E}}(\mathbf{r}, \omega) \tilde{\mathbf{E}}(\mathbf{r}, \omega) \tilde{\mathbf{E}}(\mathbf{r}, \omega) + \dots \right), \quad (2.29)$$

with ϵ_0 being the permittivity of free space and χ^m being the m th-order of the susceptibility tensor. For low field strengths the higher orders can be neglected, which results in the case of linear optics. For high field strengths, as those typically achieved with ultrashort pulses, the higher orders, especially the second and third order terms, play an important role. There are plenty of different nonlinear effects, but the explanations in the following are restricted to two of the third order effects, which are those relevant for this work.

For many materials, the refractive index is dependent on the intensity $I(z, t) \sim |A(z, t)|^2$ due to the third order susceptibility. Assuming the material responds instantaneously to the pulse, the modified intensity-dependent refractive index is (for linearly polarized light) [22]

$$\tilde{n}(\omega, |A(z, t)|^2) \approx n(\omega) + \underbrace{n_2 |A(z, t)|^2}_{\Delta n} \quad \text{with} \quad n_2 = \frac{3\chi^{(3)}}{8n(\omega)}, \quad (2.30)$$

which is known as the optical Kerr effect. The $n(\omega)$ represents, as before, the dispersive weak-field refractive index and the coefficient n_2 is sometimes called the nonlinear refractive index. Consequently, the phase velocity depends on the temporal intensity profile and yields a time- and intensity-dependent phase shift

$$\phi(z, t) = \frac{\omega_0}{c} \tilde{n}(\omega, |A(z, t)|^2) z - \omega_0 t = \beta(\omega) z + \underbrace{n_2 |A(z, t)|^2 \frac{\omega_0}{c} z}_{\phi_{\text{NL}}(z, t)} - \omega_0 t \quad . \quad (2.31)$$

When propagating on length z through a medium, this additional nonlinear phase ϕ_{NL} modifies the spectrum of the pulse and typically broadens it. This effect is referred to as Self-Phase Modulation (SPM). Formally, an instantaneous frequency is introduced

$$\omega(t) = \frac{\partial \phi_{\text{NL}}(z, t)}{\partial t} - \omega_0 \quad . \quad (2.32)$$

⁸With the assumption of instantaneous response, the material is assumed to be lossless and dispersionless and the power series can be written in time domain in the same form as Eq. (2.29).

For the example of an ultrashort Gaussian pulse introduced in Eq. (2.9), the time-varying part of the frequency can be analytically determined:

$$\frac{\partial \phi_{\text{NL}}(z, t)}{\partial t} = -8 \ln(2) \frac{n_2 \omega_0 \hat{P}}{c \Delta t^2} z t \exp\left(-4 \ln(2) \frac{t^2}{\Delta t^2}\right) \quad . \quad (2.33)$$

The spectral influence of SPM is shown in Fig. 2.5a for a pulse with $\Delta t = 900$ fs travelling through $L = 1$ m of silica. In contrast to the effect of dispersion, where the frequency dependency of the refractive index modifies the pulse in time domain, SPM modifies the pulse in frequency domain. A quantitative measure of the total accumulated phase due to SPM is the so called B -integral. It is defined by [23]

$$B = \gamma \int_0^L |A_{\text{max}}(z, t)|^2 dz \quad \text{with} \quad \gamma = \frac{n_2 \omega_0}{c A_{\text{eff}}} \quad , \quad (2.34)$$

where γ is the nonlinear parameter [16], A_{eff} the effective mode-field area and L the total length of the medium. It describes the accumulated nonlinear phase coupled to the temporal evolution of the pulse within the interaction length in the medium. It is convenient to use the maximum B -integral as a parameter to characterize the propagation through a medium, which corresponds to the total accumulated nonlinear phase of the pulse peak, given by $\hat{P}(z)$.

While SPM describes the influence of nonlinearities for one optical field, the consideration must be extended if two or more fields are present having different propagation directions, frequencies or polarization states. These fields interact with each other through nonlinearities and they can, for example, generate new fields due to the effect of four-wave mixing [16]. Ignoring such effects, these fields can also interact with each other without any energy transfer, via Cross-Phase Modulation (XPM). Considering the more general case for the interaction of two co-propagating fields with different polarization states and different frequencies, the total field is given by

$$\mathbf{E}(\mathbf{r}, t) = \frac{1}{2} \{ [A_{1x}(z, t) \hat{\mathbf{x}} + A_{1y}(z, t) \hat{\mathbf{y}}] \exp [i(k(\omega_1)z - \omega_1 t)] + [A_{2x}(z, t) \hat{\mathbf{x}} + A_{2y}(z, t) \hat{\mathbf{y}}] \exp [i(k(\omega_2)z - \omega_2 t)] \} + c.c. \quad . \quad (2.35)$$

After a lengthy calculation, when plugging Eq. (2.35) in Eq. (2.29), assuming that the medium has instantaneous response and, since a phase-matching condition is not generally satisfied, neglecting those terms oscillating at new frequencies generated via four-wave mixing, an additional nonlinear contribution to the refractive index is obtained, given by [16]

$$\Delta n_{1p} = n_2 \left(|A_{1p}(z, t)|^2 + 2 |A_{2p}(z, t)|^2 + \frac{2}{3} |A_{1q}(z, t)|^2 + \frac{2}{3} |A_{2q}(z, t)|^2 \right) \quad (2.36)$$

$$\Delta n_{2p} = n_2 \left(|A_{2p}(z, t)|^2 + 2 |A_{1p}(z, t)|^2 + \frac{2}{3} |A_{1q}(z, t)|^2 + \frac{2}{3} |A_{2q}(z, t)|^2 \right) \quad , \quad (2.37)$$

with $p = x, y$ and $q = x, y$ such that $p \neq q$. As can be seen, the refractive index variation is not only caused by SPM (the first term in the brackets), but it is also accompanied by the influence due to the presence of another field, caused by XPM (the last terms in the brackets). The SPM

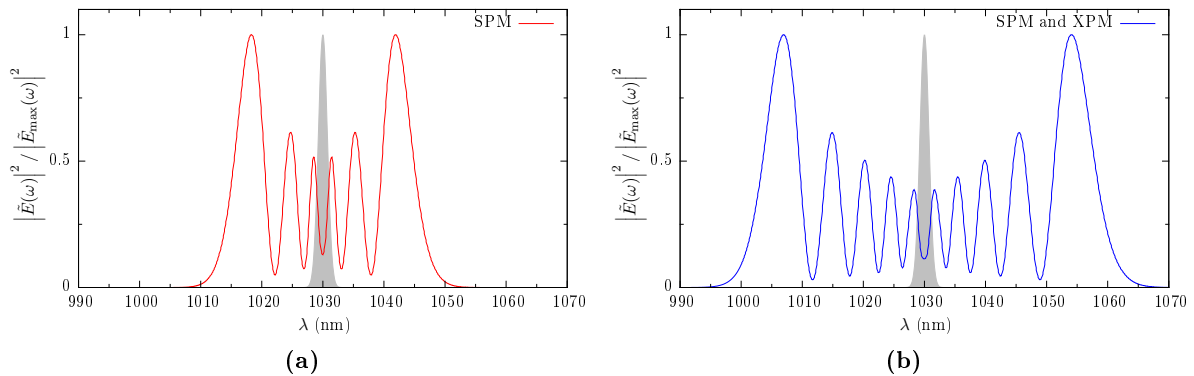


Fig. 2.5: Representation of the spectral influence of (a) SPM alone ($\hat{P}_1 = 8 \text{ kW}$) and (b) XPM and SPM ($\hat{P}_2 = 10 \text{ kW}$), for pulses with $\Delta t = 900 \text{ fs}$ travelling through $L = 1 \text{ m}$ silica ($n_2 = 2.7 \cdot 10^{-20} \text{ m}^2 \text{ W}^{-1}$).

term is just driven by the same field in the same polarization state. In contrast, the XPM terms are a mixture of the contributions from the perpendicular polarization component of the same field and the orthogonal polarization components of the other fields. If both fields are identically linearly polarized, the impact of XPM is twice as strong as that of SPM. The origin of the factor of $2/3$ lies in the symmetry properties of the $\chi^{(3)}$ tensor⁹ (weak birefringence). It increases to a factor of two when using circularly polarized light instead of linearly polarized light. Of course, Eq. (2.36) and Eq. (2.37) are also valid if both fields oscillate at the same frequency. For the nonlinear phase it follows

$$\phi_{\text{NL},1\text{p}}(z, t) = \frac{n_2 \omega_0}{c} z \left(|A_{1\text{p}}(z, t)|^2 + 2 |A_{2\text{p}}(z, t)|^2 + \frac{2}{3} |A_{1\text{q}}(z, t)|^2 + \frac{2}{3} |A_{2\text{q}}(z, t)|^2 \right) \quad (2.38)$$

$$\phi_{\text{NL},2\text{p}}(z, t) = \frac{n_2 \omega_0}{c} z \left(|A_{2\text{p}}(z, t)|^2 + 2 |A_{1\text{p}}(z, t)|^2 + \frac{2}{3} |A_{1\text{q}}(z, t)|^2 + \frac{2}{3} |A_{2\text{q}}(z, t)|^2 \right) \quad (2.39)$$

To obtain the total accumulated nonlinear phase one has to integrate again over the interaction length, as done in Eq. (2.34), which results in B for SPM and a more complicated expression for XPM, since the overlap of the pulses must be considered. The accumulated phases $\phi_{\text{NL},1}$ and $\phi_{\text{NL},2}$ can be different if $|A_1(z, t)|^2 \neq |A_2(z, t)|^2$, but they are predominantly driven by XPM due to the factor of two in the case of identical linearly polarized fields. As an example, the additional spectral influence of a second co-propagating and perpendicularly polarized pulse with equal pulse duration but different peak power is shown in Fig. 2.5b. As can be seen, the second pulse broadens the already SPM-broadened spectrum of the first pulse even further. For the case of counter-propagating pulses the interaction time is shorter. This leads to a weaker total accumulated XPM phase.

Up to now, the transverse extension of the pulse was neglected. But when very high laser power propagates through a nonlinear medium, the effect of self-focusing sets an upper limit. Due to the intensity-dependent refractive index, the phase velocity changes across the spatial

⁹For isotropic media, such as silica, only three elements of the fourth-rank tensor are independent. Those three elements have approximately the same order of magnitude, since the dominant contributions are of electronic origin [16].

intensity profile leading to a focusing effect, which is referred to as the spatial Kerr effect. The critical power for catastrophic self-focusing, which leads to the destruction of the medium, can be estimated by [24]

$$P_{\text{cr}} = \alpha \frac{\lambda_0^2}{4\pi n(\omega) n_2} \quad , \quad (2.40)$$

where α is a material-independent parameter ranging from 1.84 [22] to 1.9 [24] for a Gaussian beam shape. As a result, the maximum peak power for silica (and linearly polarized light) is $P_{\text{cr}} \approx 4 \text{ MW}$ for a wavelength in the range of $1 \mu\text{m}$ (and n_2 in the range of $2.2 \cdot 10^{-20} \text{ m}^2 \text{ W}^{-1}$ [16] to $3.2 \cdot 10^{-20} \text{ m}^2 \text{ W}^{-1}$ [22]).

3 Beam Combining

As mentioned at the beginning, the development of high-power solid-state laser systems with diffraction-limited beam quality is a challenging task, since limitations are set by nonlinear and thermal effects, which may cause spatial, temporal and spectral distortions in the Continuous Wave (CW) or pulsed laser beam. An alternative approach to scale the performance of such laser systems even further, in spite of these limitations, is to combine the performances of single laser units operating at power levels below the onset of these detrimental effects. Thereby it is possible to obtain a superposed output with the properties of each single unit but operating well above the limit of a single laser. There are plenty of different techniques, which may be classified into two main classes called Incoherent Beam Combining (IBC) and CBC [8]. Moreover, it is possible to further subdivide them into implementations, which benefit from separating different processes, such as the amplification, either spatially, temporally or spectrally. In the following, different beam combining techniques will be explained in more detail, whereby the focus will be set on CBC.

3.1 Incoherent Beam Combining

In the case of IBC such single units are independent laser sources in which the relative phases are not controlled. Consequently, the individual beams do not interfere but are simply spatially overlapped. Therefore, this type of combining consists of a simple addition of powers, which is just viable when using CW lasers or pulsed lasers with pulse durations not shorter than several nanoseconds, since shorter pulses cannot be efficiently overlapped in time using conventional electronic delays. With these techniques it is possible to combine several individual lasers spatially or spectrally in a serial or parallel manner.

Conventional one- or two-dimensional diode-laser arrays use IBC. A certain number of laser diodes are stacked together side-by-side, resulting in an addition of the average output powers of each emitter. For the case of incoherent superposition the interference term of Eq. (2.21) vanishes. Thus, in principle, the scaled total output of N lasers can be written as

$$\bar{P}_{\text{comb}}(\mathbf{r}, \lambda) = \sum_{m=1}^N \bar{P}_m(\mathbf{r}, \lambda_m) \quad , \quad (3.1)$$

where \bar{P}_m are the average output powers of each single emitter operating at the same wavelength $\lambda_m = \lambda$. The adjacent output near-field beams are smeared together in the far field, but the total beam quality is relatively low. Such devices are of interest for pumping multikilowatt solid-state

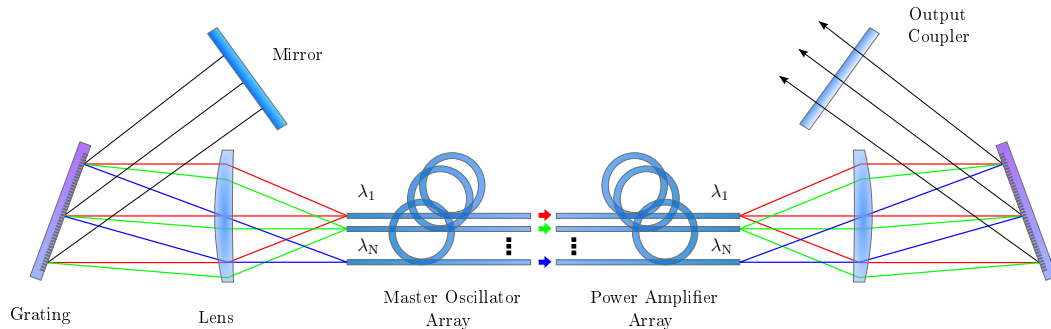


Fig. 3.1: Schematic representation of a MOPA architecture using SBC (after [8]).

lasers such as, for example, rare-earth-doped fiber lasers [8, 25].

On the other hand, these array elements may operate at different wavelengths λ_m , which additionally scales the spectral width [25]. This principle is known as Spectral Beam Combining (SBC). Hereby individual beams with non-overlapping spectra are combined with the help of wavelength-sensitive elements. If the spectra would overlap, the relative phases would need to be controlled for efficient combination. This, in turn, would be CBC. Wavelength-sensitive elements are, for example, prisms or diffraction gratings, which deflect the spatially separated beams according to their wavelength so that they overlap after the wavelength-sensitive element and subsequently propagate along the same path. Other examples are dichroic filters or Volume Bragg Gratings (VBGs), which possess wavelength-dependent transmission and which are able to combine the beams in a serial manner. These approaches can be applied to various laser sources, such as the afore mentioned laser diodes [25] or fiber amplifiers [26, 27]. Fig. 3.1 shows schematically the spectral combination of an array of fiber lasers with a subsequent amplification stage in a Master Oscillator Power Amplifier (MOPA) arrangement using two diffraction gratings.

The advantage of SBC is that the combined beams do not require mutual temporal coherence, which eliminates complicated methods of phase stabilization and makes the operation at high power levels more stable. But in order to achieve stable operation and high combining efficiency, it is necessary to control the spectra of the single emitters which is challenging. If the number of elements for a certain bandwidth increases, the spectral spacing between the elements will decrease. This makes the manufacturing of efficient steep-edge filters difficult. Furthermore, in a serial implementation using filters, the first laser of the array accumulates the largest number of bounces, which puts tight tolerances on the angular positioning. For parallel implementations using gratings, the tight positioning tolerances also hold and they additionally need to have sufficient dispersion, for example angular dispersion, to combine widely-separated wavelengths. Moreover, lasers with narrow bandwidths are required, since in the case of broadband lasers the dispersive elements imprint a spatial chirp, which means that different spectral components in a beam become spatially dispersed, resulting in a degraded output beam quality. But there are also proposals to compensate for the chirp with a staircase mirror or a VBG [8, 26, 28].

This was just a short overview of IBC, but it will not be further considered in this work, since these implementations are not suitable for ultrashort pulses. In the following, CBC and possible

implementations thereof will be explained.

3.2 Coherent Beam Combining

In the case of CBC the afore mentioned single laser units are coherent to each other, since the relative phases are controlled. All units operate at the same wavelength and they are combined in such a way that they interfere constructively. The fundamental difference with IBC is that instead of a simple addition of powers each contribution of an unit is added vectorally. This results in a total output of

$$P_{\text{comb}}(\mathbf{r}, t) = C \left| \sum_{m=1}^N \mathbf{E}_m(\mathbf{r}, t) \right|^2 \quad (3.2)$$

with $P(\mathbf{r}, t) = C |\mathbf{E}(\mathbf{r}, t)|^2 \sim I(\mathbf{r}, t)$ and C containing all constant factors. Efficiently combining the outputs in a way that they interfere constructively imposes strong requirements on the control of the relative phases, the state of polarization and the amplitudes at every instant in time [8]. In general, CBC can be divided into two subgroups, which are characterized by the kind of output composition: tiled-aperture and filled-aperture implementations.

3.2.1 Tiled-Aperture and Filled-Aperture Implementation

In tiled-aperture implementations, the outputs of the single laser units are arranged adjacent to each other forming an array of emitters. Consequently, interference and, therefore, combination of the individual beams, occurs only in the far field. In principle, this can be thought of as a synthesized plane wave [8]. Fig. 3.2a shows an example of an one-dimensional fiber amplifier array. Due to the space between the single emitters, disturbing side lobes emerge in the far field beam profile. Therefore, the filling factor of the array should be maximized, which means that the spaces between the tiles should be minimized. To demonstrate this effect, an example of an one-dimensional laser array emitting Gaussian beams (which are all in phase) is considered. This can be expressed as

$$A(x, z = 0) = \left[\sum_{m=-\infty}^{\infty} \delta(x - m\Delta x) * A_0 \exp\left(-\frac{x^2}{w_0^2}\right) \right] \Pi\left(\frac{x}{\delta x}\right) \quad , \quad (3.3)$$

where the first term is a series of Dirac delta functions (δ) shifted by Δx , the second term is a Gaussian profile with beam radius w_0 and amplitude A_0 which, by virtue of the convolution ($*$), is placed at each position designated by the Dirac deltas. The rectangular function Π defines a window with width δx to confine the infinite series of delta functions to a certain dimension (and

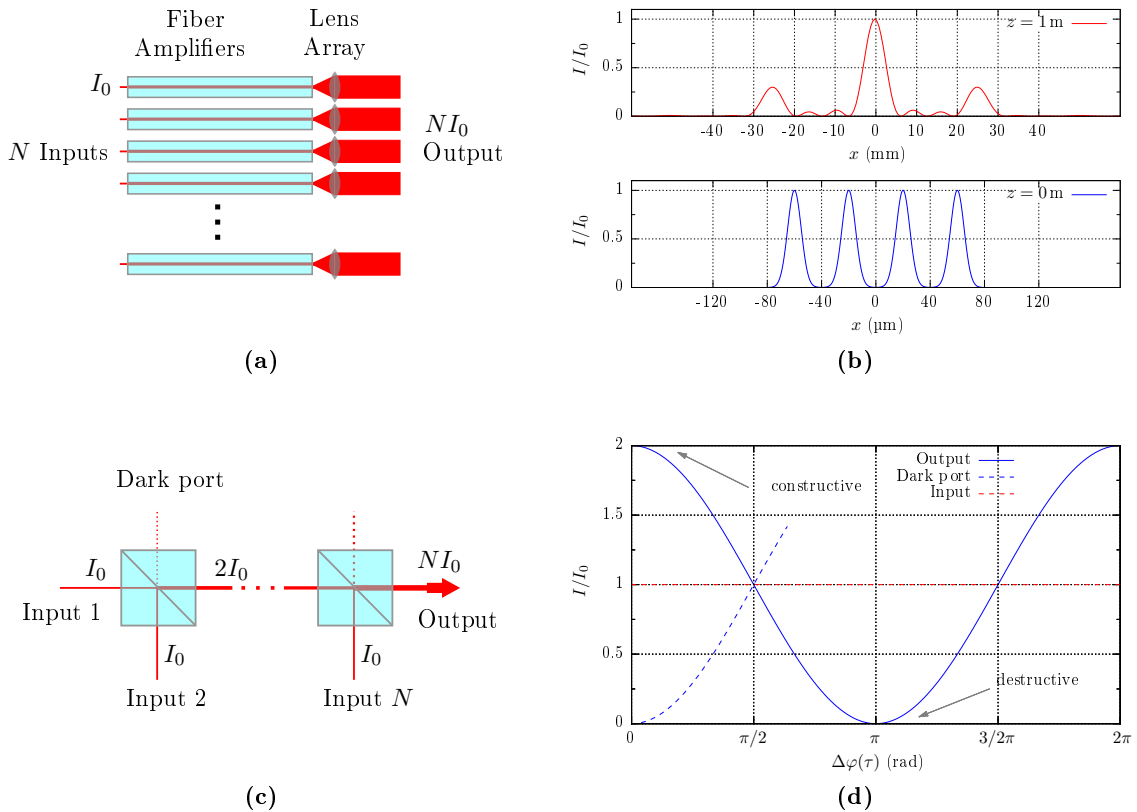


Fig. 3.2: (a) Scheme of the tiled-aperture approach and (b) corresponding spatial intensity distribution at the emission plane and after a distance $z = 1$ m. (c) Representation of the filled-aperture approach and (d) the influence of interference.

therefore the number of beams). Propagating this by means of the Fresnel diffraction integral

$$A(x, z) = \frac{\exp\left(\frac{i k}{2} z\right)}{\sqrt{i \lambda z}} \int_{-\infty}^{\infty} A(x', 0) \exp\left(\frac{i k}{2 z} (x - x')^2\right) dx' \quad (3.4)$$

and using the Fraunhofer approximation, the resulting far field is

$$A(x, z) \sim \left\{ \sum_{m=-\infty}^{\infty} \delta\left(\frac{k}{z} x - \frac{m}{\Delta x}\right) \exp\left[-\left(\frac{k x}{2 z}\right)^2 w_0^2\right] \right\} * \text{sinc}\left(\delta x \frac{k x}{z}\right) . \quad (3.5)$$

This is exemplarily shown in Fig. 3.2b for an array of $N = 4$ emitters (with an appropriate window size given by the number of sample points, the beam radii of $w_0 = 10 \mu\text{m}$ and a separation of $\Delta x = 40 \mu\text{m}$) after a propagation distance of $z = 1$ m. As can be seen, disturbing side lobes are generated, which grow as the distance between the emitters increases. In the case of optical fibers, the maximum filling factor for such a two-dimensional arrangement is achieved for a hexagonal configuration [29]. In general, the tiled-aperture approach leads to a larger beam size and to a reduced divergence. An experimental implementation is given in [30].

In the filled-aperture implementations the spatially separated beams are superimposed with a

beam combiner, which is equivalent to an inverse beam splitter. Consequently, interference occurs in the near field. Beam combiners are, for example, beam splitters, $N \times 1$ fiber couplers, gratings, and other diffractive optical elements. As an example, two monochromatic linearly polarized (one-dimensional) fields, according to Eq. (2.1), are considered, which are combined with the help of a non-polarizing ideal beam splitter. The superposed field is given by

$$E(z, t) = \frac{1}{2} \{E_{01} \exp [i\varphi(\tau_1)] + E_{02} \exp [i\varphi(\tau_2)]\} \exp [i(k(\omega_0)z - \omega_0 t)] + c.c. \quad , \quad (3.6)$$

where φ_m are the accumulated phases of the two fields. For identical amplitudes $E_{0m} = E_0$ and phase delays of $\tau_2 = \tau$ and $\tau_1 = 0$, the expression for interference, given by Eq. (2.21), simplifies to

$$I = 2I_0 \{1 + |\gamma(\tau)| \cos [\Delta\varphi(\tau)]\} \quad . \quad (3.7)$$

In the case of fully coherent fields $|\gamma(\tau)| = 1$. For constructive interference $\Delta\varphi(\tau) = 0$ and, therefore, the total intensity is, due to the additional interference term, not only the sum of the intensities of each field, but four times the intensity $I = 4I_0$ instead. However, when using a beam splitter as the combining element (50:50 splitting ratio) a factor of 1/2 must be considered for each beam, which reduces the output by a factor of 2 in Eq. (3.7) and results in $I = 2I_0$. Fig. 3.2c shows in principle the coherent combining process when using ideal beam splitter cubes as combining elements. If there is constructive interference both inputs will be added at one output port of the cube. Consequently, at the remaining port (which is called the dark port) destructive interference occurs. The interference and, hence, the output intensities depend on the phase delays of the input beams, which is represented in Fig. 3.2d. An experimental implementation of this scheme can be found in [9]. Generally, the combined on-axis output intensity scales with N for both tiled- and filled-aperture implementations. It is usual to define the combining efficiency as the ratio of the combined output power to the total input power. Considering cascaded beam splitters, the combining efficiency for fields according to Eq. (2.1), can be expressed as

$$\eta_{\text{comb}} = \frac{\left\langle \left| \sum_{m=1}^N \sqrt{\eta_m \kappa_m} \mathbf{E}_m(\mathbf{r}, t) \right|^2 \right\rangle}{\sum_{m=1}^N \langle |\mathbf{E}_{0m}|^2 \rangle} = \frac{\sum_{m=1}^N \bar{P}_m^{\text{out}} + \sum_{\substack{n=1 \\ n \neq m}}^N \sum_{m=1}^N \sqrt{\bar{P}_n^{\text{out}} \bar{P}_m^{\text{out}}} |\gamma_{nm}| \cos(\Delta\phi_{nm})}{N \sum_{m=1}^N \bar{P}_m^{\text{in}}} \quad (3.8)$$

with $\bar{P}_m^{\text{in}} = C \langle |\mathbf{E}_{0m}|^2 \rangle$ being the average input powers and $\bar{P}_m^{\text{out}} = \eta_m \kappa_m \bar{P}_m^{\text{in}}$ being the output powers, where η_m are the combiner losses and κ_m the splitting ratio [31, 32]. For the two inputs of a beam splitter $\kappa_1 = \kappa$ and $\kappa_2 = 1 - \kappa_1$. As can be seen, the efficiency gets maximized when $|\gamma_{nm}| = 1$ and the total phase difference $\Delta\phi = 0$.

3.2.2 Approaches to Coherent Beam Combining

There are many different implementations to coherently combine beams both spatially and temporally, which will be briefly explained in the following.

The first one is the common-resonator approach. In this case, the single laser units consist of an array of gain elements, which are placed inside a single bulk resonator. With the help of the feedback from the resonator all the elements are coupled together. The difficulty of this approach is to maintain lowest-order transverse-mode operation, as the power increases. This has been successfully demonstrated using CO₂ lasers [8].

Another approach is the evanescent-wave or leaky-wave coupling. For this, the distances between the single laser units, which are again an array of gain elements, are sufficiently small so that their evanescent field distributions overlap, which causes a coupling between the elements. A disadvantage of this method is that phase errors occur between adjacent elements making it challenging to obtain equal phases at the outputs of the array elements. This poses difficulties when scaling to large array sizes. This has been applied to fiber lasers, but particularly to phase-locked laser diode arrays [8, 33, 34].

A third approach is the self-organizing approach, in which the single laser units are oscillators each having very different path lengths. With the help of the feedback from all the other oscillators, every resonator is coupled to all the others. This approach is also called self-injection seeding. For example, an oscillator without any seed would operate on multiple longitudinal modes and the power distribution of those modes would fluctuate. Using a seed with a frequency near a resonance would force the operation of the oscillator on that mode with much higher power. Through the coupling of, for example, two oscillators an overall resonator is obtained having an additional resonance condition for the longitudinal modes. Therefore, just the modes satisfying this condition will be amplified. Because of this it is not possible to create ultrashort pulses with this approach. Typically, this is implemented with fiber lasers. However, the combining efficiency seems to decrease when scaling to a large number of elements [8, 35].

There are additionally nonlinear optical approaches involving phase conjugation and Raman beam combining. The method of phase conjugation relies on Stimulated Brillouin Scattering (SBS), which requires lasers with relatively high peak power. In the case of Raman beam combining, a certain number of beams are coupled into a fiber, which in sum excite through Stimulated Raman Scattering (SRS) the Stokes beam. Both concepts appear to be difficult for scaling to high power levels [8, 36, 37].

A further approach is the use of an enhancement cavity. For this concept an external resonator is used, which is seeded by a pulsed laser source. In that case, the afore mentioned single units that should be combined coherently are not beams from spatially separated lasers but successive pulses from the seed laser. The round-trip time of the resonator and the pulse repetition rate of the seed laser are matched so that the successive pulses are coherently superposed, which leads to an enhancement of the circulating pulse inside the resonator. This scales the peak power of the pulse significantly. There are different techniques to couple out that power; however, this introduces losses and limits the achievable enhancement. The repetition rate of the out-coupled

power is limited, since the cavity must be reloaded and the average output power is not scaled. But this approach is viable for ultrashort pulses [38].

Finally, an active-feedback implementation can be used, by which the differences in the path lengths of the different laser units are kept identical. These differences are detected and a feedback system is used to equalize possible variations of the path lengths with modulo 2π . Such an implementation has been used typically in MOPA architectures. Thereby the output beam of a seed laser is divided into a certain number of beams, which are distributed on spatially separated amplifiers. Afterwards those amplified outputs are combined coherently. To obtain efficient combining, an active stabilization system is needed. There are different possibilities to actively lock the phases. In general, an error signal is generated, which is fed back to a phase-controller, for example a delay line. This can be used to lock laser channels pairwise. With the Hänsch-Couillaud method [39] the change in the magnitude of the output amplitude can be detected as a function of the state of polarization. Another technique is the Pound-Drever-Hall method [40], by which the output is phase modulated and, with the help of the occurring side bands, the frequency is stabilized on the resonance frequency of a fixed resonator. Moreover, a Stochastic Parallel Gradient Descent (SPGD) algorithm can be used to maximize the on-axis intensity by controlling the phase modulators. This has been applied to both CW and pulsed operation, with which a successful scaling of the average output power and the pulse energy, respectively, beyond the afore mentioned limitations may be achieved [41, 42]. Particularly, the use of fiber-based amplifiers for the amplification of ultrashort pulses [9] is of interest for this work.

There are also approaches using both SBC and CBC. For this, single-frequency seed lasers are spectrally combined and afterwards amplified in an all-fiber-based system, to suppress the limiting effect of SBS. Subsequently, this signal is amplified in spatially separated amplifiers and coherently combined [43].

In the following, the focus is set on a particular active-feedback approach: the polarization beam combining. It will be considered using ultrashort pulses and fiber-based amplifiers in a MOPA architecture. Furthermore, a special temporal approach which uses temporal separation of pulses, the so-called DPA, will be explained.

3.2.3 Polarization Beam Combining

Polarization beam combining [44] is a special approach to the filled-aperture implementation. In this case, the beam splitters shown in Fig. 3.2c are polarization-dependent. Consequently, an incident arbitrarily polarized electromagnetic field is divided into its s - and p -polarization components. As an example, if the incident field is linearly polarized with an angle of 45° , the amplitude will be split (in an ideal beam splitter) into two parts of equal magnitude, but the p -component will be transmitted and the s -component will be reflected. The same happens if the incident field is circularly polarized, apart from the additional phase of one of the components. To coherently combine several laser units, e.g. fiber amplifiers, a beam splitter must divide

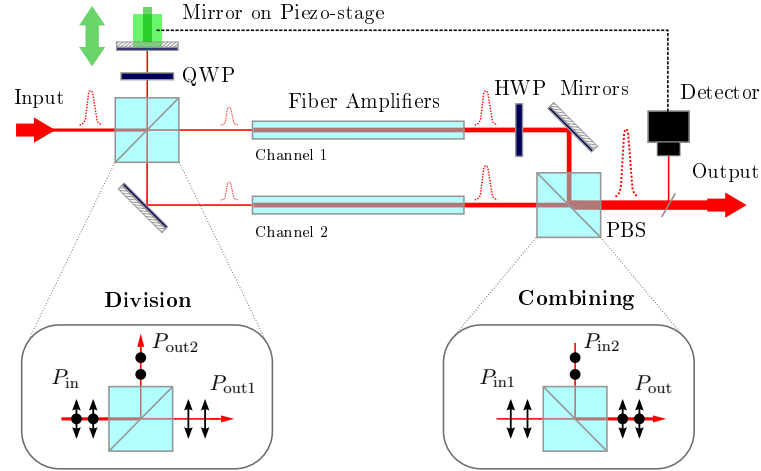


Fig. 3.3: CBC of two fiber amplifiers with a Mach-Zehnder type interferometer in a filled-aperture implementation with active-feedback.

one seed signal into several replicas and another (inverse) beam splitter must combine them again after amplification [45]. Considering two of such channels, a so-called Mach-Zehnder type interferometer seems to be advantageous. As shown in Fig. 3.3, an input pulse is split into two orthogonal polarized parts, which are amplified in two separate fiber amplifiers and which are afterwards recombined. To efficiently recombine ultrashort pulses they do not only need to overlap in space but also in time. Therefore, an active-feedback system controlling a piezo-driven delay line is usually employed to match the two optical paths. While the p -polarized component is transmitted through the first channel, the s -polarized component is reflected into the delay line. In a double-pass QWP (which behaves as a HWP) the polarization of the pulse will be rotated by 90° before passing the beam splitter a second time before arriving at the second channel. After amplifying both channels, a HWP rotates the polarization of the pulse passing through the first channel into the s -polarization, so that both are combined at the second beam splitter. If the pulses are not ideally linearly polarized in their respective axis, some amount of energy gets lost at the dark port.

To describe the process of division (combining) mathematically the Jones matrix of a Polarization Beam Splitter (PBS) must be defined. By using the Jones matrix of a linear polarizer (Tab. 2.1), a PBS can be described in a general case as

$$\mathbf{J}_{\text{PBS}} = \begin{cases} \mathbf{J}_{\text{T}} = \begin{pmatrix} \sqrt{T_p} & 0 \\ 0 & \sqrt{1-R_s} \end{pmatrix} \\ \mathbf{J}_{\text{R}} = i \begin{pmatrix} \sqrt{1-T_p} & 0 \\ 0 & \sqrt{R_s} \end{pmatrix} \end{cases} \quad \text{with} \quad |\mathbf{J}_{\text{T}}|^2 + |\mathbf{J}_{\text{R}}|^2 = \mathbf{I} \quad , \quad (3.9)$$

where \mathbf{J}_{T} and \mathbf{J}_{R} are matrices for the transmitted and reflected parts, respectively, with the transmissivity T_p of the p -component and the reflectivity R_s of the s -component. For \mathbf{J}_{R} a phase jump of $\pi/2$ must be considered (according to Appendix B), which is $\exp(i\pi/2) = i$. With these matrices the power is conserved, since the sum of the absolute squares of both matrices results in the unit matrix \mathbf{I} . If the PBS possesses additional losses, a factor of $\sqrt{\eta}$ must be multiplied

to both matrices. But then for the sum of the absolute squares of both matrices the unit matrix is no longer obtained. Furthermore, for setups including mirrors, one has to mind a phase jump at each of them. In an ideal case, where no influences due to losses (then again a certain factor $\sqrt{\eta}$ must be introduced), angles of incidence or polarizations are considered, a phase jump of π occurs at each mirror, where $\exp(i\pi) = -1$. Consequently, a Jones matrix for an ideal and lossless mirror can be written as

$$\mathbf{J}_M = \begin{pmatrix} -1 & 0 \\ 0 & -1 \end{pmatrix} . \quad (3.10)$$

When considering an input pulse $\mathbf{E}(\mathbf{r}, t)$ and using Eq. (3.9), the fields in both channels before the second PBS as shown in Fig. 3.3 are given by

$$\mathbf{E}_1(\mathbf{r}, t) = \mathbf{J}_M \mathbf{J}_{\text{HWP}}(\theta) \sqrt{G_1} \mathbf{J}_T \mathbf{E}(\mathbf{r}, t) \quad (3.11)$$

$$\mathbf{E}_2(\mathbf{r}, t) = \sqrt{G_2} \mathbf{J}_M \mathbf{J}_T \mathbf{J}_{\text{QWP}}(\theta) \mathbf{J}_M \mathbf{J}_{\text{QWP}}(\theta) \mathbf{J}_R \mathbf{E}(\mathbf{r}, t) , \quad (3.12)$$

with the constant gain G_m in each channel as a simplified representation (neglecting all other influences of the amplifiers). Ideally the rotation angle of the optical axis for both the HWP and the QWP is $\theta = 45^\circ$ with respect to the s -component (y -axis) in order to rotate the linearly polarized fields by 90° . The combined output field is

$$\mathbf{E}_{\text{comb}}(\mathbf{r}, t) = \mathbf{J}_R \mathbf{E}_1(\mathbf{r}, t) + \mathbf{J}_T \mathbf{E}_2(\mathbf{r}, t) . \quad (3.13)$$

Since real PBSs do not divide the input pulse ideally, there are also components, ejected at the dark port. Hence, the loss at the second PBS is given by

$$\mathbf{E}_{\text{loss}}(\mathbf{r}, t) = \mathbf{J}_T \mathbf{E}_1(\mathbf{r}, t) + \mathbf{J}_R \mathbf{E}_2(\mathbf{r}, t) . \quad (3.14)$$

Due to the energy conservation, the sum of the absolute squares of both the combined output field and the loss at the dark port must result in the absolute square of the input field. This is not the case yet, since the initial loss of $\mathbf{E}_2(\mathbf{r}, t)$ for its second pass through the first PBS is still missing, which is

$$\mathbf{E}_{\text{back}}(\mathbf{r}, t) = \mathbf{J}_R \mathbf{J}_{\text{QWP}}(\theta) \mathbf{J}_M \mathbf{J}_{\text{QWP}}(\theta) \mathbf{J}_R \mathbf{E}(\mathbf{r}, t) . \quad (3.15)$$

Then, the energy conservation reads $|\mathbf{E}(\mathbf{r}, t)|^2 = |\mathbf{E}_{\text{comb}}(\mathbf{r}, t)|^2 + |\mathbf{E}_{\text{loss}}(\mathbf{r}, t)|^2 + |\mathbf{E}_{\text{back}}(\mathbf{r}, t)|^2$. Thus the setup exhibits an initial loss which is mainly determined by T_p and R_s .

In the case of lossless PBSs with $\eta = 0$ and with a 45° linearly polarized input pulse (fully polarized):

$$\mathbf{E}(\mathbf{r}, t) = \frac{1}{2} \left\{ \frac{A(z, t)}{\sqrt{2}} (\hat{\mathbf{x}} + \hat{\mathbf{y}}) \exp[i(k(\omega_0)z - \omega_0 t)] \right\} + c.c. , \quad (3.16)$$

and no additional phase changes in the channels that $\Delta\phi = 0$ (disregarding the phase jumps due to the elements), the power at the combined output and at the dark port, by using Eq. (2.19),

Eq. (3.9) and Eq. (3.10), are

$$P_{\text{out}}(z, t) \approx C \frac{R_s T_p}{2} (G_1 + G_2 T_p) |A(z, t)|^2 \quad (3.17)$$

$$P_{\text{loss}}(z, t) \approx C \frac{R_s T_p}{2} (1 - T_p) G_2 |A(z, t)|^2 \quad (3.18)$$

whereby all terms including $(1 - R_s)$ were neglected to simplify the complex expression since typically $R_s > 99\%$. As can be seen, the amount of the loss $P_{\text{loss}}(z, t)$ for that nearly ideal case is mainly determined by the magnitude of T_p . When considering the perfectly ideal case $R_s = T_p = 100\%$. Then by using Eq. (2.17), one obtains the dependence of the orientation angle of the linearly polarized output on the gain factors of each channel, which is

$$\tan(2\psi) = \frac{2\sqrt{G_1 G_2}}{G_2 - G_1} \quad (3.19)$$

For different gain factors and also for $R_s = T_p \neq 100\%$ the orientation angle of the linear polarization of the output pulse is different from 45° . However, for the perfectly ideal case and if $G_1 = G_2 = G$ the orientation angle of the output polarization is $\psi = 45^\circ$ and the combined output power will be $P_{\text{out}}(z, t) = CG |A(z, t)|^2$.

Until now just perfect linearly polarized light was considered and influences due to additional phase terms were neglected. However, in reality this is not the case since the pulses in the separate amplifiers may accumulate different phases, for example due to path length differences and nonlinear effects. These different phases result, in turn, in changes in the state of polarization of the combined beam. For this reason the Degree of Linear Polarization (DOLP) can be used as a measure of the quality of the combination. It is given by the maximum and minimum output powers \bar{P}_{max} and \bar{P}_{min} , respectively, which are transmitted through an additional rotating polarizer at the output, and is defined as [45]

$$\text{DOLP} = \frac{\bar{P}_{\text{max}} - \bar{P}_{\text{min}}}{\bar{P}_{\text{max}} + \bar{P}_{\text{min}}} \quad (3.20)$$

The DOLP describes the amount of linear polarization over a certain time and ranges from zero to one, which corresponds to circularly or linearly polarized light, respectively. It should be noted that the minimum value of zero can just be achieved, if the powers of the channels to be combined are equal. Thus, the DOLP is not well suited to characterize the combination of channels with significantly different powers. Therefore, it is useful to define additionally a total system efficiency, which measures the overall combined linearly polarized output. For this, a linear polarization efficiency can be used, which can be written as

$$\eta_{\text{LP}} = \frac{\bar{P}_{\text{max}}}{\bar{P}_{\text{max}} + \bar{P}_{\text{min}}} \quad (3.21)$$

It gives the percentage of linearly polarized output power. In addition, the combining efficiency, after Eq. (3.8) compared to Eq. (3.2), relates the combined output power and the input power.

Using this, the total system efficiency can be expressed finally by

$$\eta_{\text{tot}} = \eta_{\text{LP}}\eta_{\text{comb}} \quad . \quad (3.22)$$

Both the DOLP and the total system efficiency should be used to evaluate the combined output, since just one statement is not sufficient. While the former shows mainly the occurrence of possible phase differences between the pulses, the latter shows possible power losses due to the combining process.

In the following another approach will be described, which relies on the temporal separation of pulses. This idea will be used in this work.

3.2.4 Divided-Pulse Amplification

As described in Section 2.4, an ultrashort pulse propagating through a medium accumulates a certain nonlinear phase shift that depends on its peak power. This nonlinear phase shift may lead to spectral and temporal distortions. To mitigate these effects the peak power during amplification should be reduced. This can be done using the afore mentioned CPA technique and the CBC approach. Another possibility is the Divided-Pulse Amplification (DPA) [11] approach, which, in contrast to CBC, relies not on a spatial but on a temporal separation of the pulses instead. An initial pulse is divided into N non-temporally overlapping copies, which are then amplified and subsequently recombined to obtain one single intense output pulse.

The division and recombination process is achieved, for example, in birefringent crystal stacks. These stacks consist of a sequence of crystals with alternating orientations of the optical axis, with those at odd- or even-numbered positions are oriented at an angle of 45° or 0° , with respect to the linearly polarized input pulse, respectively. Due to birefringence, at each crystal a pulse is split into two equally intense, orthogonally polarized replicas, which are referred to as the ordinary and the extraordinary pulses. According to Eq. (2.18), both pulses propagate with different speeds. If the resulting propagation time difference is sufficiently large, the pulses will be separated in time by

$$\tau = L \left| \frac{1}{v_g^e} - \frac{1}{v_g^o} \right| \quad , \quad (3.23)$$

where v_g^e and v_g^o are the group velocities of the ordinary and the extraordinary pulses, and L is the length of the crystal. To obtain equally spaced, non-overlapping pulses, the length of the first and shortest crystal L_1 must be chosen so that $\tau > \Delta t$ (with Δt being the pulse duration), and the length of the m th subsequent crystals should be $L_m = 2^{m-1}L_1$. Consequently, a stack of M crystals produces 2^M orthogonally polarized pulses. After amplification, the pulses are coherently recombined with an inverse sequence of crystals. The polarization of the final output pulse is perpendicular to that of the input pulse. A schematic implementation of a crystal stack containing $M = 3$ crystals is depicted in Fig. 3.4.

An example of a birefringent material is Yttrium Vanadate (YVO_4), which produces a polarization delay of $\sim 1 \text{ ps mm}^{-1}$ [11]. Hence, the DPA approach is only practicable for pulses with

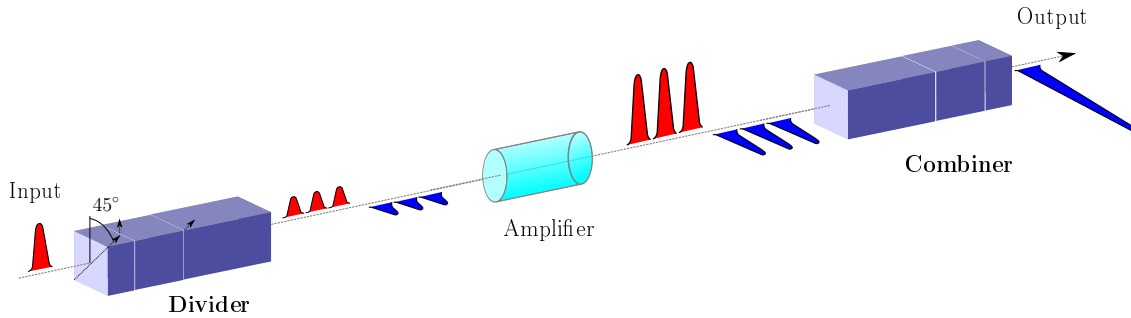


Fig. 3.4: Schematic representation of the dividing and combining process in a DPA implementation. Pulses colored in red are *s*-polarized and those colored in blue are *p*-polarized. For illustration purposes, the optical axes of the crystals in the divider are depicted.

pulse durations in the femto- and picosecond range, because only then the total length of a crystal stack is sufficiently short.

In the following a new implementation based on the idea of DPA will be presented. This new implementation allows for the use of nanosecond pulses and provides time delays in the nanosecond range. Furthermore, the afore explained approach of polarization beam combining will be used, but in a passive CBC scheme, which benefits from the advantage of not needing an active-feedback. This will also be detailed in the following section.

3.3 Passive Coherent Beam Combining

In this section the basic principle of the new implementation will be presented and theoretically investigated. Polarization beam combining is the backbone of the approach, but it will be transferred into a passive combining setup thus making an active-feedback redundant. Subsequently, this will be combined with the idea of DPA, which then results in the basic setup that allows the spatial and temporal division and combination of pulses.

As already mentioned in Section 3.2.2, there are coherent combining approaches that do not require active-feedback, as for example the self-organizing or field-coupling processes. Another possibility is to ensure that the spatially divided pulses propagate through identical optical paths in the separate channels. This can be achieved easily by using one common path, which can be done in a so-called Sagnac interferometer, as depicted in Fig. 3.5a. Here an input pulse is divided with the help of a beam splitter into two identical copies. If a PBS is used and the input pulse is linearly polarized under an angle of 45°, then it will be split into two identical copies, but the *p*-component will be transmitted and the *s*-component will be reflected. In general, using an input field $\mathbf{E}(\mathbf{r}, t)$, (Eq. (3.9) and Eq. (3.10)), the fields to be recombined from each channel can be expressed as

$$\mathbf{E}_1(\mathbf{r}, t) = \mathbf{J}_M^3 \mathbf{J}_T \mathbf{E}(\mathbf{r}, t) \quad (3.24)$$

$$\mathbf{E}_2(\mathbf{r}, t) = \mathbf{J}_M^3 \mathbf{J}_R \mathbf{E}(\mathbf{r}, t) \quad , \quad (3.25)$$

These fields, i.e. pulses, propagate clockwise and counter-clockwise through the Sagnac loop, that is they travel in different directions. After one round-trip, they recombine coherently at the PBS and, hence, travel again in the same direction. Due to the leakage of the PBS, the combined output is reduced by some losses, which corresponds to emission of energy at the input port. Both the combined output field and the lost field are given by

$$\mathbf{E}_{\text{comb}}(\mathbf{r}, t) = \mathbf{J}_T \mathbf{E}_1(\mathbf{r}, t) + \mathbf{J}_R \mathbf{E}_2(\mathbf{r}, t) \quad (3.26)$$

$$\mathbf{E}_{\text{loss}}(\mathbf{r}, t) = \mathbf{J}_R \mathbf{E}_1(\mathbf{r}, t) + \mathbf{J}_T \mathbf{E}_2(\mathbf{r}, t) \quad , \quad (3.27)$$

which, after Eq. (2.15), Eq. (3.9) and Eq. (3.10), result in

$$\mathbf{E}_{\text{comb}}(\mathbf{r}, t) = \frac{1}{2} [-(2T_p - 1)A_x(z, t)\hat{\mathbf{x}} + (2R_s - 1)A_y(z, t)\hat{\mathbf{y}}] \exp [i(k(\omega_0)z - \omega_0 t)] + c.c. \quad (3.28)$$

$$\mathbf{E}_{\text{loss}}(\mathbf{r}, t) = -i \left[\sqrt{(1 - T_p)T_p} A_x(z, t)\hat{\mathbf{x}} + \sqrt{(1 - R_s)R_s} A_y(z, t)\hat{\mathbf{y}} \right] \exp [i(k(\omega_0)z - \omega_0 t)] + c.c. \quad (3.29)$$

Since both pulses that are propagating through the Sagnac loop accumulate identical phases (disregarding the phase jumps due to the reflective elements), the resulting output pulse is linearly polarized under 45° (any deviation from the ideal 45° are due to the different magnitudes of the s - and p -polarization components). If now one or more fiber amplifiers are placed inside of the loop, this technique will be referred to as passive CBC [10]. In that case, the counter-propagating pulses are amplified, whereas one fiber amplifier can be considered as two of the afore mentioned single laser units, acting as two channels. In such a setup it is important to consider symmetry properties. As an example, in Fig. 3.5a one fiber amplifier is introduced in an asymmetric manner, since the counter-clockwise-propagating pulse enters the fiber first because of the shorter path length between the PBS and the fiber facet. This may result in different amplification dynamics for the counter-propagating pulses. Consequently, it seems to be advantageous to employ a symmetric loop, which would lead to the two pulses entering the fiber facets at the same time. For a simplified representation of a gain element inside of the loop, Eq. (3.24) and Eq. (3.25) change to

$$\mathbf{E}_1(\mathbf{r}, t) = \sqrt{G} \mathbf{J}_M^3 \mathbf{J}_T \mathbf{E}(\mathbf{r}, t) \quad (3.30)$$

$$\mathbf{E}_2(\mathbf{r}, t) = \sqrt{G} \mathbf{J}_M^3 \mathbf{J}_R \mathbf{E}(\mathbf{r}, t) \quad , \quad (3.31)$$

whereby identical amplification of the counter-propagating pulses is assumed. Since \sqrt{G} is just a constant factor, its position with respect to \mathbf{J}_M is not relevant. Using Eq. (3.26) and Eq. (3.27) as well as considering a 45° linearly polarized input pulse, the combined output power and the lost power are

$$P_{\text{out}}(z, t) = 2CG \left[T_p(T_p - 1) + R_s(R_s - 1) + \frac{1}{2} \right] |A(z, t)|^2 \quad (3.32)$$

$$P_{\text{loss}}(z, t) = 2CG [T_p(1 - T_p) + R_s(1 - R_s)] |A(z, t)|^2 \quad . \quad (3.33)$$

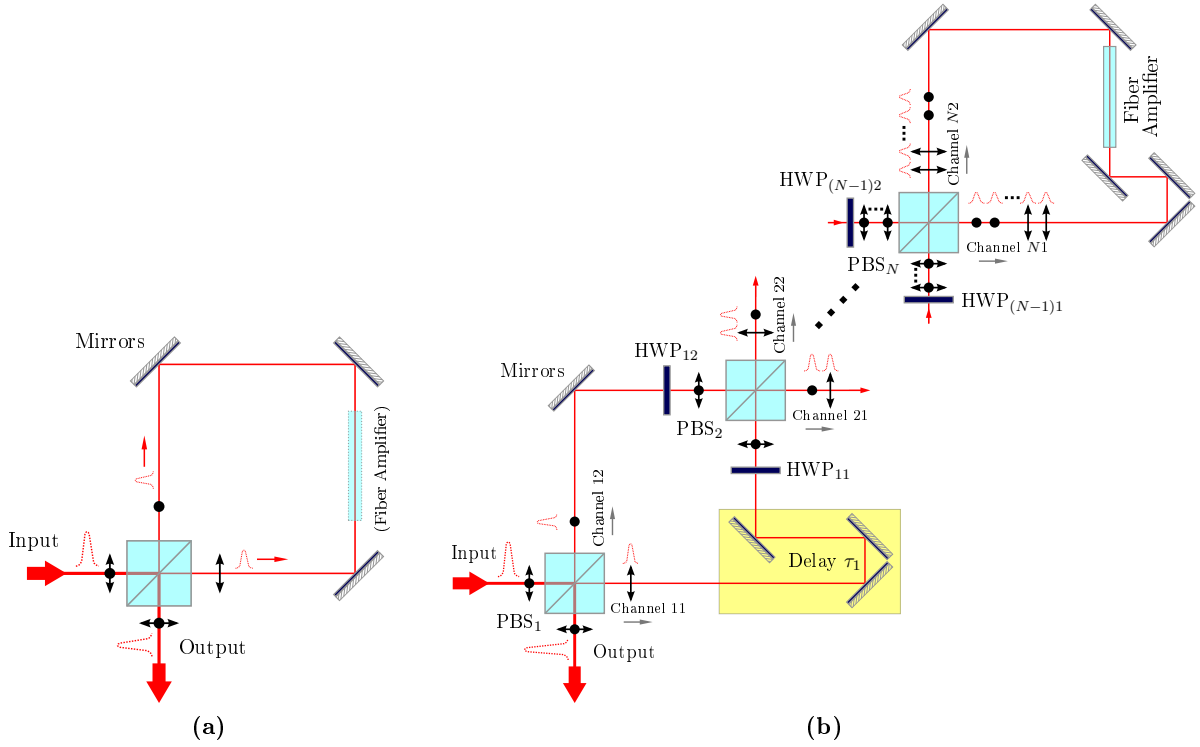


Fig. 3.5: Schematic representation of (a) a Sagnac interferometer and a fiber amplifier, and (b) the passive CBC setup using the Sagnac interferometer and Mach-Zehnder type interferometric temporal division units.

Again, the loss is mainly determined by T_p (and R_s). Using Eq. (2.17), the orientation angle of the linearly polarized output in the ideal case of identical amplification of the counter-propagating pulses is

$$\tan(2\psi) = \frac{|(2R_s - 1)(2T_p - 1)|}{2[T_p(T_p - 1) - R_s(R_s - 1)]} . \quad (3.34)$$

Consequently, the quality of a PBS determines the loss of the system and the further usefulness of the combined output. The use of such a Sagnac interferometer allows reducing the peak power of the pulses during the amplification by a factor of two, which decreases the impact of nonlinear effects and results in higher achievable amplification. However, this passive CBC scheme is limited to just two simultaneous channels.

To further increase the number of channels and to further decrease the peak power during amplification, this implementation can be extended with the idea of DPA (which will be referred to as passive DPA). Now, the pulses are not only divided spatially but also temporally. Therefore, Mach-Zehnder type interferometric spatial and temporal division units are placed in front of the Sagnac interferometer. Fig. 3.5b shows the schematic setup. A 45° linearly polarized input pulse is spatially split by a PBS, which means that the p -component is transmitted and the s -component is reflected. No amplifiers are placed inside of the channels and the pulses propagate in free space. As notation the first and the second channels are numbered 11 and 12, respectively, where the first number represents the number of the Mach-Zehnder type interferometer. Additionally, one channel (11) is extended by a simple two mirror delay line, which produces

a temporal delay of τ_1 for one of those pulses. With this simple scheme, time delays in the nanosecond range are possible. Furthermore, a HWP is placed in each channel in front of the subsequent PBS with an angle of the optical axes of $\theta = 22.5^\circ$ with respect to the s -polarization component. Consequently, the orientation angles of the two orthogonally polarized pulses are rotated by 2θ , which results in $\psi = \psi_0 + 45^\circ$ (i.e. 45° for the previously p -polarized (0°) pulse and 135° for the previously s -polarized (90°) pulse). Subsequently, they are again spatially divided at the second PBS. Since both pulses arrive at different times they are divided separately producing two orthogonally polarized pulses for each channel. Those channels are now named channel 21 and channel 22. Due to the shorter optical path of channel 12, the first pulse in channel 21 is p -polarized and in channel 22 s -polarized. Additionally, each subsequent pulse in each channel is orthogonally polarized and it possesses a delay of τ_1 with respect to the previous one. As indicated in Fig. 3.5b, such Mach-Zehnder type interferometric units may be cascaded several times. However, the delay line for each unit must be twice as long as that of the previous one, which can be referred to the first delay as $\tau_m = 2^{m-1}\tau_1$. For N PBSs this results in $N - 1$ Mach-Zehnder type interferometric units and in a total number of 2^N pulses. To express this mathematically, a Jones matrix for the temporal delay must be defined. For a temporal delay τ_m , this can be written as

$$\mathbf{J}_D(\tau_m) = \begin{pmatrix} \delta(t - \tau_m)* & 0 \\ 0 & \delta(t - \tau_m)* \end{pmatrix}, \quad (3.35)$$

where the convolution ($*$) with the delta function (δ) represents a phase shift corresponding to a temporal delay. Rewriting Eq. (3.24) and Eq. (3.25), according to Fig. 3.5b, the fields in channel 11 and 12 in front of the second PBS are

$$\mathbf{E}_{11}(\mathbf{r}, t) = \mathbf{J}_{\text{HWP}}(\theta_{11})\mathbf{J}_D(\tau_1)\mathbf{J}_M^3\mathbf{J}_T\mathbf{E}(\mathbf{r}, t) \quad (3.36)$$

$$\mathbf{E}_{12}(\mathbf{r}, t) = \mathbf{J}_{\text{HWP}}(\theta_{12})\mathbf{J}_M\mathbf{J}_R\mathbf{E}(\mathbf{r}, t), \quad (3.37)$$

where the order of the mirror and delay matrices is not important, since both represent just constant factors. The fields in the subsequent Mach-Zehnder type interferometers are then

$$\mathbf{E}_{21}(\mathbf{r}, t) = \mathbf{J}_{\text{HWP}}(\theta_{21})\mathbf{J}_D(\tau_2)\mathbf{J}_M^3[\mathbf{J}_R\mathbf{E}_{11}(\mathbf{r}, t) + \mathbf{J}_T\mathbf{E}_{12}(\mathbf{r}, t)] \quad (3.38)$$

$$\mathbf{E}_{22}(\mathbf{r}, t) = \mathbf{J}_{\text{HWP}}(\theta_{22})\mathbf{J}_M[\mathbf{J}_T\mathbf{E}_{11}(\mathbf{r}, t) + \mathbf{J}_R\mathbf{E}_{12}(\mathbf{r}, t)], \quad (3.39)$$

which can be carried on to

$$\mathbf{E}_{(m+1)1}(\mathbf{r}, t) = \mathbf{J}_{\text{HWP}}(\theta_{(m+1)1})\mathbf{J}_D(\tau_{(m+1)})\mathbf{J}_M^3[\mathbf{J}_R\mathbf{E}_{m1}(\mathbf{r}, t) + \mathbf{J}_T\mathbf{E}_{m2}(\mathbf{r}, t)] \quad (3.40)$$

$$\mathbf{E}_{(m+1)2}(\mathbf{r}, t) = \mathbf{J}_{\text{HWP}}(\theta_{(m+1)2})\mathbf{J}_M[\mathbf{J}_T\mathbf{E}_{m1}(\mathbf{r}, t) + \mathbf{J}_R\mathbf{E}_{m2}(\mathbf{r}, t)], \quad (3.41)$$

with $m = 1, 2, \dots, N$, whereby both $\mathbf{E}_{N1}(\mathbf{r}, t)$ and $\mathbf{E}_{N2}(\mathbf{r}, t)$, respectively, contain then 2^{N-1} pulses. As an example, the fields entering the Sagnac loop for the case of a setup containing two PBSs are calculated. Considering a 45° linearly polarized input pulse (fully polarized), as given by Eq. (3.16), and the angles of the HWPs in the two channels of the Mach-Zehnder type

interferometer of $\theta_{11} = \theta_{12} = 22.5^\circ$ as well as writing for $\mathbf{J}_D(\tau_1)\mathbf{E}(\mathbf{r}, t) = \mathbf{E}(\mathbf{r}, t - \tau_1)$, the complex fields after the second PBS, using Eq. (2.19), Eq. (3.9) and Eq. (3.10), are

$$\mathbf{E}_{21}(\mathbf{r}, t) = \frac{i}{2} \begin{pmatrix} -\sqrt{R_s T_p} - \sqrt{T_p(1-T_p)} \\ \sqrt{1-R_s}(\sqrt{R_s} - \sqrt{1-T_p}) \end{pmatrix} E(z, t) - \frac{i}{2} \begin{pmatrix} \sqrt{1-T_p}(\sqrt{T_p} + \sqrt{1-R_s}) \\ \sqrt{R_s T_p} - \sqrt{R_s(1-R_s)} \end{pmatrix} E(z, t - \tau_1) \quad (3.42)$$

$$\mathbf{E}_{22}(\mathbf{r}, t) = \frac{1}{2} \begin{pmatrix} \sqrt{R_s(1-T_p)} + 1 - T_p \\ \sqrt{R_s(1-T_p)} - R_s \end{pmatrix} E(z, t) - \frac{1}{2} \begin{pmatrix} \sqrt{T_p(1-R_s)} + T_p \\ \sqrt{T_p(1-R_s)} + R_s - 1 \end{pmatrix} E(z, t - \tau_1), \quad (3.43)$$

where $E(z, t) = A(z, t) \exp[i(k(\omega_0)z - \omega_0 t)]$ (electric field with the amplitude function of a pulse). Each term of Eq. (3.42) and Eq. (3.43) represents one of the four separated pulses. The individual field components are now expressed by the detailed matrix notation (the first and the second row imply $\hat{\mathbf{x}}$ und $\hat{\mathbf{y}}$, respectively). This was done to show the change of each individual field component. To illustrate the main polarization orientation of the delayed pulses, as shown in Fig. 3.5b, all terms including the factors $(1 - T_p)$ and $(1 - R_s)$, which are small, were colored in blue. Those blue terms affect the orientation of the linear polarization states, which will lead to the losses of the setup. In Fig. 3.6 the influence of the quality of the PBSs is shown according to Eq. (3.42) and Eq. (3.43) for both the ideal case with $T_p = 100\%$ and $R_s = 100\%$, and the more realistic case with $T_p = 95\%$ and $R_s = 99\%$, for a 45° linearly polarized input pulse with a pulse duration of $\Delta t = 2$ ns, HWPs orientation of $\theta = 22.5^\circ$, and a delay of $\tau_1 = 7$ ns. This will be further considered in Chapter 4.

Next, the pulses counter-propagate through the Sagnac loop and are amplified in one fiber amplifier. Again, a simplified representation is used. As depicted in Fig. 3.5b, an individual delay line is introduced in the Sagnac loop to provide the possibility of placing the fiber amplifier in the middle of the loop. Marking the back-propagating fields with a dash, the fields in the respective channels after a further pass through the second PBS are

$$\mathbf{E}'_{11}(\mathbf{r}, t) = \mathbf{J}_T \sqrt{G} \mathbf{J}_M^5 \mathbf{E}_{21}(\mathbf{r}, t) + \mathbf{J}_R \sqrt{G} \mathbf{J}_M^5 \mathbf{E}_{22}(\mathbf{r}, t) \quad (3.44)$$

$$\mathbf{E}'_{12}(\mathbf{r}, t) = \mathbf{J}_R \sqrt{G} \mathbf{J}_M^5 \mathbf{E}_{21}(\mathbf{r}, t) + \mathbf{J}_T \sqrt{G} \mathbf{J}_M^5 \mathbf{E}_{22}(\mathbf{r}, t) \quad (3.45)$$

As can be seen, in principle, disregarding the factors \sqrt{G} and the matrices \mathbf{J}_M , in Eq. (3.44) the complete first row of Eq. (3.42) and the second row of Eq. (3.43) are combined as well as in Eq. (3.45) the second row of Eq. (3.42) and the first row of Eq. (3.43), building two back-propagating pulses in the respective channels with some small delayed loss pulses. The pulse traveling back through the channel 11 consists mainly of the first pulses of Eq. (3.42) and Eq. (3.43), which now also accumulates some time delay and arrives at the same time at the first PBS as the pulse traveling back through the channel 12, which consists mainly of the second pulses of Eq. (3.42) and Eq. (3.43). Since the optical axes of the HWPs are oriented with an angle of θ with respect to the forward-propagating field, the backward-propagating field will see an angle of $-\theta$. Consequently, the combined orthogonal linearly polarized beams produce ideally a pulse with a linear polarization orientation of $\psi = 45^\circ$ or $\psi = 135^\circ$, respectively. These are subsequently rotated with a HWP to either *s*- or *p*-polarization in each channel. Those two

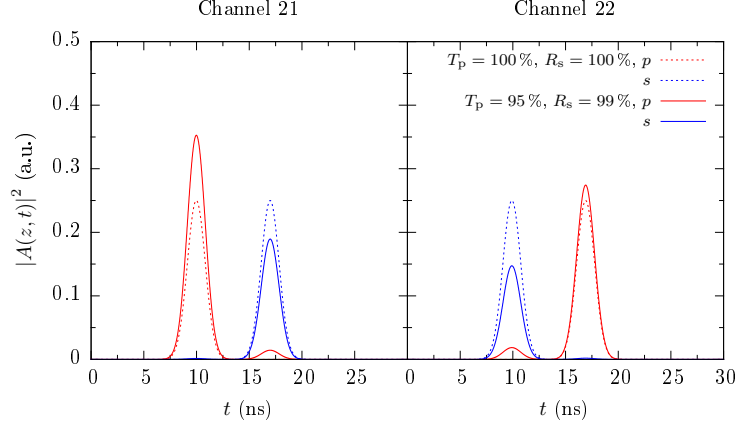


Fig. 3.6: Simulation of the pulse division by two PBSs (HWPs orientation of $\theta = 22.5^\circ$) for a 45° linearly polarized input pulse with normalized amplitude (both polarization components possess an amplitude of 0.5). The polarization components in channel 21 and 22 are depicted for $T_p = 100\%$ and $R_s = 100\%$ in dashed lines and for $T_p = 95\%$ and $R_s = 99\%$ in solid lines, where the p - and s -polarization are colored in red and blue, respectively.

states combine again at a subsequent PBS and so on. Finally, the combined output and the loss, which travels back to the input port, is given by

$$\mathbf{E}_{\text{comb}}(\mathbf{r}, t) = \mathbf{J}_R \mathbf{J}_D(\tau_1) \mathbf{J}_M^3 \mathbf{J}_{\text{HWP}}(-\theta_{11}) \mathbf{E}'_{11}(\mathbf{r}, t) + \mathbf{J}_T \mathbf{J}_M \mathbf{J}_{\text{HWP}}(-\theta_{12}) \mathbf{E}'_{12}(\mathbf{r}, t) \quad (3.46)$$

$$\mathbf{E}_{\text{loss}}(\mathbf{r}, t) = \mathbf{J}_T \mathbf{J}_D(\tau_1) \mathbf{J}_M^3 \mathbf{J}_{\text{HWP}}(-\theta_{11}) \mathbf{E}'_{11}(\mathbf{r}, t) + \mathbf{J}_R \mathbf{J}_M \mathbf{J}_{\text{HWP}}(-\theta_{12}) \mathbf{E}'_{12}(\mathbf{r}, t) \quad (3.47)$$

An analytical expression of this is too comprehensive and it is, therefore, omitted at this point. For a certain number of Mach-Zehnder type interferometers, the back propagation (beginning after the last PBS) can be written as

$$\begin{aligned} \mathbf{E}'_{m1}(\mathbf{r}, t) = \mathbf{J}_R \mathbf{J}_D(\tau_{(m+1)}) \mathbf{J}_M^3 \mathbf{J}_{\text{HWP}}(-\theta_{(m+1)1}) \mathbf{E}'_{(m+1)1}(\mathbf{r}, t) + \\ \mathbf{J}_T \mathbf{J}_M \mathbf{J}_{\text{HWP}}(-\theta_{(m+1)2}) \mathbf{E}'_{(m+1)2}(\mathbf{r}, t) \end{aligned} \quad (3.48)$$

for channel $m1$ and for channel $m2$

$$\begin{aligned} \mathbf{E}'_{m2}(\mathbf{r}, t) = \mathbf{J}_T \mathbf{J}_D(\tau_{(m+1)}) \mathbf{J}_M^3 \mathbf{J}_{\text{HWP}}(-\theta_{(m+1)1}) \mathbf{E}'_{(m+1)1}(\mathbf{r}, t) + \\ \mathbf{J}_R \mathbf{J}_M \mathbf{J}_{\text{HWP}}(-\theta_{(m+1)2}) \mathbf{E}'_{(m+1)2}(\mathbf{r}, t) \quad , \end{aligned} \quad (3.49)$$

with $m = N - 1, \dots, 2, 1$.

Furthermore, it could be of interest to provide pulses with the same power in the channels. For this the power division will be adjusted with the help of the HWP in front of the PBS and by measuring the powers of the channels. Considering an initial linearly p -polarized input pulse incident on a combination of a HWP and a (lossless) PBS, the fields in the two channels are

given by

$$\mathbf{E}_1(\mathbf{r}, t) = \mathbf{J}_T \mathbf{J}_{\text{HWP}}(\theta) E(z, t) \hat{\mathbf{x}} \quad (3.50)$$

$$\mathbf{E}_2(\mathbf{r}, t) = \mathbf{J}_R \mathbf{J}_{\text{HWP}}(\theta) E(z, t) \hat{\mathbf{x}} \quad , \quad (3.51)$$

where again $E(z, t) = A(z, t) \exp [i(k(\omega_0)z - \omega_0 t)]$. Using Eq. (2.19), Eq. (3.9) and Eq. (2.17), as a result, for the condition $|\mathbf{E}_1(\mathbf{r}, t)|^2 \stackrel{!}{=} |\mathbf{E}_2(\mathbf{r}, t)|^2$ a solution is found to be

$$\tan(2\theta) = \pm \sqrt{\frac{2T_p - 1}{2R_s - 1}} \quad . \quad (3.52)$$

For example, the realistic values of transmissivity and reflectivity of a PBS of $T_p > 95\%$ and $R_s > 99\%$, would lead to an orientation angle for the HWP with respect to the s -polarization component of $\theta \approx 21.9^\circ$. Consequently, the amount of the larger reflected part is somewhat reduced to increase the amount of the transmitted part.

All the above presented calculations were made without considering, for example, influences of mirrors or other losses. They form the fundamental base for the simulations of the experimental setups and they were implemented in MATLAB[®]. In the following chapter, the experimental investigations and simulations will be presented.

4 Experimental and Theoretical Investigation of the Passive DPA Setup

In this chapter the experimental realization and investigation of the above explained passive CBC setup incorporating the idea of DPA will be presented. This was investigated both for a setup including a passive fiber and for one including an active fiber. The former was used for proof-of-principle experiments, which will be discussed first. Afterwards, the setup was adapted for high-power experiments. This way, a CPA system in a MOPA architecture was used and an active fiber was included into the setup. Both the extraction of high average power and high pulse energy, respectively, will be presented. Furthermore, based on some theoretical considerations, these experimental results will be compared with simulations.

4.1 Setup Including a Passive Fiber

4.1.1 Experimental Setup

The experimental setup is depicted in Fig. 4.1. This was used for the demonstration of the idea in a proof-of-principle experiment. As a laser source an ytterbium-based master oscillator from the company HighQLaser (of the type *femtoTrain*TM) was used. It delivered an average output power of $\bar{P} \approx 200$ mW at a central wavelength of $\lambda_0 = 1028.3$ nm with a bandwidth of $\Delta\lambda = 3.9$ nm. Furthermore, it produced linearly polarized pulses with a pulse duration of $\Delta t = (200 \pm 100)$ fs [46] (not measured) with a repetition rate of $f_{\text{rep}} = 40$ MHz, that corresponds to a pulse interval of $1/f_{\text{rep}} = 25$ ns. To protect the oscillator from back-propagating beams, an optical Faraday isolator from the company Soliton was used. After the isolator the pulses were *s*-polarized. This can be important, since the reflection of any polarization orientation different from *s*- or *p*-polarization may lead to depolarization effects at the mirrors. Due to the isolator the average power was reduced to $\bar{P} \approx 160$ mW, which is referred to in the following as the input power of the setup. The beam was collimated with the help of a Kepler telescope consisting of two equal standard lenses with a focal length of $f = 8$ mm, with which a beam diameter of $2w_0 \approx 2$ mm was obtained. This corresponds to a Rayleigh length of $z_R = \pi w_0^2/\lambda_0 \approx 3$ m, which was sufficient for a propagation from the telescope to the fiber end facet. Throughout the whole setup, dielectric mirrors from the company Thorlabs of the kind E03 were used. Before the beam enters the first PBS, the orientation of the linear polarization state was adjusted by the HWP₀; all HWPs were from the company ALTECHNA for a design wavelength of 1030 nm. With the orientation angle

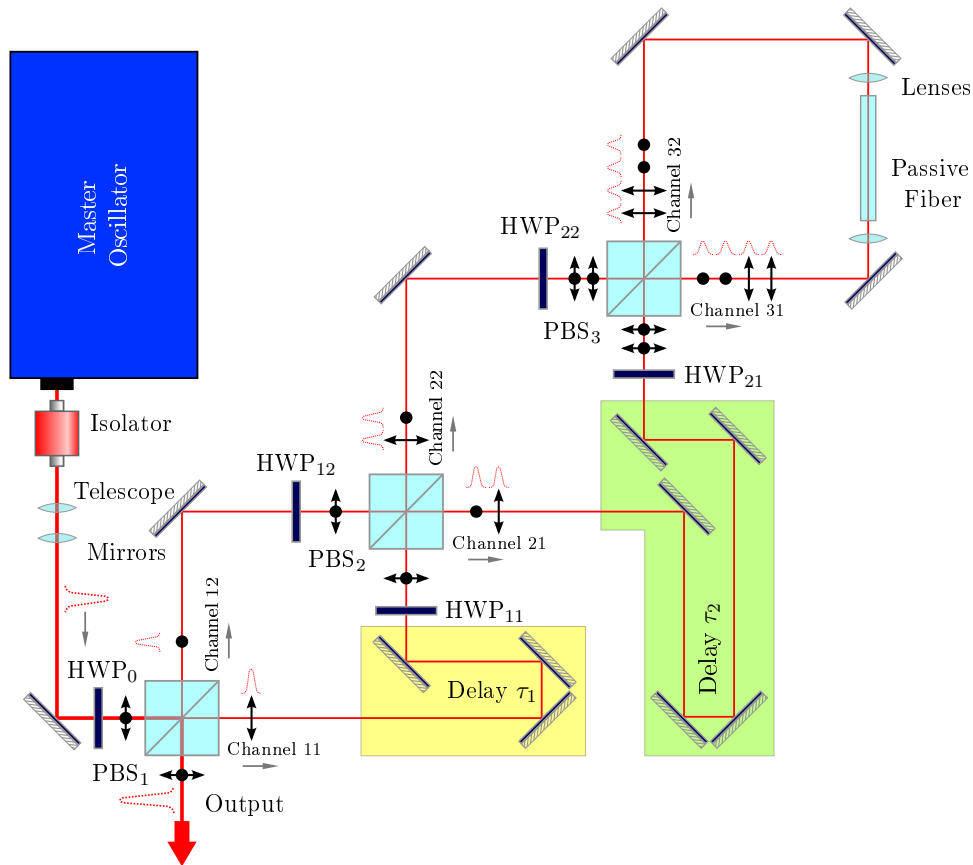


Fig. 4.1: Scheme of the experimental passive DPA setup consisting of three PBSs, which form part of two Mach-Zehnder type interferometric temporal division units, and including a passive fiber.

of the optical axis of the HWPs, the splitting ratio of the input could be changed. As PBSs, cubes from the company Edmund Optics were used, which were specified to exhibit $R_s > 99\%$ and $T_p > 90\%$ with a loss at each surface of $\eta < 0.5\%$ due to the anti-reflection coatings [47]. To achieve an overall division of one input pulse into eight pulses in this basic experiment, three PBSs were used, which formed two Mach-Zehnder type interferometric units. As explained in Section 3.3, a HWP was placed in each channel to rotate the orientation of the orthogonal linearly polarized pulses by 45° so that they could be further divided at the subsequent PBS. One channel of each Mach-Zehnder type interferometer included a delay line. The first one had a path length of $l_{\tau_1} \approx 72$ cm, which corresponds to a temporal delay of $\tau_1 = l_{\tau_1}/c = 2.4$ ns. Actually, the second delay line should have twice as large as the first one. This had a path length of $l_{\tau_2} \approx 149$ cm, which corresponds to a temporal delay of $\tau_2 = l_{\tau_2}/c = 4.8$ ns. Since the pulse durations were in the femtosecond range, this was not critical in terms of temporal overlaps. Consequently, four pulses entered each channel of the Sagnac loop. To simulate a fiber amplifier, a standard passive single-mode fiber was placed inside the loop. This fiber was from the company j-fiber (IG-09/125/250) which possessed a core diameter of $6 \mu\text{m}$, that corresponds to a mode-field diameter of approximately $7 \mu\text{m}$, and a length of $L \approx 10$ cm. As shown in Fig. 4.1, for this passive and low power case no symmetry properties were considered, but they will play a significant role for a fiber amplifier. In order to focus the beams into the fiber and in order to

collimate the emitted beams, two spherical lenses with a focal length of $f = 18.4$ mm were used. This setup was used in a proof-of-principle experiment. To investigate the advantage of the division of the input pulse, which leads to a reduction of the peak power inside of the fiber, the occurrence of SPM, in the form of spectral broadening, was measured. This will be presented in the following.

4.1.2 Experimental Investigations

With the above described proof-of-principle setup, the temporal and spatial division and recombination of ultrashort pulses were investigated. To demonstrate its feasibility and the advantage of the reduction of the peak power of the pulses, a passive fiber was introduced into the Sagnac loop. Since the spectrum of an ultrashort pulse with significant peak power may be broadened due to SPM, a divided series of pulses should undergo significantly less broadening. Consequently, this effect was used to compare the impact of nonlinear effects for both one pulse and for eight pulses.

To select the desired number of pulses, the rotation angles of the HWPs were used. First, all of them were adjusted so that the measured powers in both subsequent channels after the respective PBS were nearly the same. To adjust the division of the power for the channels 21 and 22 the channels 11 and 12 were alternately blocked. However, it should be mentioned that although the powers in the channels directly after PBS₁ were the same, the input powers arriving at PBS₂ were slightly different. This is due to the fact that the channels including a delay line contained more mirrors than the others and that the mirrors possessed losses, which may be polarization-dependent. According to [48], the E03 mirrors are specified with the reflectivities $R_p \approx 99.0\%$ and $R_s \approx 99.5\%$. Considering a p -component traveling through the delay lines, for example, the mirrors lead to a reduced power of approximately $R_p^3 \approx 97\%$ in the first one and $R_p^5 \approx 95\%$ in the second one. However, that the powers are equal in two channels does not mean that in the polarization components are weighted equally. As a result, those contents in the wrong polarization component led to a polarization angle different from $\psi = 45^\circ$ after the next HWP, which would have caused a further change in the splitting ratio of the subsequent PBS. Consequently, in order to equalize the powers in the next channels, the orientation of the next HWP must be moved away further from $\theta = 22.5^\circ$. This influenced the polarization states of the back-propagating pulses and, finally, the combined output power and the losses, respectively. In any case, all HWPs were oriented such that the power was divided equally by the subsequent PBS. With the help of a high-resolution oscilloscope (LeCroy), since the real pulse shape and pulse duration were not important for this experiment, the divided pulses were measured after PBS₃ in channel 31 and 32, as shown in Fig. 4.2a and Fig. 4.2b. In total, eight pulses were obtained by using three PBS. For comparison, the corresponding input pulses from the oscillator are shown in Fig. 4.2c. As can be seen, the peaks of the divided pulses had all different magnitudes due to the sum of the influences of the PBSs, HWPs and mirrors. The average input power of the setup (in front of PBS₁) was $\bar{P}_{in} = 160$ mW which resulted, due to the mirror losses,

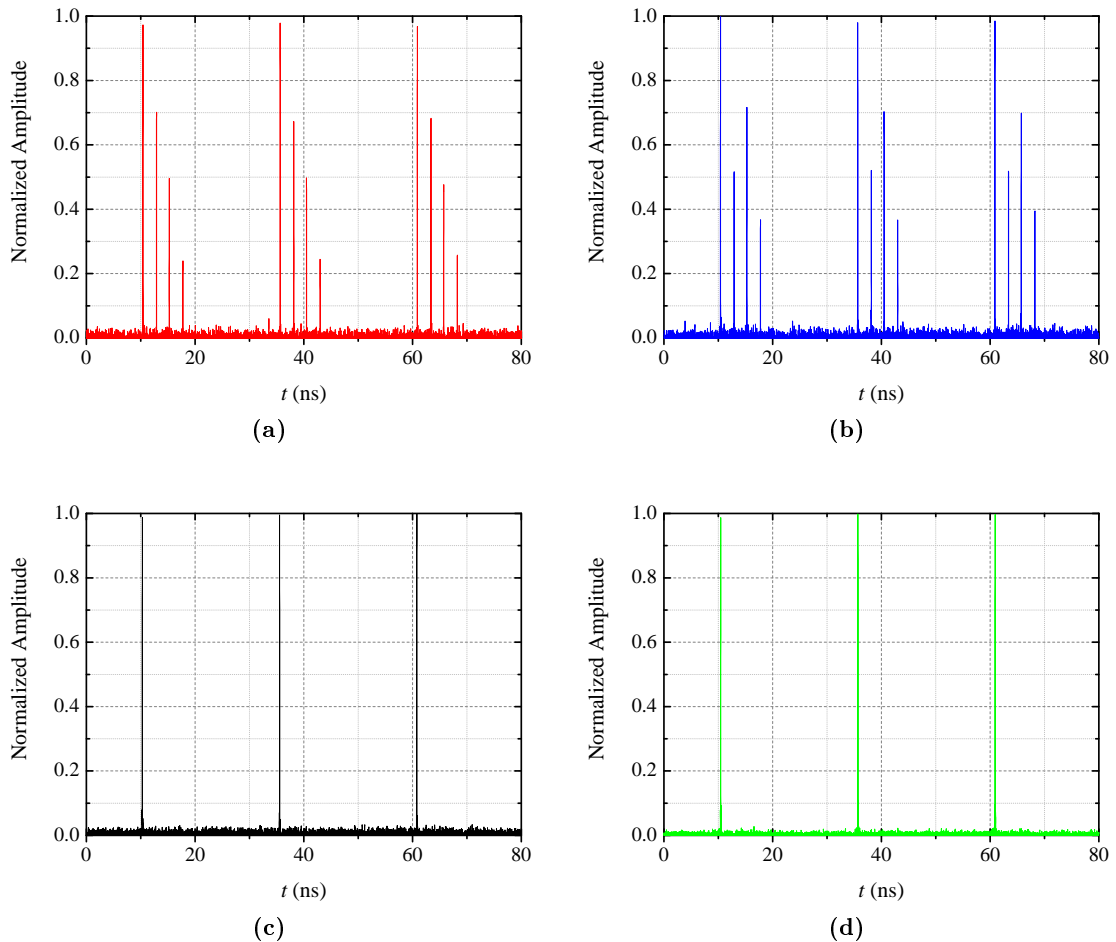
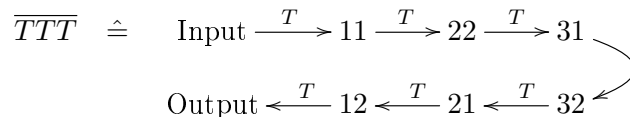


Fig. 4.2: Measured (normalized) pulses (a) in channel 31 and (b) in channel 32 (for equally divided powers at each PBS). For comparison, in (c) the input pulses of the oscillator and in (d) the combined output pulses are shown.

in $\bar{P} = 75$ mW for channel 31 and $\bar{P} = 78$ mW for channel 32 inside the Sagnac loop in front of the passive fiber. Finally, a combined average output power of $\bar{P}_{\text{comb}} = 55$ mW was achieved, for which the combined pulses are shown in Fig. 4.2d. Within the resolution of the oscilloscope no noticeable side pulses were visible. Measuring the polarization efficiency according to Eq. (3.21) with the help of another polarization cube at the output resulted in $\eta_{\text{LP}} = 77\%$ (DOLP = 55% after Eq. (3.20)). Consequently, the recombination was not perfect. Reasons for that were, for example, an insufficient Rayleigh length and additional phase shifts accumulated due to the mirrors. The former is important for the beam size throughout the setup, since there are a shortest and a longest path. If the sizes of the beams traveling through those are different, something that was observable, the spatial combination efficiency is reduced. On the other hand, the different polarization states of the pulses may accumulate a phase difference due to the mirrors, which reduces the temporal combination efficiency.

To obtain an estimation of for the combining efficiency, the combined output power of eight pulses must be related to that of one single pulse. Actually, removing the division setup and using just the fiber would be the fairest comparison of a combined and a single beam. This is

because a single beam propagating through the division setup includes also all system losses. Consequently, the apparent combining efficiency will be higher, which should be kept in mind. However, it would have been impractical to remove all division components for such a measurement. Therefore, a single beam was chosen by rotating the HWPs. Since, in principle, the divided pulses can be considered as individual beams, there were eight possibilities for single pulse paths. Those depended on whether a pulse was completely transmitted or reflected by a PBS. To distinguish between them the short notation $\overline{\text{PBS}_1\text{PBS}_2\text{PBS}_3}$ is introduced, where, for example, \overline{TTT} denotes the path of transmission at each PBS. This can be illustrated as



with the numbers denoting the channels according to Fig. 4.1. With this, for example, the average output power for one pulse traveling the path \overline{TTT} was $\bar{P} = 60 \text{ mW}$ while for the path \overline{RRR} it was $\bar{P} = 72 \text{ mW}$. The main reason for the strong reduction of the power was the relatively poor fiber coupling efficiencies. Since this was just a proof-of-principle experiment, the fiber ends were just cleaved and clamped in a magnet holder. The coupling efficiencies for all eight possible beams are summarized in Tab. 4.1, which were determined by the ratio of the measured powers before and after the fiber. Hence, the main loss of power was due to the poor fiber coupling efficiency (approximately 50%). As the power values before the fiber indicate, there were different system losses for the different paths. Since a combined beam contains all individual beams, the system losses together with the poor fiber coupling efficiencies of each beam were the main reason for the reduced combined output power. Consequently, it is convenient to define the combining efficiency as

$$\eta_{\text{comb}} = \frac{\bar{P}_{\text{comb}}}{\frac{1}{N} \sum_{m=1}^N \bar{P}_m} \quad , \quad (4.1)$$

where N is the total number of possible beam paths (in this case $N = 8$) with the corresponding power \bar{P}_m of each, according to Tab. 4.1. In other words, the combining efficiency is defined by the relation of the combined output power and the average of the single pulse powers of all possible beam paths going through the setup. Unfortunately, just the single pulse powers for the case of \overline{TTT} and \overline{RRR} were measured. Averaging those and using the combined output power given above, a combining efficiency of $\eta_{\text{comb}} = 83 \%$ was achieved. Finally, by using the already given polarization efficiency, this results, according to Eq. (3.22), in a total system efficiency of $\eta_{\text{tot}} = 64 \%$. Even though not outstanding, this result shows the feasibility of this approach.

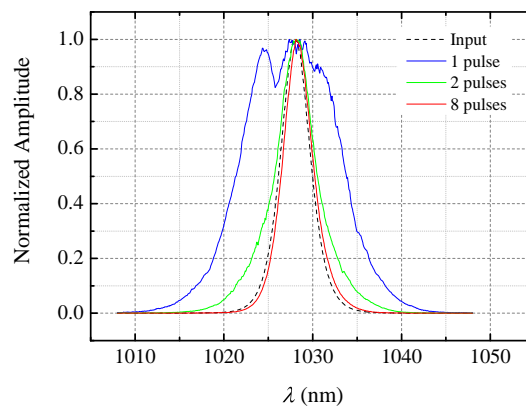
Furthermore, the output spectra were measured. Since the peak power of an ultrashort pulse can be significant, SPM may lead to spectral broadening after propagating through the passive fiber. A small core diameter of the fiber was chosen to enhance this effect, according to Eq. (2.34). The influence of XPM can be neglected, since the interaction length of the counter-propagating pulses is very short. Estimating the peak power of one pulse by using $\bar{P} = 150 \text{ mW}$ and assuming $\Delta t = 250 \text{ fs}$ as well as applying Eq. (2.12) and Eq. (2.13), it results $\hat{P} \approx 15 \text{ kW}$. Due to the division of one pulse into eight, the peak power of each is reduced by a factor of eight, which

Tab. 4.1: Measured fiber coupling efficiencies for the different beam paths.

Nr.	PBS ₁	PBS ₂	PBS ₃	\bar{P} (mW) before fiber	\bar{P} (mW) after fiber	η_{couple} (%)
1	<i>T</i>	<i>T</i>	<i>T</i>	140	72	51
2	<i>T</i>	<i>R</i>	<i>R</i>	145	66	46
3	<i>T</i>	<i>T</i>	<i>R</i>	150	62	41
4	<i>T</i>	<i>R</i>	<i>T</i>	150	52	35
5	<i>R</i>	<i>R</i>	<i>R</i>	150	77	51
6	<i>R</i>	<i>T</i>	<i>T</i>	145	78	54
7	<i>R</i>	<i>R</i>	<i>T</i>	150	68	45
8	<i>R</i>	<i>T</i>	<i>R</i>	160	86	54

results in $\hat{P} \approx 1.9$ kW. Consequently, the output spectra should differ significantly, which can be seen in Fig. 4.3. In the case of one single pulse at the chosen path \overline{RRR} , the input spectrum of the oscillator ($\Delta\lambda = 3.9$ nm, black dashed line) was broadened to $\Delta\lambda = 12.4$ nm (blue solid line), which shows a strong influence of SPM. In contrast, for a division into eight pulses (red solid line) no significant change in the spectrum was observable. Actually, this is not a fair comparison, since the average output powers for the single pulse case and for the division into eight pulses differ by approximately 24%. However, the difference in the spectral broadening cannot be explained alone by this change of the average power. The main reason for the broader spectrum in the single pulse case is the nearly eight times higher peak power, which proves the advantage of the dividing procedure. Additionally, a division into two pulses was performed, which corresponds to the use of just a Sagnac loop without the Mach-Zehnder type interferometric division units (chosen path \overline{RR} for the first two PBSs). With this the spectrum (green solid line) was less affected compared to the case of one single pulse and an output power of $\bar{P} = 68$ mW was achieved.

In the following the properties of the passive DPA setup will be investigated theoretically. Thereby, the advantage in terms of the accumulated nonlinear phase and the limitations due to the setup itself will be considered in more detail.

**Fig. 4.3:** Measured output spectra for one, two and eight pulses compared to the input spectrum of the oscillator.

4.1.3 Theoretical Investigations

To obtain a deeper understanding of the experimental results, in the following this setup will be investigated theoretically. With the help of the theory explained in Section 3.3 a simulation tool was programmed in MATLAB[®] to investigate the behavior of such a setup. Therefore, the evolution of an input field through the setup, according to Fig. 4.1, was calculated, but at first without considering the passive fiber. The same parameters for the input pulse, $\bar{P}_{\text{in}} = 160 \text{ mW}$ and $f_{\text{rep}} = 40 \text{ MHz}$, and for the delay lines, $\tau_1 = 2.4 \text{ ns}$ and $\tau_2 = 4.8 \text{ ns}$, as in the experiment were chosen. To see the temporal shape of the pulses the pulse duration was increased to $\Delta t = 500 \text{ ps}$, otherwise the graphs would be comparable to Fig. 4.2. Assuming lossless mirrors and lossless PBSs with $T_p = 95\%$ and $R_s = 99\%$, Fig. 4.4 shows the s - and p -components (blue and red solid lines) of the divided pulses in channel 31 and 32, the input pulse, the combined output and the lost field, which propagates back to the input. Considering first Fig. 4.4a, the influence of the real splitting ratios of the PBSs can be seen by the different magnitudes of the pulses, which are related to an input pulse normalized to one (Fig. 4.4b). For comparison, the divided pulses for the case of ideal PBSs are depicted as well (dashed lines). The distribution of the pulse peaks, especially for channel 31, agrees with the measurements shown in Fig. 4.2. The different splitting ratio of the PBSs influences not only the magnitudes of the forward-propagating pulses but also the backward-propagating pulses and, hence, the combined output and the loss, respectively, which is shown in Fig. 4.4b. With the given parameters a combining efficiency of $\eta_{\text{comb}} = \bar{P}_{\text{out}}/\bar{P}_{\text{in}} \approx 75.2\%$ was theoretically obtained. This is of a comparable order of magnitude to the experimentally achieved combining efficiency, but this includes no losses. However, the measured efficiency was calculated after Eq. (4.1), which leads to a better efficiency value, since the system losses are more or less excluded. But this kind of calculation will be needed for the case of an active fiber. To determine the polarization efficiency a rotating

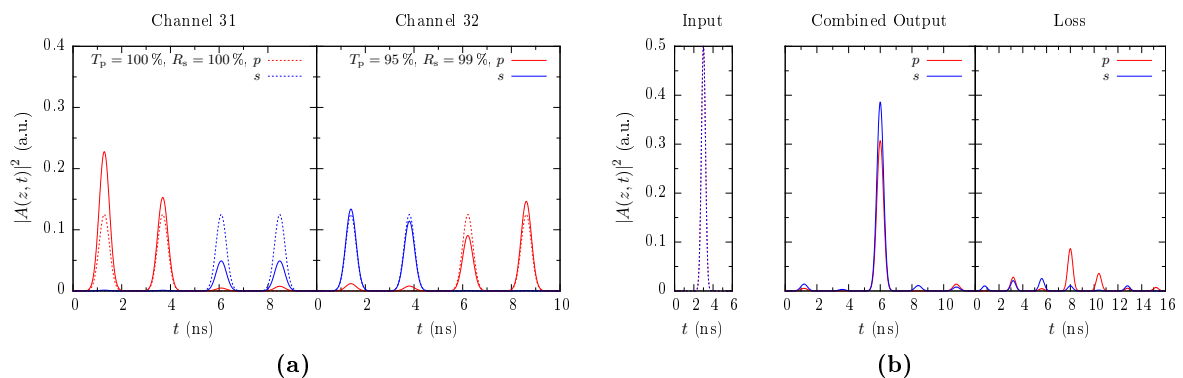


Fig. 4.4: Simulation of the field evolution through the passive DPA setup containing three PBSs (with $T_p = 95\%$, $R_s = 99\%$ and $T_p = 100\%$, $R_s = 100\%$) and no passive fiber, where (a) shows the divided pulses in channel 31 and channel 32 and (b) shows the input pulse ($\Delta t = 500 \text{ ps}$), the combined output and the loss.

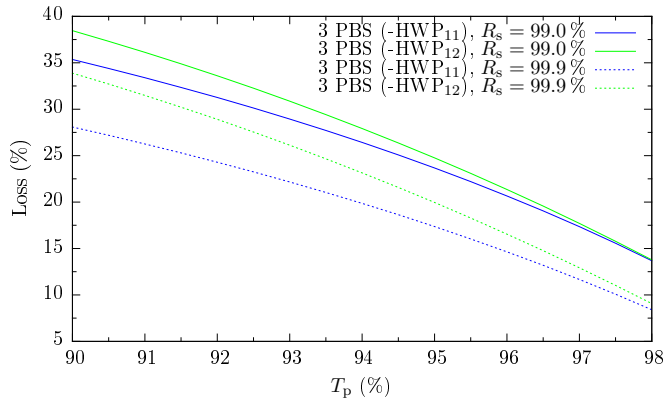


Fig. 4.5: Simulation of the loss depending on the transmissivity T_p of the PBSs for given reflectivities $R_s = 99.0\%$ (solid lines) and $R_s = 99.9\%$ (dashed lines), for the case of three PBSs (all HWPs with $\theta = 22.5^\circ$, except HWP₁₁ or HWP₁₂ that have $\theta = -22.5^\circ$).

linear polarizer after Tab. 2.1 (and Appendix B) was simulated by

$$\mathbf{E}_P(\mathbf{r}, t) = \mathbf{J}_{P_P}(\theta)\mathbf{E}_{\text{comb}}(\mathbf{r}, t) \quad (4.2)$$

which resulted after Eq. (3.21), with $P_P^{\min}(\mathbf{r}, t) = C |\mathbf{E}_P^{\min}(\mathbf{r}, t)|^2$ and $P_P^{\max}(\mathbf{r}, t) = C |\mathbf{E}_P^{\max}(\mathbf{r}, t)|^2$, and using Eq. (2.11), in a polarization efficiency of $\eta_{LP} \approx 93.6\%$ (DOLP $\approx 87.3\%$ after Eq. (3.20)). Finally, a total system efficiency, according to Eq. (3.22), of $\eta_{\text{tot}} \approx 70.5\%$ was theoretically achieved. It is noteworthy that this efficiency was just determined by the splitting ratio of the PBSs. Therefore, the influence of the parameters T_p and R_s was investigated in more detail. Fig. 4.5 shows the loss percentage $\eta_{\text{loss}} = \bar{P}_{\text{back}}/\bar{P}_{\text{in}}$ as a function of T_p for a given $R_s = 99.0\%$ (solid lines) and $R_s = 99.9\%$ (dashed lines). Thereby a setup containing three PBSs with all HWPs having a rotation angle of $\theta = 22.5^\circ$ was considered, where once HWP₁₁ and once HWP₁₂ were chosen to have the negative angle $\theta = -22.5^\circ$. As can be seen, there is a difference in the efficiency if HWP₁₁ or HWP₁₂ is chosen to have a negative angle. This is due to the asymmetric splitting ratio of the PBSs, which will lead to a larger depolarization in the reflected port because of the larger s -component and the larger leakage fraction of the p -component, in combination with the changed polarization orientation of the pulses. A subsequent combination of HWP and PBS will lead to a different division of the pulses coming from the reflected port compared to those coming from the transmitted port. Consequently, this will influence the back-propagating fields and, therefore, the recombination (which will be different for a change of the polarization orientation caused by a negative or a positive rotation angle of the respective HWP). As can be seen in Fig. 4.5, the smaller the difference of T_p and R_s is (which implies a larger T_p), the more similar are the pulses polarized after their division at a PBS and the smaller the loss. On the other hand, a larger R_s implies, for small T_p , a larger depolarization for the reflected port (since the leakage fraction of the s -component for the transmitted port becomes negligible), but an overall improved efficiency. In any case, what can be seen is that there is a loss (η_{loss}) in the range of approximately 10% to 40% (depending on the parameters) for such a setup containing three PBS, which is just caused by the splitting ratio of the PBS.

The question that now arises is if there is a possibility to improve the efficiency. The trivial answer is to use ideal PBSs. Since they are not available another possibility must be considered. The division of the pulses in the setup depends on the orientation of their linear polarization and on the splitting ratio of the PBSs. However, since the latter produces slightly different polarization orientations for the two channels, the idea is now to compensate for this with the rotation angles of the HWPs. Up to now, the rotation angles of all the HWPs were set to an absolute value of $\theta = 22.5^\circ$. Since various combinations are possible, in a first iteration the rotation angles of both HWP_{21} and HWP_{22} are fixed to $\theta = 22.5^\circ$. Furthermore, the HWP_0 at the input is fixed at this value, too. With the help of the simulation tool, again for the chosen parameters $T_p = 95\%$ and $R_s = 99\%$ as well as for $T_p = 100\%$ and $R_s = 100\%$ for comparison, all combinations were calculated and they are shown in Fig. 4.6. Fig. 4.6a shows the case of an ideal PBS whereas Fig. 4.6b shows the case of a more realistic PBS. To calculate these plots, the angle of HWP_{11} was set to the first value, which means $\theta_{\text{HWP}_{11}} = 0^\circ$, and all angles for HWP_{12} ($\theta_{\text{HWP}_{12}}$) in the range of 0° to 180° (in that case for negative angles) were calculated. This was continued for all angles of HWP_{11} , also in the range of 0° to 180° . For all these combinations the combining efficiency was calculated, which percent is color-coded in Fig. 4.6. What is obtained, is a periodic behavior along the diagonal, which reflects a change between the loss port and the output port. Ideally, both HWPs should have identical angles (or shifted by 90°) to obtain maximum output (Fig. 4.6a). Due to the asymmetric splitting ratio of the PBSs the positions of minima and maxima are shifted and they are modulated slightly along the other diagonal (Fig. 4.6b). By the selection of a maximum one has to be careful, since those in the range of multiples of 45° (ideally) correspond to rotation angles at which an incident pulse is rotated by 0° or 90° , i.e. in the case of nearly *s*- or *p*-polarized pulses that no division occurs at the subsequent PBS. Finally, choosing a maximum and doing the same calculation for the remaining HWPs in a further iteration with this procedure an improvement of the combining efficiency of

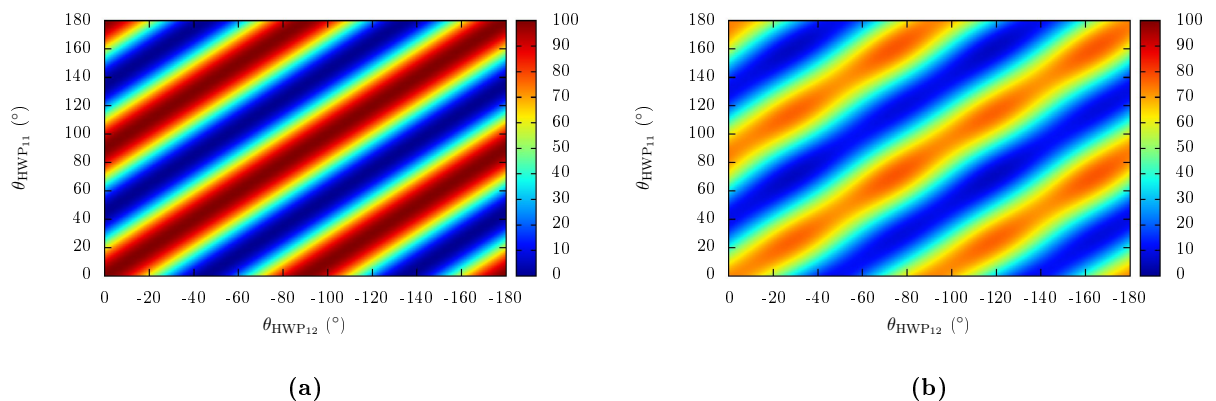


Fig. 4.6: Simulation of the combining efficiency (color-coding in percent) of the possible combinations of rotation angles in a setup containing three PBSs for HWP_{11} and HWP_{12} (angles for HWP_{12} chosen negative) for (a) $T_p = 100\%$ and $R_s = 100\%$ and (b) $T_p = 95\%$ and $R_s = 99\%$ (for all times $\theta_{\text{HWP}_0} = \theta_{\text{HWP}_{21}} = \theta_{\text{HWP}_{22}} = 22.5^\circ$).

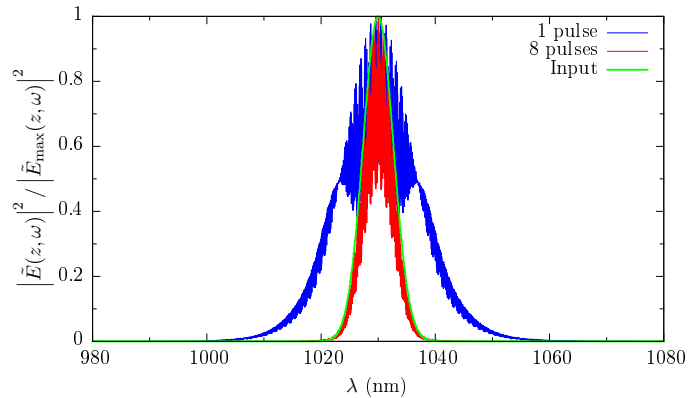


Fig. 4.7: Simulation of the influence of SPM in a passive fiber on the output spectra for both the case of one pulse and for the case of eight pulses.

just about 1% was achieved for both HWP_{11} or HWP_{12} having negative angles. Furthermore, no improvement by varying HWP_0 was observable. Consequently, the calculated losses for the chosen parameters, as shown in Fig. 4.5, are reliable.

Now a passive fiber is introduced into the Sagnac loop to consider the influence of SPM. Therefore, the Fourier Split-Step method [16] was implemented, which calculates piecewise the contributions of dispersion and SPM. The same fiber parameters were chosen as in the experiment: a length of $L = 10$ cm and a mode-field diameter of $7\ \mu\text{m}$ (fused silica with a refractive index according to Fig. 2.4a and $n_2 = 2.7 \cdot 10^{-20}\ \text{m}^2\ \text{W}^{-1}$). Furthermore, for the PBSs the parameters $T_p = 95\%$ and $R_s = 99\%$ were used as well as an input power of $\bar{P}_{\text{in}} = 160\ \text{mW}$ and an assumed pulse duration of $\Delta t = 250\ \text{fs}$ ($f_{\text{rep}} = 40\ \text{MHz}$). With the rotation angles of the HWPs two cases were simulated. In one of them all the HWPs were set to $\theta = 0^\circ$ to produce just one pulse (\overline{TTT}) and the other one all HWPs were set to $\theta = 22.5^\circ$ ($\theta_{\text{HWP}_{12}} = -22.5^\circ$) to produce a division of eight pulses. Since the peak power within the fiber of one pulse is much higher than that of the divided individual pulses, the accumulated phase due to SPM is much higher in the former case. The total accumulated phase is described by the B -integral according to Eq. (2.34). Calculating this for the case of one pulse results in the value of $B = 13\ \text{rad}$, which leads to significant distortions in the form of a broad spread spectrum. In contrast, for the case of pulse division the B -integrals of the individual pulses are in the range of $0.3\ \text{rad}$ to $1.5\ \text{rad}$, which has significant less impact compared to the previous case. The reason for the given range of B -integrals is due to the asymmetric splitting ratio of the PBSs, (see Fig. 4.4a). Since the fiber coupling efficiencies for the proof-of-principle experiment were approximately 50%, the input power is now reduced to a half. The calculated B -integrals are $3.2\ \text{rad}$ for one pulse and $0.2\ \text{rad}$ to $0.8\ \text{rad}$ for eight pulses. The corresponding output spectra for both cases are shown normalized in Fig. 4.7. As can be seen, the spectrum is broadened by SPM for one pulse while for the divided pulses the spectral width remains nearly unchanged when compared to the input spectrum. The modulations for both arises from the small leakage fractions, which are transmitted or reflected by the PBSs. These propagate differently through the setup and produce small pre- and post-pulses, which are observable in Fig. 4.4b. Compared to the experimental results, the bandwidths of the calculated spectra are in a similar range, which is mainly determined by the pulse duration. However, no

modulations were observable in the measured spectra. The reason for this is to be found on the resolution of the detector of the spectrum analyzer. Since the frequency of the modulations is too high it was not measurable during the experiments. The pre- and post-pulses have a significant impact and cause strong modulations in the spectrum even for very small magnitudes. A solution may be to use an Acousto-Optic Modulator (AOM) [18] to pick just the main intense pulse and, consequently, clean it from the parasitic pulses.

The presented considerations demonstrated the feasibility of the passive DPA approach and its advantage in terms of the total accumulated nonlinear phase. However, there are limitations, which are mainly determined by the quality of the PBSs. In the following, further possible limitations will be considered.

4.2 Setup Including an Active Fiber

4.2.1 Experimental Setup

For the experiments with an active fiber the experimental setup was changed as depicted in Fig. 4.8. An existing CPA laser system was used as the front- and back-end, where the passive DPA setup was inserted as the main amplification stage. The front-end, as roughly indicated in Fig. 4.8, included a passively mode-locked master oscillator delivering femtosecond pulses with a center wavelength of $\lambda_0 = 1030$ nm and a repetition rate of $f_{\text{rep}} = 40$ MHz. The pulses were stretched in a subsequent grating stretcher (possessing a spectral hard-cut of 7 nm) to a pulse duration of about $\Delta t = 2$ ns. Afterwards those pulses were amplified in the first pre-amplifier using a single-mode ytterbium-doped fiber with a core diameter of 6 μm . Additionally, an AOM was used to reduce the repetition rate. Then, a Spatial Light Modulator (SLM) was employed to compensate for any residual spectral phase (after the final recompression). The SLM was controlled by an active pulse shaping algorithm based on the Multiphoton Intrapulse Interference Phase Scan (MIIPS) [49] method. This was followed by the second pre-amplifier, which used an ytterbium-doped rod-type Photonic Crystal Fiber (PCF) [50] having a LMA [51] with a doped core diameter of 42 μm (mode-field diameter 45 μm) and a pump cladding diameter of 170 μm (which will be referred to as Large-Pitch Fiber (LPF) 30 in the following), and a second AOM, with which the repetition rate could be further reduced. The third pre-amplifier used another rod-type PCF with a doped core diameter of 49 μm (mode-field diameter 50 μm) and a pump cladding diameter of approximately 200 μm (LPF 35). Since this front-end was designed for a CBC setup, one of its main amplifiers, which also used rod-type PCF fiber (LPF 35), was employed as a further pre-amplifier operating at a relatively low power. All in all, an average output power of up to 4 W (depending on the experiment) was used as seed for the passive DPA setup. An isolator was used at the input to protect the front-end system for back-propagating beams. Subsequently, the beam diameter was enlarged to nearly $2w_0 \approx 5$ mm with a Galilei telescope consisting of two lenses with focal lengths of $f_1 = -40$ mm and $f_2 = 100$ mm.

an investigation at relatively low average power including three PBSs and an investigation with two PBS at high average power and high pulse energies were carried out. For the latter, just the bracketed elements were removed, as indicated in Fig. 4.8. Again, only one of the channels of each Mach-Zehnder type interferometer included a delay line, which had to be significantly larger than in the previous experiment to accommodate nanosecond pulses. The first one had a path length of $l_{\tau_1} \approx 2.05$ m, which corresponded to a temporal delay of $\tau_1 = l_{\tau_1}/c \approx 7$ ns, while the second one possessed a path length of $l_{\tau_2} \approx 4.06$ m, which corresponded to a temporal delay of $\tau_2 = l_{\tau_2}/c \approx 14$ ns. Those delays were sufficient to ensure no overlapping divided pulses. Additionally, the long Rayleigh length supported a relatively constant beam size over such long distances. Hence, in total eight (four) pulses entered the Sagnac loop. Within the loop an active fiber was placed. This was a rod-type PCF with a doped core diameter of $70 \mu\text{m}$ (mode-field diameter $70 \mu\text{m} - 80 \mu\text{m}$), a pump cladding diameter of approximately $280 \mu\text{m}$ (LPF 50), and a length of $L = 1.15$ m. It was optically pumped with a fiber-coupled pump diode laser module from the company LIMO [53] delivering a maximum average output power of 600 W at a center wavelength of 976 nm through a $400 \mu\text{m}$ core fiber. To obtain a good coupling of the pump power into the pump cladding of the active fiber, an especially designed pump coupling system from the Fraunhofer Institute was used. This comprised a lens system and a dichroic filter in order to transmit the pump wavelength and reflect the signal wavelength. This filter was oriented at an angle of 22.5° , whereby the combination of a 45° and 22.5° mirror was used to align the beam. For the measurements a pump-coupling efficiency of approximately 80% was assumed. Since the lens system (possessing an $f_{\text{eff}} \approx 20$ mm) between the filter and the fiber had to be used to focus the signal into the fiber core, a Galilei telescope was inserted in channel 32 to obtain a large magnification factor (for this two lenses with focal lengths of $f_1 = -30$ mm and $f_2 = 200$ mm were used). In channel 31, on the other hand, a lens with a focal length of $f = 60$ mm was placed in front of the fiber and a corresponding telescope comprising lenses with $f_1 = -30$ mm and $f_2 = 100$ mm were used. Both telescopes were chosen in such a way that at each side of the fiber the coupling efficiencies for the input beams were high and the emitted beams had nearly the same sizes. This was required to obtain a good beam overlap and, therefore, a good combining efficiency. Furthermore, a pump blocker was placed at the opposite side of the fiber (end without pump diode) in order to filter out the remaining pump power. Moreover, in the same channel an additional delay line was included to equalize the path lengths for both channels between the PBS_3 and the fiber facets. Finally, the combined output pulse was ejected at the open port of PBS_1 while the loss was back-propagating in the direction of the input and it was blocked by the isolator. Additionally, the output pulse could be sent through a compressor, which possessed an efficiency of approximately 80% , to remove the imprinted chirp.

This setup was used to investigate the amplification behavior of the temporally and spatially divided pulses as well as its influence on the combining efficiency. In the following the experiments will be explained, which focused on both obtaining a high average power and a high pulse energy, respectively. But first, the case of low average power will be considered, as a smooth transition from the passive to the active approach.

4.2.2 Experimental Investigations at Low Average Powers Using Three PBSs

With the setup described above the performance of the (CPA) DPA approach was investigated for the active case. Therefore, with the same temporal and spatial division scheme as for the proof-of-principle experiment, and one strongly stretched input pulse, the amplification characteristics at relatively low average output powers were tested. To obtain that division all HWPs were rotated so that a homogeneous division of the average power was obtained. Thus, according to Eq. (3.52), the rotation angle of the HWPs was close to $\theta = 22.5^\circ$ except for HWP₁₂, which was set to the negative angle $\theta = -22.5^\circ$. An average input power of $\bar{P}_{\text{in}} = 4 \text{ W}$ (measured in front of HWP₀) and a repetition rate of $f_{\text{rep}} = 4 \text{ MHz}$ delivered from the front-end system was used as seed. The adjustment of the whole setup for the proof-of-principle experiment was difficult, since each divided pulse corresponds to an individual beam, which must be focused into the fiber. It was not possible to determine a fiber coupling efficiency due to the absorption of the signal in the active fiber. Therefore, the coupling of each individual beam was adjusted so that their amplified output power was nearly the same. The amplified average output powers for each individual beams were measured directly after the fiber for launched pump powers up to approximately 55 W. These results are shown in Fig. 4.9a. In the legend the already introduced abbreviations have been used, whereby the given powers correspond to the remaining seed powers in front of the fiber. The differences between these seed powers were caused by the different losses of the paths and they resulted in a small spread of the output powers. Additionally, the combined outputs are depicted for both the case of all HWPs possessing a rotation angle of $\theta = 22.5^\circ$ and the case for HWP₁₂ possessing a negative angle. Those powers were measured at the output of PBS₁ without compression. The negative rotation angle of one of the first HWPs interchanges the output and the loss ports. Consequently, the dashed line corresponds to the loss. According to Fig. 4.5, HWP₁₁ should have possessed the negative angle since this would result in a better efficiency. However, in this case no significant difference in the efficiencies was observable. The difference between the powers of the single beams and the combined beam are caused by the system losses. While the depicted single beam graphs include just the system losses due to the forward propagation, the combined beam graph includes the losses due to the backward propagation as well. In Fig. 4.9b the powers of the single beams at the output (uncompressed) are shown. As be can seen, the amplified outputs were reduced, whereby the different paths caused different losses and, therefore, a further spread of the individual output powers. Now, the combined output power evolution falls almost in the middle of the other graphs. Consequently, the combined output is the average of all the single beam outputs, while each difference between them determines the combining losses (after Eq. (4.1)). According to that, a combining efficiency of $\eta_{\text{comb}} \geq 91.4\%$ (91.4% for the highest power) was achieved. Hence, in this low power regime no significant influences of the amplification process, such as saturation effects, were present. Furthermore, due to the reduced peak powers of the divided pulses, the accumulated nonlinear phases were negligible. However, a polarization efficiency of $\eta_{\text{LP}} = 92.5\%$ (DOLP = 85%, at the highest power) was measured. This resulted in a total system efficiency of $\eta_{\text{tot}} = 84.6\%$. Comparing it to the theoretically calculated one of Section 4.1.3, a better efficiency than expected

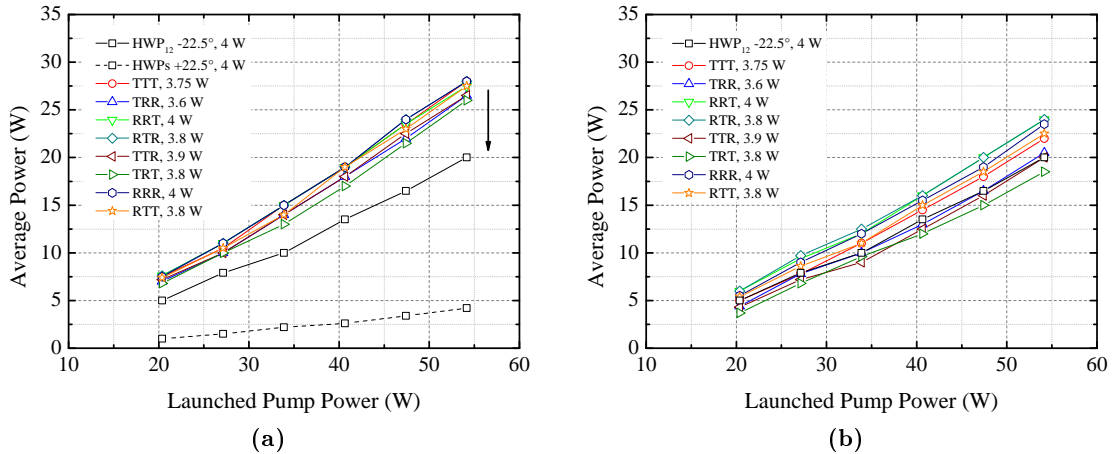


Fig. 4.9: Measured amplified output powers for the different possible paths of the single pulses (a) directly after the fiber and (b) uncompressed at the output after PBS₁. The combined output is depicted in both (HWP₁₂ $\theta = -22.5^\circ$), while in (a) the case for all HWPs having $\theta = 22.5^\circ$ is also indicated.

was obtained. This could be explained by the changes in the setup but also by a better splitting ratio of the PBSs than the assumed one.

In this experiment the pump power was not increased any further since distortions of some of the profiles of the individual beams were observable. The reason for these distortions was that the PBSs caused interference effects due to errors in their layer system or differences in the design wavelength. Due to the significantly larger beam sizes used here as compared to those of the proof-of-principle experiment, these effects were clearly visible. The PBSs of lower quality, i.e. those degrading the beams most, were sorted out. Just one PBS (from the company Edmund Optics) remained. This together with another one from the company ALTECHNA (compatible with high-power applications and with $T_p > 97\%$ and $R_s > 99.5\%$ [52]) were used for the rest of the experiments. Consequently, the complexity of the setup was reduced to two PBSs, where PBS₂ and the corresponding HWPs were removed (named in brackets in Fig. 4.8) and the ALTECHNA PBS was placed at the position of PBS₃. In the following, the cases of high average output power and high pulse energy will be considered with this reduced setup.

4.2.3 Experimental Investigations at High Average Power Using Two PBSs

As discussed in the previous section, the setup was reduced to just two PBSs, whereby PBS₂ and its corresponding HWPs were removed. Hence, the total path lengths through the setup remained unchanged but the beams crossed each other at the virtual position of PBS₂. Those pulses propagating along channel 11 (delay line 1) to channel 22 corresponded to the undelayed pulses, while those propagating along channel 12 to channel 21 (delay line 2) were delayed. In total, four pulse replicas were produced. These counter-propagated through the Sagnac loop in groups of two. Due to the crossed beam paths, either HWP₂₁ or HWP₂₂ had to be set to a

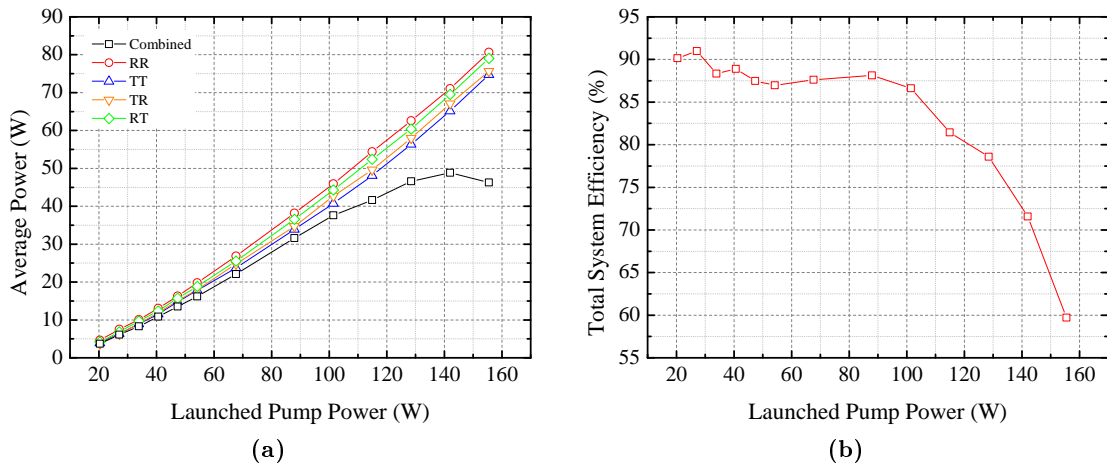


Fig. 4.10: (a) Measured amplified output powers after the compressor for the different possible paths of the single pulses and for the combined output and (b) calculated total system efficiency.

negative rotation angle in order to eject the combined output beam at the right port of PBS₁. Afterwards, the output was sent through the compressor to remove the imprinted chirp. Since the efficiency of the compressor is polarization-dependent (i.e. just linearly polarized light was efficiently transmitted), the measured combined output power after the compressor related to the average value of all possible single pulse paths corresponds to the total system efficiency, as given by Eq. (3.22). As before, an average input power of $\bar{P}_{\text{in}} = 4 \text{ W}$ and a pulse repetition rate of $f_{\text{rep}} = 4 \text{ MHz}$ were chosen as the seed delivered from the front-end system.

In Fig. 4.10a the measured compressed average output powers are shown of both the combined beam and for the four possible single pulse beams. The pump power was increased up to a maximum value of nearly $\bar{P}_{\text{pump}} \approx 160 \text{ W}$. As in the previous experiment, the powers for the different single pulse beams increased linearly with the pump power but they were slightly spread due to the different system losses. Thereby, the pulses traveling along the path \overline{TT} accumulated the largest amount of loss, while those along the path \overline{RR} accumulated the smallest amount of loss, as expected. The slope efficiencies (η_{slope}) ranged from 52% to 56% (after compression). If the pump power was increased further above 160 W (leading to amplified output powers $\bar{P}_{\text{out}} > 90 \text{ W}$ for each single-pulse beam) thermal instabilities led to fluctuations of the mode profile. This could be explained by mode instabilities [54] but it was not further investigated and it certainly exceeds the scope of this work. In contrast, for the combined output this instability was even observed for a pump power of $\bar{P}_{\text{pump}} \approx 142 \text{ W}$, which corresponded to a combined output power of around $\bar{P}_{\text{out}} \approx 50 \text{ W}$. Up to that point, the slope efficiency amounted to $\eta_{\text{slope}} = 41\%$. In Fig. 4.10b the achieved total system efficiency is depicted, which was calculated similarly to Eq. (4.1), but where the combined output power already includes the polarization efficiency due to the compressor. Another measurement of the polarization efficiency at the output of PBS₁ as a function of the pump power showed an increasing behavior from $\eta_{\text{LP}} \approx 86\%$, for $\bar{P}_{\text{pump}} < 68 \text{ W}$, to $\eta_{\text{LP}} \approx 92\%$, where it remained nearly constant. The reason for that increase may be found in the measurement accuracy of the thermal detector at low

powers or the reduced amount of cladding-light at high powers. The efficiency of the compressor is not relevant for the calculation of the combining efficiency, since it is contained in both the combined output power and the single beam powers. As can be seen, up to a pump power of $\bar{P}_{\text{pump}} \approx 100 \text{ W}$ the total system efficiency remained approximately constant at a promising value of $\eta_{\text{tot}} > 87 \%$. However, with a further increase of the pump power the efficiency started to decrease steadily below $\eta_{\text{tot}} \approx 80 \%$. For pump powers $\bar{P}_{\text{pump}} > 130 \text{ W}$ it dropped significantly towards $\eta_{\text{tot}} \approx 60 \%$.

For all output powers up to this drastic degradation a constant autocorrelation duration of $\Delta t_{\text{AC}} = 760 \text{ fs}$ was measured for the combined case. In order to obtain the temporal pulse duration, the pulse shape must be known. For example, a Gaussian or a Sech^2 -like shape can be assumed. Then, the pulse duration can be calculated from the autocorrelation duration with a so-called deconvolution factor (see Appendix D). But it is more accurate to use the simulation software FiberDesk to calculate this factor from the measured output spectrum. With this procedure, a deconvolution factor of 0.691 was obtained, which corresponded to a pulse duration of $\Delta t \approx 526 \text{ fs}$. For a combined output power of $\bar{P}_{\text{out}} \approx 49 \text{ W}$, and when using Eq. (2.12) and Eq. (2.13), a peak power of $\hat{P}_{\text{out}} \approx 23.2 \text{ MW}$ was achieved. Thus, a temporal division of the pulses seems to be just justified for a system delivering high average power when non-stretched pulses are used. Consequently, in this regime the CPA technique seems to be sufficient. However, if the combined output power can be increased, due to some improvements, towards the limit of the CPA approach, when nonlinear effects would become significant, the temporal division would decrease the peak power and, therefore, mitigate those effects.

The main reason for this reduction of the combining efficiency are thermal effects. For example, for higher average powers, mode shrinking may occur in the fiber during amplification due to the unavoidable heat load and its associated refractive index change [55]. These temperature-induced waveguide changes become more severe for larger mode-field diameters. Since the fiber is typically pumped only from one side, the heat load is usually higher at or near this fiber end. Therefore, with increasing power, the beam sizes emitted at both fiber ends change differently. As a result, the beam sizes do not perfectly match any more at the PBSs which reduces the combining efficiency. However, in principle this issue can be overcome with a symmetric heat distribution along the fiber, which implies using a double-sided pumping or two separate amplifiers within the Sagnac loop.

Moreover, the emitted beam profiles at both fiber ends may be different due to production tolerances for a particular fiber design due to the preparation of the ends. In Fig. 4.11 the beam profiles for a pump power of $\bar{P}_{\text{pump}} \approx 115 \text{ W}$ are shown for the single pulse beams and for the combined beam at the output of PBS₁. In Fig. 4.11a and Fig. 4.11b the profiles of the beams that counter-propagate with respect to the pump beam are depicted, while Fig. 4.11c and Fig. 4.11d show the co-propagating beams. As can be seen, the counter-propagating beams possessed a larger, flatter beam profile. Interestingly, the co-propagating beams possessed a smaller beam diameter since they were emitted at the "colder" side of the fiber. This could be understood taking into account that Fig. 4.11 represents far-field beam profiles. Thus, after approximately 9 m propagation an initially smaller beam (smaller Rayleigh length) will typically diverge more than a bigger one. Consequently, this leads to an initial reduction of the combining efficiency

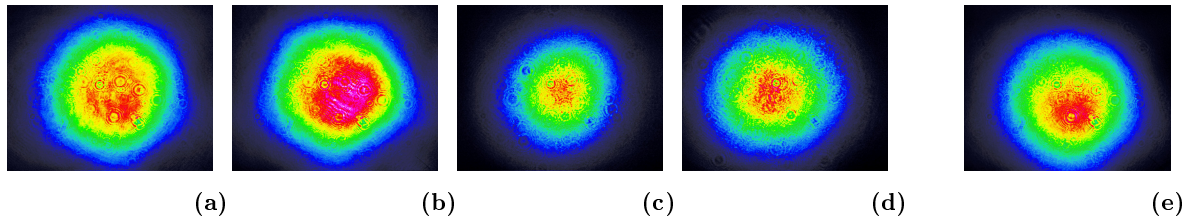


Fig. 4.11: Measured beam profiles (at $\bar{P}_{\text{pump}} \approx 115$ W) of the individual beams (a) \overline{RR} , (b) \overline{TT} , (c) \overline{TR} , (d) \overline{RT} , and (e) the combined beam.

at the PBSs, according to [56, 57]. Finally, in Fig. 4.11e the combined output beam profile is depicted, which shows an improved beam profile compared to the individual beams.

Moreover, the thermal load of the optical elements, as for example the PBSs, may lead to thermal lensing, which can disturb the different pulses dissimilarly because of the different path lengths that each travel through the setup. The unequal path lengths of the temporally divided pulses may lead to different aberration effects during their propagation, which changes their wavefronts. Due to the waveguide characteristics of the fiber this is not important for the forward-propagating beams but it definitely affects the back-propagating beams. This can influence the quality of the combination at a PBS.

Furthermore, a non-perfect spatial recombination of the delayed pulses at a PBS may lead to failure fractions of a different polarization, which propagate back through the wrong delay line producing pre- or post-pulses. Those pulses are delayed in the nanosecond range, which causes fast modulations (with small periods) in the output spectrum of the combined beam. In Fig. 4.12a the spectra of the single pulse beams \overline{RR} and \overline{TT} , as well as that of the combined beam compared to the input spectrum are shown. All these spectra were measured at the output of PBS₁. As can be seen, the bandwidth of $\Delta\lambda \approx 3$ nm remained nearly the same for all cases, besides a negligible broadening of the spectra for the single pulse cases. The edges at the short wavelength side of the amplified spectra were suppressed because of gain narrowing. While the impact of nonlinear effects, even for the single pulse beams, at high average powers is significantly reduced by the fiber design and by the strong stretching of the pulses, a non-perfect temporal combining generates modulations (with larger periods) in the spectrum (due to the slightly shifted pulses). Those modulations arose at a launched pump power in the range of $\bar{P}_{\text{pump}} \approx 142$ W and became stronger for higher powers.

Another reason for the degradation of the combining efficiency may be the different amplification behavior between the counter-propagating pulses as well as between the delayed pulses. Due to the asymmetric pump geometry the inversion is distributed asymmetrically, too. Furthermore, the temporally delayed pulses do not undergo as high an amplification as the first amplified pulses. The first pulse depletes the inversion, which results in a reduction of the gain (caused by saturation) for the next pulses, since a gain medium cannot provide an arbitrarily high gain for arbitrarily high input powers [58]. In Fig. 4.12b the amplified pulses after the fiber amplifier within the Sagnac loop for one channel are shown for both a pump power of $\bar{P}_{\text{pump}} \approx 54$ W and $\bar{P}_{\text{pump}} \approx 115$ W. They were measured with an oscilloscope and a photo diode that possessed a time constant of approximately 1 ns. Since the pulse durations were in the range of 2 ns, these

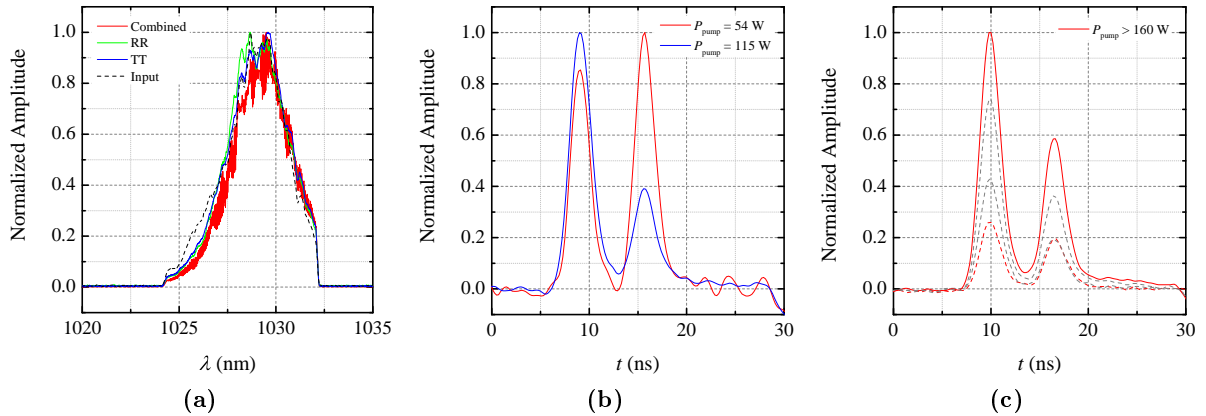


Fig. 4.12: (a) Measured spectra with $\bar{P}_{\text{pump}} \approx 142$ W for two different paths of the single pulse beams and for the combined output beam, compared to the input spectrum. (b) Amplified pulses within one channel of the Sagnac loop for the pump powers $\bar{P}_{\text{pump}} \approx 54$ W and $\bar{P}_{\text{pump}} \approx 115$ W, and (c) several single shot measurements with $\bar{P}_{\text{pump}} > 160$ W.

were at the limit of the resolution. Anyway the measurement was accurate enough to show the temporal separation of the pulses. The oscillations after them were caused by ringing of the electronics. For pump powers up to $\bar{P}_{\text{pump}} \approx 54$ W the ratio of the peak powers of the delayed pulses equaled that of the input pulses (red curve in Fig. 4.12c). For increasing power the first pulse obtained progressively more amplification, but the inversion could not be built up fast enough to provide the same gain for the second pulse. Consequently, at high output powers unequal peak powers of the delayed pulses sets in (blue curve in Fig. 4.12c). For pump powers $\bar{P}_{\text{pump}} > 130$ W the mentioned thermal effects dominated, which ultimately limited the combined output power. As an example, the amplified pulses after the fiber amplifier for the same channel at a pump power of $\bar{P}_{\text{pump}} > 160$ W were measured. Fig. 4.12c shows some arbitrarily chosen single-shot measurements at different times. As can be seen, strong fluctuations occurred. This again might have been caused by the mentioned mode instabilities, since fluctuations of the output mode were observable with the camera. This, however, is beyond the scope of this work. Another possibility is that the thermally induced change of the optical elements and a temperature-dependent expansion of the fiber change the focusing of the seed signal into the fiber and, hence, lead to different seeds for the amplification.

Most of the drawbacks seem to be caused by employing the Sagnac geometry and not by the DPA approach. As a consequence, a setup without an active stabilization system is viable for high average powers up to a certain limit, that is determined by thermal effects. However, its advantage, together with the DPA approach, will only be significant if no CPA technique should be applied.

4.2.4 Experimental Investigations at High Pulse Energy Using Two PBSs

To investigate the properties of the setup operating at high pulse energies, the input delivered by the front-end system was changed. Thus, the amplification characteristics of the pre-amplifiers were modified and the repetition rate was reduced with the help of the AOMs. This resulted in an input seed signal with an average power of $\bar{P} = 600 \text{ mW}$ and a repetition rate of $f_{\text{rep}} = 20 \text{ kHz}$. According to Eq. (2.12), this corresponded to a pulse energy of the input pulses of $E_p = 30 \mu\text{J}$. The stretched pulse duration of $\Delta t = 2 \text{ ns}$ remained unchanged. With this, the same series of measurements for the possible single pulse paths and the divided pulses as before, were acquired. In Fig. 4.13a the measured average output powers after the compressor are shown. Additionally, a second ordinate was attached showing the calculated output pulse energies, after Eq. (2.12). Considering first the single pulse cases, the pulse energies (E_p) were in the range of 0.79 mJ to 0.93 mJ . The pump power/pulse energy was not increased any further, since the measured pulse shape and the spectrum degraded significantly. Similar to Fig. 4.10a, the highest value belongs to the path \overline{RR} , while, surprisingly, the order of the other paths was interchanged and the lowest value now belonged to the path \overline{TR} . The reason for that may be the rotation angles of the HWPs used to chose between the individual beams, since the positioning was very sensitive. For the measured values a range of slope efficiencies (η_{slope}) of 31% to 37% was obtained.

Next, equal power division at the PBSs was applied by setting all HWPs to the rotation angles $\theta = 22.5^\circ$, as described for the high average power measurements. With this, a significant reduction of the achieved combined average output power was observable, which resulted in a maximum achieved pulse energy of approximately $E_p = 0.52 \text{ mJ}$. A slope efficiency of just $\eta_{\text{slope}} \approx 23 \%$ was obtained, which degraded for launched pump powers $\bar{P}_{\text{pump}} > 54 \text{ W}$. Ultimately, for pump powers $\bar{P}_{\text{pump}} > 68 \text{ W}$ no further increase of the combined output power was achievable.

The total system efficiency (η_{tot}) is depicted in Fig. 4.13b, which again was calculated as before similarly to Eq. (4.1). It decreases almost linearly from approximately 78% to 60% for the range of the launched pump power (27 W to 68 W). In contrast to the case of high average power, no sudden degradation of the efficiency due to a strong influence of thermal effects is observable. This is because now the thermal load of the fiber and all optical elements was significantly lower, since the average powers were lower. The main reason for the steady degradation of the efficiency was the non-negligible nonlinear phases accumulated by the pulses. According to Eq. (2.38) and Eq. (2.39), there should be a significant influence of SPM and, additionally, of XPM. In Fig. 4.14a the measured spectra of both the single pulse case (\overline{RR}) and the combined case at a pump power of $\bar{P}_{\text{pump}} \approx 68 \text{ W}$ are shown. As can be seen, there are strong modulations on the spectrum for the case of one single pulse [59], which leads to a dramatic change of the pulse shape. In contrast, the spectrum of the combined output shows considerably lower modulations, which highlights the advantage of the temporal and spatial division of the pulses. The reduced peak power mitigates the influences of nonlinear effects. However, due to the asymmetric pump geometry and, therefore, the higher inversion at the pump-side, the co-propagating pulses may acquire a larger amount of SPM compared to the counter-propagating pulses. Further-

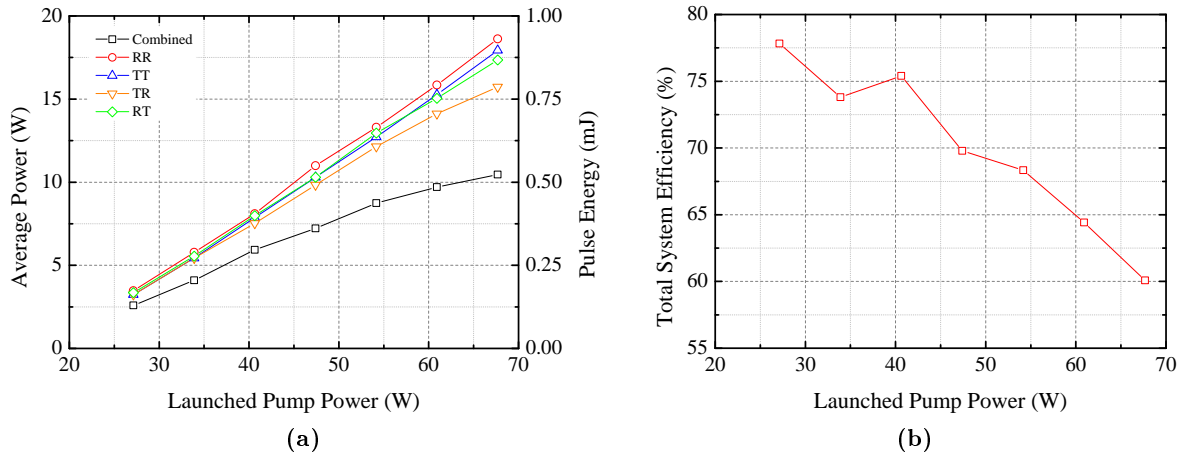


Fig. 4.13: (a) Measured amplified output powers and resulting pulse energies after the compressor for the different possible paths of the single pulses and the combined output, and (b) the calculated total system efficiency.

more, due to the relatively long interaction length of the strongly stretched counter-propagating pulses within the fiber, XPM causes another significant amount of nonlinear phase. But this is different for each pulse, since they are differently amplified and possess different peak powers. Moreover, the pulses are not perfectly s - or p -polarized, which causes significant differences in the acquired XPM phases for the two polarization components (due to the factors of $2/3$ and 2 , see Eq. (2.38) and Eq. (2.39)). Consequently, the total accumulated B -integrals were different in each pulse which led to the dramatic degradation of the efficiency. A strongly asymmetric Sagnac loop, that prevents the crossing of the pulses within the fiber, prevents the onset of XPM. The autocorrelations corresponding to the different spectra were measured, as shown in Fig. 4.14b. While for all pump powers the autocorrelation duration of the combined pulse remained constant at $\Delta t_{AC} = 880$ fs, that of one single pulse increased steadily up to an autocorrelation duration of $\Delta t_{AC} = 1.35$ ps for a launched pump power of $\bar{P}_{\text{pump}} \approx 68$ W. Moreover, the pulse shape

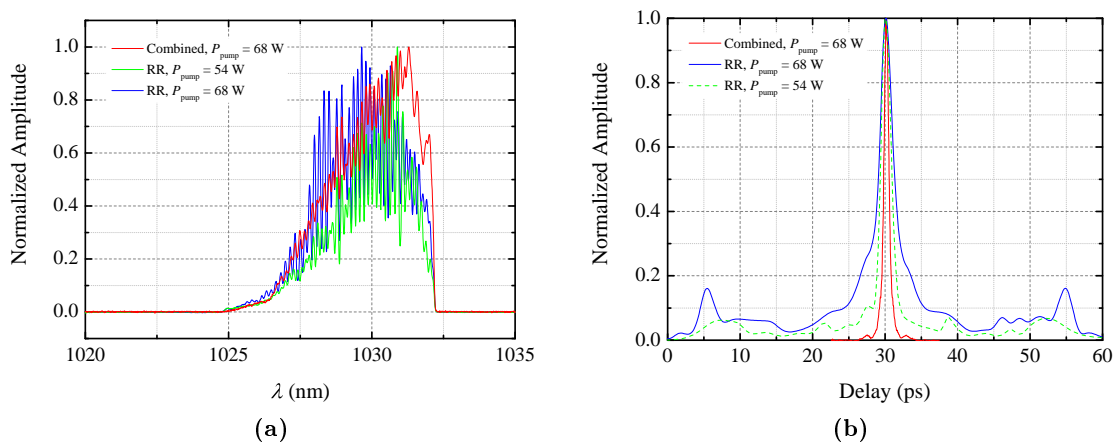


Fig. 4.14: (a) Measured spectra of the single-pulse path \overline{RR} for two pump powers and of the combined pulse and (b) the corresponding autocorrelations.

degraded and detrimental pre- and post-pulses arose. This demonstrates the advantage of the DPA approach, since the accumulated total nonlinear phase of the pulses is much lower than that of single pulse case. Although the efficiency dropped significantly up to that maximum pump power, the overall launched power for both the single pulse and the combined pulse was the same. However, to compare output pulses of nearly the same pulse energy, the combined pulse at a pump power of $\bar{P}_{\text{pump}} \approx 68 \text{ W}$ and the single pulse at a pump power of $\bar{P}_{\text{pump}} \approx 47 \text{ W}$ can be used. Unfortunately, the autocorrelations were measured just at both $\bar{P}_{\text{pump}} \approx 41 \text{ W}$ and $\bar{P}_{\text{pump}} \approx 54 \text{ W}$. Nevertheless, both resulted in the same autocorrelation duration of $\Delta t_{\text{AC}} = 1 \text{ ps}$, whereby that at the slightly higher pump power is additionally depicted in Fig. 4.14b. The achieved autocorrelation durations were optimized with the MIIPS to compensate for residual spectral phases.

Finally, the peak powers can be calculated. In Tab. 4.2 the calculated values are summarized for the achieved maximum of the combined pulse and for both the single pulse of roughly the same pulse energy and for that of the same pump power. Therefore, an input power of $\bar{P}_{\text{in}} = 600 \text{ mW}$, a repetition rate of $f_{\text{rep}} = 20 \text{ kHz}$, and Eq. (2.12) as well as Eq. (2.13) were used. Again, with the help of FiberDesk the deconvolution factors for the three cases were determined, to obtain the corresponding pulse durations. The gain was roughly estimated as the ratio of the output power (which was assumed by taking out the compressor efficiency from the measured compressed output power) and the input power. As can be seen, while the shortest pulse duration was obtained with the combined pulse, a higher peak power was obtained for both single pulse cases. But these differences are mainly caused by the differing average output powers (10.5 W for the combined case and 13.3 W for the single pulse case) when comparing those with approximately the same pulse energy. Additionally, the B -integrals were estimated. With the help of the implemented MATLAB[®] simulation tool (XPM not considered) including the Fourier Split-Step method now extended by a simple exponential amplification model (the same for both input signals), the B -integrals were calculated by assuming the given parameters of the input and the fiber as well as the PBSs having $R_s = 99 \%$ and $T_p = 95 \%$. The calculated B -integrals for those cases are listed in Tab. 4.2. Since the divided pulses had in this case different peak powers (compare with Fig. 3.6), their accumulated phases were also different. Hence, the B -integral value given in Tab. 4.2 for the combined case corresponds to the maximum value of the four pulses. The advantage compared to the non-divided pulses is, as can be seen, the lower total accumulated nonlinear phase. In spite of this, with the passive combining approach used no improvement of the extracted pulse energy and, therefore, of the peak power was achieved, when compared to

Tab. 4.2: Calculated output pulse durations and peak powers for the combined and single pulse case with simulated B -integrals.

Case	\bar{P}_{out} (W) measured	Gain	Deconv. Factor	Δt (fs)	\hat{P}_{out} (MW) compressed	B -int. (rad) SPM
Combined ($\bar{P}_{\text{pump}} \approx 68 \text{ W}$)	10.5	17	0.683	601	870	max. 2.7
Single \overline{RR} ($\bar{P}_{\text{pump}} \approx 54 \text{ W}$)	13.3	22	0.686	697	954	5.8
Single \overline{RR} ($\bar{P}_{\text{pump}} \approx 68 \text{ W}$)	18.6	31	0.630	857	1087	7.5

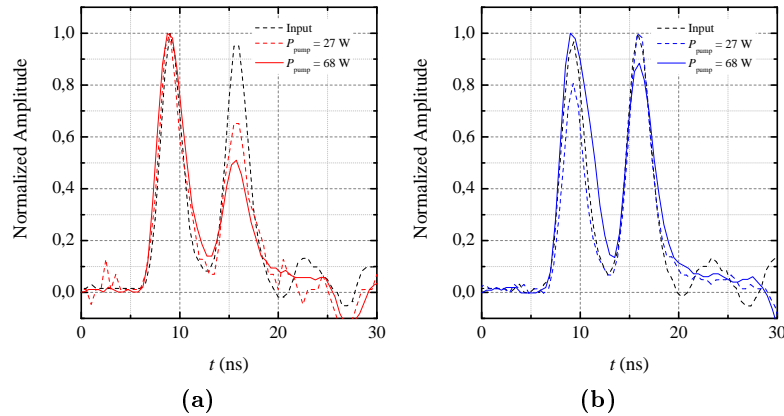


Fig. 4.15: Impact of the saturation effect on the pulse ratio for (a) the co-propagating pulses and (b) the counter-propagating pulses with respect to the pump beam.

the single pulse case. However, although the B -integral for the combined case is smaller, it is still high enough to affect the combining efficiency, which may be improved by a further division of the pulses.

Another cause for the degradation of the efficiency may be the saturation effect, as already mentioned in the previous section. Each first pulse of the counter-propagating pulses within the Sagnac loop undergoes a higher amplification than the subsequent pulses. Due to the asymmetric pump geometry the co- and the counter-propagating pulses with respect to the pump beam are also affected differently. Fig. 4.15 shows the normalized amplified pulses compared to the input pulses for both directions. As can be seen, the saturation effect is more drastic for the co-propagating pulses. Surprisingly, that was comparable for both the case of high average power and high pulse energy. This difference in the pulse ratio affects the resulting polarization states at the combining stages and, consequently, the amount that is finally ejected at the output port or at the loss port of PBS₁. The impact of this effect and also of the accumulated nonlinear phase will be considered in more detail in the following.

4.2.5 Theoretical Investigations and Discussion

With the help of the implemented MATLAB[®] simulation tool, which was introduced in Section 4.1.3 and which was extended by a simple exponential amplification model, the passive DPA setup including an active fiber will be theoretically investigated in the following. Hereby, the focus will be on the impact of a changed pulse ratio and of the nonlinear effects SPM and XPM.

As mentioned, the realistic splitting ratio of the lossless PBSs can lead to significant variations of the magnitudes of the temporally and spatially divided pulses. This results in a baseline loss of the setup that depends on the magnitude of the parameters R_s and T_p . Additionally, the amplitude ratio of consecutive pulses changes due to saturation in an amplifier. Thus, the first

pulse of a series is more amplified than the following pulses, since for the latter the inversion is depleted and it cannot be built up fast enough. Furthermore, the pulse ratio between the channels can be changed, in case for example that one channel is more amplified/better coupled in the fiber than the other one. In the following, the influence of different pulse ratios for the case of a division into four pulses will be considered. Therefore, based on the setup sketched in Fig. 3.5b, Eq. (3.42) and Eq. (3.43) will be used, which describe the fields directly after PBS₂. But only ideal PBSs will be considered with $R_s = T_p = 100\%$, otherwise the resulting expression would be too extensive. Consequently, the peaks of the divided pulses at the input are equal and the ideal ratio of those pulses is 1. To describe a deviation from this ideal case in terms of ratios, a difference of the pulse peaks is introduced in such a way that the total energy content of both pulses is not changed (no amplification is considered). Hence, starting from the ideal ratio of 1, when the first pulses are increased by half the difference, the delayed pulses are decreased by that same amount. Since this difference can change for counter- (channel 21) and co-propagating (channel 22) pulses with respect to the pump beam, it is referred to as ξ_1 and ξ_2 . This is illustrated in Fig. 4.16a. Additionally, it is possible that the total ratio between the pulses from channel 21 and those from channel 22 changes. In order to model this, a parameter ξ_0 that represents the difference with the ideal case is introduced, which is illustrated in Fig. 4.16b. While both pulses of channel 21 are decreased by half the value of ξ_0 , the pulses of channel 22 are increased by that amount, which was arbitrarily chosen. Thus, using Eq. (3.42) and Eq. (3.43) (and including the mirrors of the Sagnac loop into the calculation to obtain the fields which would enter the fiber at both sides) and by applying these differences as weighting factors to change the pulse ratios, it follows

$$\mathbf{E}_{21}(\mathbf{r}, t) = \frac{i}{2} \sqrt{1 - \frac{\xi_0}{2}} \sqrt{1 + \frac{\xi_1}{2}} E(z, t) \hat{\mathbf{x}} + \frac{i}{2} \sqrt{1 - \frac{\xi_0}{2}} \sqrt{1 - \frac{\xi_1}{2}} E(z, t - \tau_1) \hat{\mathbf{y}} \quad (4.3)$$

$$\mathbf{E}_{22}(\mathbf{r}, t) = -\frac{1}{2} \sqrt{1 + \frac{\xi_0}{2}} \sqrt{1 + \frac{\xi_2}{2}} E(z, t) \hat{\mathbf{y}} - \frac{1}{2} \sqrt{1 + \frac{\xi_0}{2}} \sqrt{1 - \frac{\xi_2}{2}} E(z, t - \tau_1) \hat{\mathbf{x}}. \quad (4.4)$$

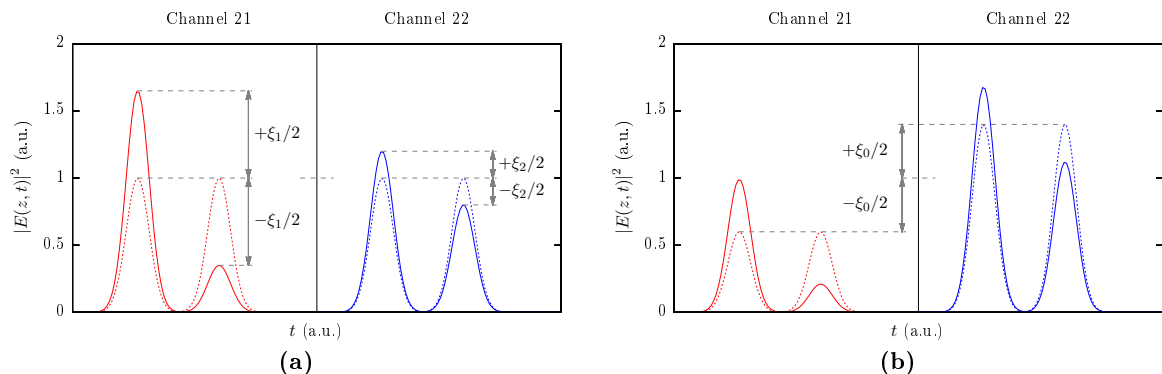


Fig. 4.16: Illustration of the variation of the pulse peak ratio (a) between the first and second pulse of channel 21 and channel 22, and (b) between both channels.

The square roots were introduced, since complex fields are considered. Since it is more convenient to use ratios, the difference in the pulse peaks can be defined with the help of the pulse peak ratios \mathcal{R}_m as

$$\xi_m = 2 \frac{1 - \mathcal{R}_m}{1 + \mathcal{R}_m} \quad , \quad (4.5)$$

where $m = 0, 1, 2$. Thereby, the pulse peak ratio is defined as the ratio of the delayed pulse to the first pulse, which typically is $0 \leq \mathcal{R} \leq 1$, since usually the first pulse peak becomes larger than the second. Calculating now the back propagation of these fields, by assuming no fiber within the Sagnac loop, which means no further influences due to dispersion, nonlinear phases or additionally amplification ($G = 1$, since this influence is now expressed by the weight factors), and using Eq. (3.44) and Eq. (3.45) as well as calculating the power loss fraction by using Eq. (3.47) and Eq. (2.10), it results

$$P_{\text{loss}}(z, t) = C \frac{(\mathcal{R}_0 + 1) \sqrt{\mathcal{R}_1 + 1} \sqrt{\mathcal{R}_2 + 1} - 2\sqrt{\mathcal{R}_0 \mathcal{R}_1 \mathcal{R}_2} - 2\sqrt{\mathcal{R}_0}}{2(\mathcal{R}_0 + 1) \sqrt{\mathcal{R}_1 + 1} \sqrt{\mathcal{R}_2 + 1}} |A(z, t)|^2 \quad . \quad (4.6)$$

The percentage of the loss, by relating Eq. (4.6) to the input $P_{\text{in}}(z, t) = C |A(z, t)|^2$, dependent on the pulse peak ratios \mathcal{R}_1 and \mathcal{R}_2 is shown in Fig. 4.17a for both a total ratio $\mathcal{R}_0 = 1$ (left), which means no change of the ratio between the two channels, and for an arbitrarily chosen $\mathcal{R}_0 = 0.3$ (right). Considering first the former, if the ratios \mathcal{R}_1 and \mathcal{R}_2 are identical, this has no impact on the combined output for that ideal case and it would just change the orientation of the output polarization (according to Eq. (2.17)). Furthermore, any variation of both ratios, \mathcal{R}_1 and \mathcal{R}_2 , decreasing from 1 to 0.3 lead to a negligible loss of smaller than 2%. It is remarkable that these losses are small even though for ratios of 0.5 the first pulse becomes twice as high as the second one. Ultimately, a further decrease of the pulse peak ratio of one of the channels to 0.1, whereas the other remains 1, leads to a loss of nearly 6% and ends up at nearly 15% for the extreme ratio of 0. Now, the change of total ratio is shown in Fig. 4.17a. In the right-hand side of the figure the same variation but for $\mathcal{R}_0 = 0.3$ can be seen. As can be observed clearly from the coloring, there is a baseline loss of approximately 8% even for identical ratios of \mathcal{R}_1 and \mathcal{R}_2 . Nevertheless, it shows the same behavior as before and it leads to losses of nearly 13% for a pulse peak ratio of 0.1 in one channel (when that of the other one remains at 1) and, ultimately, to approximately 20% for the extreme ratio of 0. Consequently, a changed ratio between both channels results in a stronger impact on the combining efficiency than a variation of the individual pulse heights of the temporally delayed pulses within one channel. Finally, the impact for the measured pulse peak ratios can be determined. According to Fig. 4.15b and Fig. 4.15a from the previous section, it resulted in a changed pulse ratio of $\mathcal{R}_1 = 0.74$ for the counter-propagating and $\mathcal{R}_2 = 0.39$ for the co-propagating pulses (which corresponds to peak differences of $\xi_1 = 0.15$ for Fig. 4.15b and $\xi_2 = 0.44$ for Fig. 4.15a including the small initial difference of the input pulses). In Fig. 4.17b the variation of \mathcal{R}_0 for those values is shown (red solid line). Moreover, the ideal case of $\mathcal{R}_1 = \mathcal{R}_2 = 1$ (green dashed line) and the more extreme case of $\mathcal{R}_1 = 1$ and $\mathcal{R}_2 = 0.1$ (blue dashed line) are depicted for comparison. As can be seen, the measured case differs just slightly from the ideal case for the whole \mathcal{R}_0 range. The measured ratios were obtained from two independent photo-diodes. Hence, a total ratio between the channels could

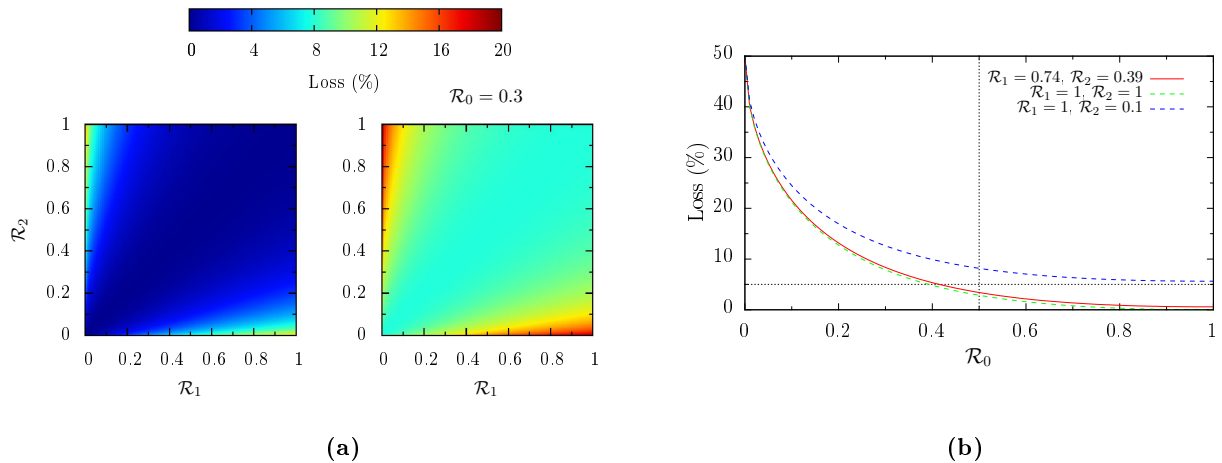


Fig. 4.17: Impact of the pulse peak ratios on the combining efficiency for (a) the variation of \mathcal{R}_1 and \mathcal{R}_2 for a given \mathcal{R}_0 , and (b) the variation of \mathcal{R}_0 for given \mathcal{R}_1 and \mathcal{R}_2 .

not be measured directly. However, with the help of the relative measurements of the initial pulses and the amplified pulses for one channel, whereby the peak differences for the different ratios were subtracted out, the growth of the amplified pulses can be determined. Relating the obtained values for channel 21 and channel 22, a total ratio of $\mathcal{R}_0 = 0.9$ came out. However, the sensitivity of both photo-diodes may have been different, which may have influenced the resulting peak differences. Nevertheless, as seen in Fig. 4.17b, the determined ratios have nearly no impact on the combining efficiency, and even a further reduction of the total ratio down to $\mathcal{R}_0 = 0.5$ would lead to a loss smaller than 4%. Consequently, the impact of the variations of the pulse peaks were negligible in our experiments.

The influence of the rotation angles of the HWPs for a fixed pulse ratio was investigated, which may be used for a correction of the pulse heights or to obtain an improvement of the combining efficiency. However, since the calculated loss for the measured pulse ratios is negligible small, no improvement is really needed. Nevertheless, this factor becomes important for lower ratios. In Fig. 4.18 the combining efficiency as a function of the rotation angles of the HWPs is shown for arbitrarily chosen ratios $\mathcal{R}_1 = 0.2$, $\mathcal{R}_2 = 0.9$, and $\mathcal{R}_0 = 0.2$. In this case, those constant factors were assumed as different relative gain factors, which were fixed for the individual pulses. The combined output was now related to the changed magnitude of the total field including all factors, which, therefore, results in a maximum efficiency of 100%. This was done, since the ratios of the input pulses in the Sagnac loop are modified due to the varied HWPs. However, in contrast to the ideal case, where the pulse ratios are not changed and the settings of the HWPs scale linearly, the settings for a significant change of the ratios may be optimized to improve the efficiency, according to Fig. 4.18. This may become even more important for setups including more than two PBSs. But a changed input pulse ratio, which would enter the fiber, may also change the impact of other effects, as for example SPM, which may again reduce the efficiency. Next, the impact of the nonlinear phases due to SPM and XPM will be discussed. In order to do this the implemented MATLAB[®] simulation tool was used. The principle setup remained

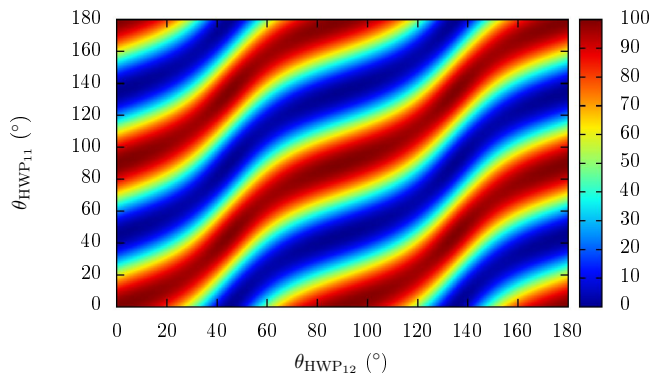


Fig. 4.18: Simulation of the combining efficiency (color-coding in percent) of the possible combinations of rotation angles in a setup containing two PBSs ($T_p = 95\%$ and $R_s = 99\%$) for fixed pulse ratios within the Sagnac loop of $\mathcal{R}_1 = 0.2$, $\mathcal{R}_2 = 0.9$, and $\mathcal{R}_0 = 0.2$ ($\theta_{\text{HWP}_0} = 22.5^\circ$).

the same but now the PBS splitting ratio was more realistic with $R_s = 99\%$ and $T_p = 95\%$. Hence, the losses due to the PBSs, as discussed in Section 4.1.3, were already included, which amounted approximately to 11% for the chosen parameters. The impact of the change of the pulse ratios was excluded, since the simulation tool is based on a simple exponential amplification model, without considering saturation effects. Furthermore, the exponential gain was considered to be the same for both co- and counter-propagating pulses. This is a rough assumption, since the inversion is asymmetrically distributed due to the one-sided pump geometry. With these assumptions, the impact of SPM was simulated for both one pulse (\overline{RR}) and for the division into four pulses. Therefore, the total accumulated nonlinear phases, that is the B -integrals, were calculated. To obtain values comparable to the measurements, the simulated average output powers (including the system losses) at the output port of the division setup (PBS₁) for the case of one pulse were fitted to those of the measurements with the help of the gain factor G at each measuring point. Unfortunately, just the compressed average output powers were measured. The output after the combining setup is obtained by taking out the compressor efficiency, but there is no information about the polarization efficiency. However, assuming no significant change of the polarization efficiency for the case of a single pulse, a maximum gain factor of $G \approx 40$ was obtained. The same gain factors were assumed for the case of the division into four pulses, even though in reality, they may have been different. The results of the calculated B -integrals are depicted in Fig. 4.19a. As can be clearly seen, the amount of the total accumulated nonlinear phase is approximately four times larger for the single pulse when compared to the division into four pulses (named as co- and counter-propagating pulse 1 and 2, respectively), which demonstrates the advantage of the reduction of the peak power. While a maximum value of $B = 7.5$ rad was obtained for one pulse, a range of 1.1 rad to 2.7 rad was obtained for four pulses. This range of B -integrals is caused by the different peak powers of the individual pulses due to the splitting ratios of the PBSs. If the splitting ratios would be ideal, the B -integrals of the individual pulses would be identical. Furthermore, the total

system efficiency was calculated with the help of the defined combining efficiency, according to Eq. (4.1), and the polarization efficiency, by using Eq. (3.21) and Eq. (4.2). The result is shown in Fig. 4.19b together with the determined total system efficiency of the measurements. As can be seen, the simulation lays approximately 10% above the measurements and it possesses a slightly lower slope. In the simulated results the polarization efficiency remained nearly constant at $\eta_{LP} \approx 93\%$ and the decreasing slope was mainly determined by the combining efficiency. A difference in the B -integral of the pulses to be combined can justify the power-dependent decrease of the combining efficiency. Referring to [60], the impact on the combining efficiency of two pulses with a small B -integral difference is relatively small. This holds for low pump powers, but for higher pump powers this B -integral difference increases. Additionally, there are two combining stages. At the first (PBS₂) the first and second co-propagating pulses are combined with the first and second counter-propagating ones, respectively. According to Fig. 4.19a, the difference of the B -integrals of the corresponding pulses is smaller than the B -integral difference between the resulting combined pulses. Consequently, the combining loss at the second combining stage (PBS₁) is larger than that at the first combining stage.

In the case of single-side pumping the accumulated phase due to SPM is different for the co- and counter-propagating beams which leads, as already mentioned, to an asymmetric distribution of the inversion and, hence, to a distinct amplification behavior. Fig. 4.20 shows a schematic depiction of the growth of the signal power along the fiber for both cases. As can be seen, the B -integral for the co-propagating case (indicated by the area below the corresponding curve in Fig. 4.20) can be significantly larger than that of the counter-propagating case. Just as an illustration of the impact of this effect, the nonlinear phase of the co-propagating pulses was increased by a factor of 2 (in the example of Fig. 4.20, the depicted areas differ by a factor of 4). This is additionally shown in Fig. 4.19a and Fig. 4.19b (with dashed lines). As a consequence, this increase of the B -integral differences of the corresponding pulses leads to a stronger reduction of the combining efficiency at both combining stages. The polarization efficiency decreased just slightly by 3% up to the maximum pump power. All together, a more drastic decrease of the total system efficiency was obtained, which comes close to the measurement. But this was just a rough

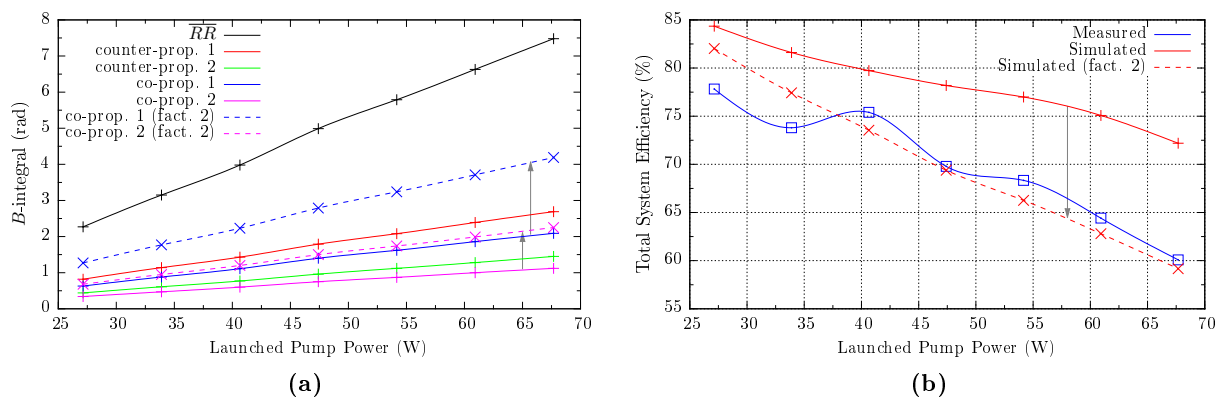


Fig. 4.19: (a) Simulated B -integrals with fitted gain factors for both a single pulse (\overline{RR}) and a division into four pulses, and (b) the simulated and the measured total system efficiency.

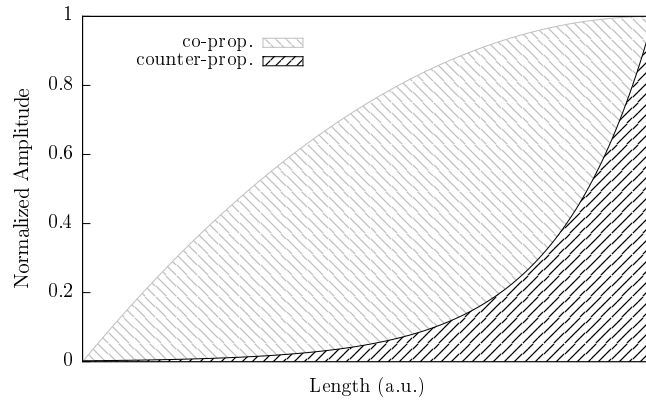


Fig. 4.20: Difference in the growth of an amplified signal for co- and counter-propagating pumping.

estimation, which should illustrate the impact on the efficiency of different accumulated phases due to SPM. However, it is not clear if the degradation of the measured total system efficiency was partly caused by a reduction of the polarization efficiency, since this was not measured. For a more accurate simulation, the different developments of the co- and counter-propagating pulses together with saturation must be considered, which will influence the resulting nonlinear phases. Moreover, the impact of XPM plays also a role because the counter-propagating pulses overlap within the fiber. For this an even more complex calculation would be necessary, since additionally the change of the overlap of the pulses must be considered to calculate the resulting phase. Again as a rough estimation, the pulses were assumed to overlap completely within the whole interaction length and the additional phase terms were calculated according to Eq. (2.38) and Eq. (2.39). As a result, the B -integrals of all four pulses increased, whereby the pulses with the higher peak powers (which means those with the larger B -integral, according to Fig. 4.19a) imprint a larger nonlinear phase on the other ones. Consequently, the total nonlinear phases between all pulses are equalized to a certain extent and the reduced B -integral differences lead to an increase of both the polarization efficiency and the combining efficiency. Therefore, XPM may partially compensate for the effect of the B -integral difference. But again, this was just a rough estimation and it needs to be simulated more accurately.

From the discussion above it can be inferred that, in order to compensate for the difference in the accumulated nonlinear phases of the co- and counter-propagating beams, a symmetric pump geometry, i.e. double-sided pumping, should be used. This would lead to a symmetric distribution of the inversion and, therefore, to the same amplification characteristics for all the pulses independently of their direction of propagation. But the opposite-facing pump diodes could destroy each other if the fiber reaches transparency, since then a significant amount of pump power will be transmitted through the fiber and no pump blockers can be used. To avoid this, two consecutive fiber amplifiers within the Sagnac loop could be used, which are pumped from opposite sides. In this case one pump blocker can be used between them. The counter-propagating pulses will be amplified equally and, therefore, the B -integral differences between the corresponding first and second pulses will be the same. However, the difference between the B -integrals of the first and second pulses will still degrade the combination at the last combining

stage. To compensate for this (saturation effect), the B -integrals of the pulses must be equalized by means of the ratios of the input pulses to be amplified. A possibility is to use the rotation angle of the HWP_0 at the input, which controls the ratios of the first and the delayed pulses in both Sagnac channels. The peak powers of the first pulses can be reduced to obtain pulses of the same peak powers after amplification. But this works only for setups containing two PBSs. Nevertheless, to reduce the difference of the B -integrals, the input and the output pulses must be controlled separately. Therefore, a separation of the division and combination stages of the DPA setup seems to be advantageous. For this, an active stabilization system is needed. Thus, only active stabilization in combination with a tailoring of the pulse train allows for efficient combining with high energy extraction (and high B -integrals).

5 Conclusion

High-power laser systems based on ytterbium-doped fiber amplifiers delivering ultrashort pulses find application in many fields such as material processing or HHG. For these applications both the achievable average power as well as the pulse energy are of concern. For the high-performance scaling of such laser systems, limitations are set by nonlinear and thermal effects, which may cause detrimental distortions of the pulse. There are different techniques to overcome these limitations. Among them the polarization beam combination of ultrashort pulses, that are amplified in a certain number of spatially separated amplifiers, is one of the most promising. This technique allows achieving output powers beyond the values given for single amplifiers due to a reduction of peak power during the amplification process. The disadvantage is that this technique requires an active-feedback system for phase stabilization. In order to transfer the advantages of this setup to a passive approach, a Sagnac interferometer can be used. In this case, a fiber amplifier is placed inside of the Sagnac loop, with which two counter-propagating pulses are amplified. However, in this implementation the reduction of the peak power of the pulses is limited by a factor of two. To reduce the peak power even further, this approach can be extended with the idea of DPA. This idea exploits a temporal splitting of the pulses. With this, the peak power can be reduced by the number of the generated pulse replicas. Such a technique has just been demonstrated for ultrashort pulses up to now. The goal of this work was the realization and investigation of such a passive DPA setup as the main amplification stage of an existing CPA system, which delivered strongly stretched and pre-amplified pulses in the nanosecond range.

In order to achieve temporal delays in the order of a few nanoseconds, a sequence of two Mach-Zehnder type interferometers was placed in front of the Sagnac interferometer, whereby one channel of each Mach-Zehnder interferometer included a long delay line. In a proof-of-principle experiment the division of non-stretched femtosecond pulses in eight replicas with delays in the nanosecond range could be achieved. These pulses were sent through a small passive single-mode fiber within the Sagnac loop to demonstrate the feasibility and the advantage of this procedure when compared to a non-divided pulse approach. It could be shown that in the case of eight pulses no spectral broadening due to SPM was observable whereas for one pulse it was significant. With this setup, a combining efficiency of 83% and a polarization efficiency of 77% could be achieved. The reason for the reduced polarization efficiency was traced back to the poor-quality of mirrors employed.

Furthermore, a theoretical description of the setup was developed based on the Jones calculus. It could be shown that the quality of the beam splitters, in terms of the parameters R_s and T_p , determines a baseline loss of the setup, which cannot be optimized by means of the settings of the integrated HWPs. Depending on the number of PBSs, that loss can be significant. This loss amounts for typical parameters of $R_s = 99\%$ and $T_p = 95\%$ approximately to 11% for two and approximately to 25% for three PBSs. Moreover, it has been shown that the polarization

leakage of those non-perfect PBSs produce pre- and post-pulses, which generate modulations in the spectrum. A solution to clean the output pulse from the parasitic pulses may be to use an AOM.

Next, an improved setup was implemented within the CPA system. For this, mirrors of better quality and an increased beam size were used, in order to provide a nearly constant collimation of the beams over the long optical paths present in the setup. Temporal delays of 7 ns and 14 ns for the division of 2 ns pulses into eight replicas have been realized. Those were amplified in a rod-type PCF within the Sagnac loop. With this system, two investigations were made: operation at high average power and at high pulse energy, respectively. In a first experiment at relatively low average power, an uncompressed output power of 20 W at a repetition rate of 4 MHz with a total system efficiency of 84.6 % could be achieved. Unfortunately, at this point it was found out that some of the available PBSs caused distortions in the beams. For this reason the complexity of the setup was reduced to two PBSs, which corresponds to a division into four pulses. With this, a maximum compressed average output power of 49 W and a pulse duration of 526 fs were achieved, which corresponded to a total system efficiency of approximately 72 %. Up to a power of approximately 38 W the efficiency remained higher than 87 %, whereas it dropped to 60 % for higher output powers. This strong degradation was mainly due to thermal effects. These caused fluctuations in the beams, which in turn had a significant impact on the stability of the combining process because of the rupture of the symmetry required by the passive Sagnac geometry. In the high pulse energy case, a compressed pulse energy of 0.52 mJ at a repetition rate of 20 kHz and a pulse duration of 601 fs were achieved. These parameters corresponded to a peak power of approximately 870 MW. The total system efficiency decreased nearly linearly from 78 % to 60 % for increasing power up to the given values. Based on simulations it could be shown that the main reason for this steady degradation was the difference of the accumulated nonlinear phases of the divided pulses. Finally, compared to a non-divided single pulse, a two to four times smaller B -integral was obtained, which resulted in less modulations in the spectrum, and, therefore, in a shorter and cleaner pulse. However, due to an overall more efficient extraction for the case of one pulse, no improvement in the extracted pulse energy could be achieved. In principle, the results demonstrate the potential of the concept of temporal and spatial division of ultrashort pulses during their amplification. Since most of the drawbacks of the experimental setup resulted from the Sagnac geometry and not from the DPA approach, the next step will be to introduce a DPA stage into a CPA system employing CBC with an active-feedback. Furthermore, the realization of the DPA stage needed plenty of 45° mirrors, which causes polarization-dependent phases and losses. Therefore, a linear configuration will be applied in the future, which uses 0° mirrors due to their negligible phase impact. Moreover, the division and combination stages of the DPA setup will be separated, to control the B -integral differences of the individual pulses. For this, an active stabilization system will be employed. Such a system will be able to produce pulse energies beyond the 3 mJ mark, which represents the maximum achieved value for ultrashort fiber lasers so far.

Bibliography

- [1] A. Ancona, F. Röser, K. Rademaker, J. Limpert, S. Nolte, and A. Tünnermann. High speed laser drilling of metals using a high repetition rate, high average power ultrafast fiber CPA system. *Opt. Express*, 16(12):8958–68, June 2008.
- [2] A. McPherson, G. Gibson, H. Jara, U. Johann, T. S. Luk, I. A. McIntyre, K. Boyer, and C. K. Rhodes. Studies of multiphoton production of vacuum-ultraviolet. *J. Opt. Soc. Am. B*, 4(4):595–601, 1987.
- [3] S. Hädrich, J. Rothhardt, M. Krebs, F. Tavella, A. Willner, J. Limpert, and A. Tünnermann. High harmonic generation by novel fiber amplifier based sources. *Opt. Express*, 18(19):20242–20250, September 2010.
- [4] Anthony E Siegman. *Lasers*. University Science Books, Mill Valley, California, 1st edition, 1986.
- [5] Donna Strickland and Gerard Mourou. Compression of amplified chirped optical pulses. *Opt. Commun.*, 56(3):219–221, 1985.
- [6] Tino Eidam, Stefan Hanf, Enrico Seise, Thomas V. Andersen, Thomas Gabler, Christian Wirth, Thomas Schreiber, Jens Limpert, and Andreas Tünnermann. Femtosecond fiber CPA system emitting 830 W average output power. *Opt. Lett.*, 35(2):94–96, January 2010.
- [7] Tino Eidam, Jan Rothhardt, Fabian Stutzki, Florian Jansen, Steffen Hädrich, Henning Carstens, Cesar Jauregui, Jens Limpert, and Andreas Tünnermann. Fiber chirped-pulse amplification system emitting 3.8 GW peak power. *Opt. Express*, 19(1):255–260, January 2011.
- [8] Tso Yee Fan. Laser Beam Combining for High-Power , High-Radiance Sources. *IEEE J. Selected Topics in Quantum Electron.*, 11(3):567–577, 2005.
- [9] Arno Klenke, Enrico Seise, Stefan Demmler, Jan Rothhardt, Sven Breilkopf, Jens Limpert, and Andreas Tünnermann. Coherently-combined two channel femtosecond fiber CPA system producing 3 mJ pulse energy. *Opt. Express*, 19(24):24280–5, November 2011.
- [10] Louis Daniault, Marc Hanna, Dimitris N. Papadopoulos, Yoann Zaouter, Eric Mottay, Frédéric Druon, and Patrick Georges. Passive coherent beam combining of two femtosecond fiber chirped-pulse amplifiers. *Opt. Lett.*, 36(20):4023–4025, 2011.
- [11] Shian Zhou, Frank W. Wise, and Dimitre G. Ouzounov. Divided-pulse amplification of ultrashort pulses. *Opt. Lett.*, 32(7):871–873, April 2007.
- [12] L. J. Kong, L. M. Zhao, S. Lefrancois, D. G. Ouzounov, C. X. Yang, and F. W. Wise. Generation of megawatt peak power picosecond pulses from a divided-pulse fiber amplifier. *Opt. Lett.*, 37(2):253–255, January 2012.

-
- [13] L. Daniault, M. Hanna, D. N. Papadopoulos, Y. Zaouter, E. Mottay, F. Druon, and P. Georges. High peak-power stretcher-free femtosecond fiber amplifier using passive spatio-temporal coherent combining. *Opt. Express*, 20(19):21627–21634, 2012.
- [14] Max Bom and Emil Wolf. *Principles of Optics*. Cambridge University Press, 7th edition, 1999.
- [15] Andrew M. Weiner. *Ultrafast Optics*. John Wiley & Sons, Inc., Hoboken, New Jersey, 2009.
- [16] Govind P. Agrawal. *Nonlinear Fiber Optics*. Academic Press, 3rd edition, 2001.
- [17] Dieter Meschede. *Optik, Licht und Laser*. Vieweg+Teubner Verlag, Wiesbaden, 3. edition, 2008.
- [18] Bahaa E. A. Saleh and Malvin Carl Teich. *Fundamentals of Photonics*. John Wiley & Sons. Inc., Hoboken, New Jersey, 2nd edition, 2007.
- [19] Edward Collett. *Field Guide to Polarization*. SPIE Press, Washington, 2005.
- [20] Rüdiger Paschotta. Coherence Length of Ultrashort Pulses, 2006.
- [21] Ajoy Ghatak and K. Thyagarajan. *An Introduction to Fiber Optics*. Cambridge University Press, 1998.
- [22] Robert W. Boyd. *Nonlinear Optics*. Academic Press, 3rd edition, 2008.
- [23] M. D. Perry, T. Ditmire, and B. C. Stuart. Self-phase modulation in chirped-pulse amplification. *Opt. Lett.*, 19(24):2149–51, December 1994.
- [24] Gadi Fibich and Alexander L. Gaeta. Critical power for self-focusing in bulk media and in hollow waveguides. *Opt. Lett.*, 25(5):335–7, March 2000.
- [25] B. Chann, A. K. Goyal, T. Y. Fan, A. Sanchez-Rubio, B. L. Volodin, and V. S. Ban. Efficient, high-brightness wavelength-beam-combined commercial off-the-shelf diode stacks achieved by use of a wavelength-chirped volume Bragg grating. *Opt. Lett.*, 31(9):1253–1255, 2006.
- [26] Oliver Schmidt, C. Wirth, D. Nodop, Jens Limpert, Thomas Schreiber, T. Peschel, R. Eberhardt, and Andreas Tünnermann. Spectral beam combination of fiber amplified ns-pulses by means of interference filters. *Opt. Express*, 17(25):22974–22982, 2009.
- [27] Thomas H. Loftus, Alison M. Thomas, Paul R. Hoffman, Marc Norsen, Rob Royse, Anping Liu, and Eric C. Honea. Spectrally Beam-Combined Fiber Lasers for High-Average-Power Applications. *IEEE J. Selected Topics in Quantum Electron.*, 13(3):487–497, 2007.
- [28] Eric C. Cheung, James G. Ho, Timothy S. McComb, and Stephen Palese. High density spectral beam combination with spatial chirp precompensation. *Opt. Express*, 19(21):20984–20990, 2011.

- [29] Z. M. Huang, C. L. Liu, J. F. Li, D. Y. Zhang, H. F. Wang, Y. Q. Luo, and Q. Q. Hu. Numerical Analysis of Coherent Combination for Fiber Lasers and Application to Beam Steering. *Laser Phys.*, 22(8):1347–1352, 2012.
- [30] C. X. Yu, S. J. Augst, S. M. Redmond, K. C. Goldizen, D. V. Murphy, A. Sanchez, and T. Y. Fan. Coherent combining of a 4 kW, eight-element fiber amplifier array. *Opt. Lett.*, 36(14):2686–8, July 2011.
- [31] Tso Yee Fan. The Effect of Amplitude (Power) Variations on Beam Combining Efficiency for Phased Arrays. *IEEE J. Selected Topics in Quantum Electron.*, 15(2):291–293, 2009.
- [32] Leo A. Siiman, Wei-zung Chang, Tong Zhou, and Almantas Galvanauskas. Coherent femtosecond pulse combining of multiple parallel chirped pulse fiber amplifiers. *Opt. Express*, 20(16):18097–18116, 2012.
- [33] L. Michaille, C. R. Bennett, D. M. Taylor, T. J. Shepherd, J. Broeng, H. R. Simonsen, and A. Petersson. Phase locking and supermode selection in multicore photonic crystal fiber lasers with a large doped area. *Opt. Lett.*, 30(13):1668–1670, 2005.
- [34] D. R. Scifres, R. D. Burnham, and W. Streifer. Phase-locked semiconductor laser array. *Appl. Phys. Lett.*, 33(12):1015–1017, 1978.
- [35] Tsai-wei Wu, Wei-zung Chang, Almantas Galvanauskas, and Herbert G Winful. Model for passive coherent beam combining in fiber laser arrays. *Opt. Express*, 17(22):19509–18, October 2009.
- [36] D. A. Rockwell and C. R. Giuliano. Coherent coupling of laser gain media using phase conjugation. *Opt. Lett.*, 11(3):147–149, March 1986.
- [37] Timothy. H. Russell, Shawn M. Willis, Matthew B. Crookston, and Won B. Roh. Stimulated Raman scattering in multi-mode fibers and its application to beam cleanup and combining. *J. Nonlin. Opt. Phys., Mater.*, 11:303–316, 2002.
- [38] Ioachim Pupeza, Tino Eidam, Jens Rauschenberger, Birgitta Bernhardt, Akira Ozawa, Ernst Fill, Alexander Apolonski, Thomas Udem, Jens Limpert, Zeyad A. Alahmed, Abdallah M. Azzeer, Andreas Tünnermann, Theodor W. Hänsch, and Ferenc Krausz. Power scaling of a high-repetition-rate enhancement cavity. *Opt. Lett.*, 35(12):2052–2054, June 2010.
- [39] T. W. Hänsch and B. Couillaud. Laser frequency stabilization by polarization spectroscopy of a reflecting reference cavity. *Opt. Commun.*, 35(3):441–444, 1980.
- [40] R. W. P. Drever, J. L. Hall, F. V. Kowalski, J. Hough, G. M. Ford, a. J. Munley, and H. Ward. Laser phase and frequency stabilization using an optical resonator. *Appl. Phys. B*, 31(2):97–105, June 1983.
- [41] Rui Xiao, J. Hou, M. Liu, and Z. F. Jiang. Coherent combining technology of master oscillator power amplifier fiber arrays. *Opt. Express*, 16(3):2015–22, February 2008.

- [42] Rongtao Su, Pu Zhou, Xiaolin Wang, Hanwei Zhang, and Xiaojun Xu. Active coherent beam combining of a five-element, 800 W nanosecond fiber amplifier array. *Opt. Lett.*, 37(19):3978–3980, October 2012.
- [43] X. Wang, J. Leng, P. Zhou, Y. Ma, X. Xu, and Z. Liu. 1.8-kW simultaneous spectral and coherent combining of three-tone nine-channel all-fiber amplifier array. *Appl. Phys. B*, 107(3):785–790, May 2012.
- [44] Radoslaw Uberna, Andrew Bratcher, and Bruce G. Tiemann. Coherent polarization beam combination. *IEEE J. Quantum Electron.*, 46(8):1191–1196, 2010.
- [45] Enrico Seise, Arno Klenke, Jens Limpert, and Andreas Tünnermann. Coherent addition of fiber-amplified ultrashort laser pulses. *Opt. Express*, 18(26):27827–27835, 2010.
- [46] HighQLaser. femtoTrain K-1030-200fs Yb. Data sheet.
- [47] Edmund Optics GmbH. Breitbandige polarisierende Strahlteilerwürfel. <http://www.edmundoptics.de/optics/beamsplitters/cube-beamsplitters>. 12.12.2012.
- [48] Thorlabs Inc. Broadband Dielectric Mirrors. <https://www.thorlabs.de/>. 14.12.2012.
- [49] Vadim V. Lozovoy, Igor Pastirk, and Marcos Dantus. Multiphoton intrapulse interference. IV. Ultrashort laser pulse spectral phase characterization and compensation. *Opt. Lett.*, 29(7):775–777, April 2004.
- [50] Philip Russell. Photonic crystal fibers. *Science (New York, N.Y.)*, 299(5605):358–362, January 2003.
- [51] Fabian Stutzki, Florian Jansen, Tino Eidam, Alexander Steinmetz, Cesar Jauregui, Jens Limpert, and Andreas Tünnermann. High average power large-pitch fiber amplifier with robust single-mode operation. *Opt. Lett.*, 36(5):689–691, March 2011.
- [52] ALTECHNA. HR Laser Line mirrors (HR). <http://www.altechna.com/>. 23.12.2012.
- [53] LIMO Lissotschenko Mikrooptik GmbH. Fiber-Coupled Diode Laser Pump Modules. <http://www.limo.de/>. 23.12.2012.
- [54] Cesar Jauregui, Tino Eidam, Hans-Jürgen Otto, Fabian Stutzki, Florian Jansen, Jens Limpert, and Andreas Tünnermann. Temperature-induced index gratings and their impact on mode instabilities in high-power fiber laser systems. *Opt. Express*, 20(1):440–451, January 2012.
- [55] Florian Jansen, Fabian Stutzki, Hans-Jürgen Otto, Tino Eidam, Andreas Liem, Cesar Jauregui, Jens Limpert, and Andreas Tünnermann. Thermally induced waveguide changes in active fibers. *Opt. Express*, 20(4):3997–4008, 2012.
- [56] Gregory D. Goodno, Chun-Ching Shih, and Joshua E. Rothenberg. Perturbative analysis of coherent combining efficiency with mismatched lasers. *Opt. Express*, 18(24):25403–25414, November 2010.

-
- [57] Gregory D. Goodno, Chun-Ching Shih, and Joshua E. Rothenberg. Perturbative analysis of coherent combining efficiency with mismatched lasers: errata. *Opt. Express*, 20(21):23587–235878, October 2012.
- [58] Lee M. Frantz and John S. Nodvik. Theory of Pulse Propagation in a Laser Amplifier. *J. Appl. Phys.*, 34(8):2346, 1963.
- [59] Damian Schimpf, Enrico Seise, Jens Limpert, and Andreas Tünnermann. Decrease of pulse-contrast in nonlinear chirped-pulse amplification systems due to high-frequency spectral phase ripples. *Opt. Express*, 16(12):8876–8886, 2008.
- [60] Arno Klenke, Enrico Seise, Jens Limpert, and Andreas Tünnermann. Basic considerations on coherent combining of ultrashort laser pulses. *Opt. Express*, 19(25):25379–87, December 2011.
- [61] Rüdiger Paschotta. *Field Guide to Laser Pulse Generation*. SPIE Press, Bellingham, WA, 2008.

Appendix

A Fourier Transformation

The Fourier transformation and the inverse Fourier transformation are defined for temporal and spatial domain as

$$\tilde{E}(\omega) = \mathcal{F}\{E(t)\} = \frac{1}{2\pi} \int_{-\infty}^{\infty} E(t) \exp(i\omega t) dt \quad (\text{A.1})$$

$$E(t) = \mathcal{F}^{-1}\{\tilde{E}(\omega)\} = \int_{-\infty}^{\infty} \tilde{E}(\omega) \exp(-i\omega t) d\omega \quad (\text{A.2})$$

$$\tilde{\mathbf{E}}(\mathbf{k}) = \mathcal{F}\{\mathbf{E}(\mathbf{r})\} = \frac{1}{(2\pi)^3} \int_{-\infty}^{\infty} \mathbf{E}(\mathbf{r}) \exp(-i\mathbf{k}\mathbf{r}) d\mathbf{r} \quad (\text{A.3})$$

$$\mathbf{E}(\mathbf{r}) = \mathcal{F}^{-1}\{\tilde{\mathbf{E}}(\mathbf{k})\} = \int_{-\infty}^{\infty} \tilde{\mathbf{E}}(\mathbf{k}) \exp(i\mathbf{k}\mathbf{r}) d\mathbf{k} \quad (\text{A.4})$$

B Matrix Rotation

If an optical polarizing device is rotated by an angle θ , its Jones matrix \mathbf{J} can be transformed to $\mathbf{J}(\theta)$. With the help of the rotation matrix [19]

$$\mathbf{R}(\theta) = \begin{pmatrix} \cos \theta & \sin \theta \\ -\sin \theta & \cos \theta \end{pmatrix} \quad (\text{B.5})$$

the transformed Jones matrix is obtained by using

$$\mathbf{J}(\theta) = \mathbf{R}(-\theta)\mathbf{J}\mathbf{R}(\theta) \quad . \quad (\text{B.6})$$

C Power Conservation for a Beam Splitter

A beam splitter, also a PBS, divides an input field $\mathbf{E}(\mathbf{r}, t)$ in two parts: $\mathbf{E}_1(\mathbf{r}, t)$ and $\mathbf{E}_2(\mathbf{r}, t)$. Due to the conservation of the power then it should be

$$|\mathbf{E}(\mathbf{r}, t)|^2 = |\mathbf{E}_1(\mathbf{r}, t)|^2 + |\mathbf{E}_2(\mathbf{r}, t)|^2 \quad . \quad (\text{C.7})$$

But if one calculates the sum of both fields, according to interference, the absolute square is given by (omitting the brackets)

$$|\mathbf{E}|^2 = (\mathbf{E}_1 + \mathbf{E}_2)(\mathbf{E}_1 + \mathbf{E}_2)^* = |\mathbf{E}_1|^2 + |\mathbf{E}_2|^2 + \underbrace{\mathbf{E}_1\mathbf{E}_2^* + \mathbf{E}_1^*\mathbf{E}_2}_{\stackrel{!}{=}0} \quad . \quad (\text{C.8})$$

Consequently, the additional term must be zero. Reformulating them into

$$\mathbf{E}_1\mathbf{E}_2^* + \mathbf{E}_1^*\mathbf{E}_2 = 2\Re\{\mathbf{E}_1^*\mathbf{E}_2 \exp[i(\phi_2 - \phi_1)]\} = 2\mathbf{E}_1^*\mathbf{E}_2 \cos(\phi_2 - \phi_1) \quad (\text{C.9})$$

shows, that a phase difference of $\phi_2 - \phi_1 = \pm\pi/2$ is needed.

D Deconvolution Factors

For a known pulse shape in time domain it is possible to calculate the pulse duration from the autocorrelation duration. After [61], the so called deconvolution factors for some examples of pulse shapes are summarized in Tab. D.1.

Tab. D.1: Deconvolution factors.

Pulse Shape	Deconvolution Factor
Squared Hyperbolic Secant (sech^2)	0.647
Gaussian	0.707
Rectangular	1
Triangular	0.692

Acknowledgment

On this page I would like to thank all those who knowingly or unknowingly made a contribution to any extent to this work.

First of all, I want to thank especially the director of the Institute, Andreas Tünnermann, and the head of the department “Fiber & Waveguide Lasers”, Jens Limpert, for giving me the opportunity to do my Master’s Thesis at the Institute of Applied Physics and to work on this topic.

Furthermore, special thanks go to Cesar Jauregui Misas who always had an ear open for any problems, who has outdone itself with its helpfulness and friendliness, and who has contributed through extensive discussions to the continuous progress of my work. Moreover, I want to thank Arno Klenke for the supervision of my work and for doing the groundwork in the field of coherent combining. Especially, I thank him for the support in the laboratory during the experiments and for the help by the evaluation of the results. I thank him further for the many helpful discussions and hints.

I would also like to thank Tino Eidam, who with his funny and critical way could not only provide for amusement, but also has significantly contributed to the progress of this “Bachelor’s Thesis”. Moreover, I want to thank Sven Breilkopf, as ally in the field of combining, for his theoretical and experimental support. At this point I would like to thank again Jens Limpert, who followed with interest my work and gave good advice.

Many thanks to all other members of the group “Fiber & Waveguide Lasers” for the constant helpfulness and pleasant working atmosphere. Namely, thanks to: Steffen Hädrich, Jan Rothhardt, Thomas Gottschall, Florian Jansen, Christoph Jocher, Manuel Krebs, Reinhold Lehneis, Hans-Jürgen Otto, Stefan Demmler, Martin Baumgartl, Fabian Stutzki and Alexander Steinmetz. All you could ask for help and it was always supported.

I am also grateful to my student colleagues and friends, Roberto Knoth and Daniel Asoubar, for their helpful discussions outside the institute and during our entire studies. Thank you very much for the great time.

Finally, I would like to thank my parents and my grandparents for the financial support and their care. I also thank my brother Enrico and his wife Corinna for the constant interest in my studies. Especially, I want to thank my brother for any support in the field of informatics. My last but not least thanks go to my live-in girlfriend Nadine Haupt and my son Linus Maximus Kienel for their love and support in good times and bad times. I am eternally grateful to you for your understanding that I had to use a lot of strength to overcome this challenging program of study. You gave me the strength for that. Without you I would not have done it. Thank you!

Statement of Authorship

I hereby certify that this report has been made by myself independently and without use of other than the stated sources and aids. All contained references to external sources have been identified as such. In particular, I acknowledge that both verbatim statements as well as in their own words given statements of other authors of the source have been invariably quoted.

Date: January 28, 2013

Signature: